

Copyright

by

Jacob Alexander Hummel

2016

The Dissertation Committee for Jacob Alexander Hummel certifies that
this is the approved version of the following dissertation:

**The First Supernovae: Impact on Early Star Formation and
Prospects for Direct Detection**

Committee:

Volker Bromm, Supervisor

J. Craig Wheeler

Miloš Milosavljević

Steven Finkelstein

Naoki Yoshida

**The First Supernovae: Impact on Early Star Formation and Prospects
for Direct Detection**

by

Jacob Alexander Hummel, B.S.; M.A.

Dissertation

Presented to the Faculty of the Graduate School of
The University of Texas at Austin
in Partial Fulfillment
of the Requirements
for the degree of
Doctor of Philosophy

The University of Texas at Austin
May, 2016

The First Supernovae: Impact on Early Star Formation and Prospects for Direct Detection

Jacob Alexander Hummel, Ph.D.

The University of Texas at Austin, 2016

Supervisor: Volker Bromm

The formation of the first stars in the Universe marked a pivotal moment in cosmic history, initiating the transition from the simple initial conditions of the big bang to the complex structures we see today. Ionizing radiation produced by these so-called Population III stars began the process of reionization, and the supernovae marking their deaths initiated the process of chemical enrichment. These violent explosions and the compact remnants they leave behind also produce significant amounts of high-energy X-rays and cosmic rays able to travel through the predominantly neutral intergalactic medium and build up a cosmic background. To better understand how these first supernovae impact subsequent episodes of metal-free star formation, we employ *ab-initio*, cosmological hydrodynamics simulations to model the formation of stars in a $\sim 10^6 M_\odot$ minihalo at $z \gtrsim 20$ under the influence of both an X-ray and cosmic ray background. The presence of an ionizing background—whether X-rays or cosmic rays—serves to expedite the collapse of gas to high densities by enhancing molecular hydrogen cooling, thus allowing stars to form at substantially earlier epochs in strongly irradiated minihalos. The mass of the stars thus formed however appears

to be quite robust, maintaining a characteristic mass of order \sim a few $\times 10 M_{\odot}$ even as the strength of the ionizing background varies by several orders of magnitude. We furthermore assess the prospects for direct detection of the first supernovae should they happen to end their lives as extremely energetic pair-instability supernovae, which should be within the detection limits of the upcoming *James Webb Space Telescope*. Using a combination of semi-analytic models and cosmological simulations to estimate their source density, we find that the primary obstacle to observing such events is their scarcity, not their faintness. Finally, we describe the novel software developed to enable this research. These tools for manipulating and analyzing simulation data have been released as the open-source GADGET DataFrame Library: `gadfly`.

Contents

List of Figures	viii
Chapter One: Introduction	1
1.1 From the Big Bang to Now	1
1.2 Cosmic Renaissance	3
1.3 The First Supernovae	5
Chapter Two: The Source Density and Observability of Pair-Instability Supernovae from the First Stars	8
2.1 Introduction	8
2.2 The PISN Rate	13
2.3 JWST Observability	25
2.4 Discussion and Conclusions	34
Chapter Three: Population III Star Formation Under X-ray Feedback	38
3.1 Introduction	38
3.2 Cosmological Context	41
3.3 Numerical Methodology	47
3.4 Results	57
3.5 Summary and Conclusions	68
Chapter Four: Population III Star Formation Under Cosmic Ray Feedback . .	71
4.1 Introduction	71
4.2 Cosmic Rays in the Early Universe	75
4.3 Numerical Methodology	79
4.4 Results	89

4.5 Summary and Conclusions	99
Chapter Five: A pandas-based Framework for Analyzing GADGET Simulation Data	102
5.1 Introduction	102
5.2 A Framework built on pandas	105
5.3 Visualization	114
5.4 Future Development	116
5.5 Summary	117
Chapter Six: Outlook	118
Appendix A: Appendix	119
Bibliography	123

List of Figures

2.1	a) the factor f_{LW} by which LW feedback increases the critical mass for star formation; points show the results of the simulation, the red line our fit. b) The critical mass for star formation in both simulations. Blue crosses mark the critical mass for star formation in the absence of LW feedback, red crosses in its presence. The blue line shows the best fit critical mass from Eq. (2.1), given by a temperature of 2200 K; the red line the critical mass from Eq. (2.9) for LW feedback using the fit for f_{LW} given in Eq. (2.8). The green line marks the halo mass corresponding to a virial temperature of 10^4 K, and the black dashed line represents the critical mass employed, accounting for atomic cooling in halos with virial temperatures above 10^4 K.	18
2.2	a) \dot{n}_{PISN} in the upper limit of no feedback (blue), with chemical feedback (green), LW feedback (red) and the resulting PISN rate for the conservative (chemical plus LW) feedback case (black). b) Same as (a), but for enhanced massive star formation.	21
2.3	The observable PISN rates in number per year per JWST field of view above a given redshift in the upper limit of no feedback (blue line), in the conservative feedback case (solid red line), and the enhanced star formation case (dashed red line). The rates calculated by Miralda-Escudé & Rees (1997), Mackey et al. (2003), Weinmann & Lilly (2005) and Wise & Abel (2005) are also shown for reference. Red points account for feedback; blue points do not.	24
2.4	The temperature and radius of our blackbody fits as a function of source frame time since the explosion for models R250, B200, R175 and He100. The secondary rise in temperature seen in R250 and B200 is caused by the decay of ^{56}Ni reheating the ejecta at late times. Note also that the apparent radii begin to decrease again at late times; this can be interpreted as the photosphere receding into the ejecta as the material cools.	27

- 3.1 X-ray average intensity as a function of redshift. The lightest grey line represents our fiducial model J_0 , with successively darker grey lines denoting 10, 100, and 1000 J_0 , respectively. The blue and red ranges denote the critical intensity above which collapse of the baryonic component into a $2 \times 10^5 M_\odot$ and $10^6 M_\odot$ halo is suppressed, respectively. In each case, the upper limit of the range assumes the contribution from secondary ionisation is negligible, while the lower limit denotes $J_{\text{XR,crit}}$ for maximally effective secondary ionisation. The vertical grey bar denotes the range of redshifts over which our minihaloes first reach $n = 10^{12} \text{ cm}^{-3}$ 44
- 3.2 Cumulative column density along both polar and equatorial lines of sight approaching the centre of the minihalo. Shown is the column density for a selection of snapshots from just prior to the formation of the first sink particle to 5000 yr later, with different colors indicating different snapshots. Note that the scatter in the central 10^3 AU is larger in the equatorial plane than along the pole: as the accretion disc rotates, occasionally a sink particle orbiting the density-averaged centre lands within the chosen line of sight. 45
- 3.3 Column density as a function of gas number density along both polar (green) and equatorial (blue) lines of sight. Points sample the distribution of column density as a function of number density for their respective lines of sight across several snapshots, while the lines indicate the χ^2 best fit. 50
- 3.4 X-ray ionisation and heating rates for H I, He I and He II as a function of total number density for the $J_{\text{XR}} = J_0$ case at $z = 25$. In both panels, the solid blue, dashed green, and dash-dotted red lines denote H I, He I, and He II, respectively. The grey lines in each style demonstrate the expected rates in the absence of X-ray self-shielding for that species. H I dominates both ionisation and heating when the relative abundances of these species are accounted for, and we see that X-rays penetrating the minihalo experience significant attenuation above densities of $n \sim 10^6 \text{ cm}^{-3}$ 52

3.5 Density projection of the final simulation output 5000 yr after the formation of the first sink particle on progressively smaller scales for both the $J_{\text{XR}} = 0$ (top) and the shielded $J_{\text{XR}} = 10^2 J_0$ (bottom) simulations. White boxes indicate the region depicted on the next smaller scale. Clockwise from top left: full simulation box; minihalo and surrounding filamentary structure; central 100 pc of minihalo; central 10 pc. The density scale for each panel is included just to the right – note that the scaling changes from panel to panel. In both cases, note how the morphology approaches an increasingly smooth, spherical distribution on the smallest scales, where the gas is in quasi-hydrostatic equilibrium. In the shielded $J_{\text{XR}} = 10^2 J_0$ case, the low-density filamentary structure is smoothed out due to X-ray heating, whereas gas at high densities is shielded and proceeds to collapse unimpeded.	55
3.6 Mass-weighted temperature distribution of the collapsing gas in each simulation, shown just prior to sink formation—or maximum density reached in the case of the $10^3 J_0$ background. Each panel shows the behaviour of the gas in the presence of the CXB, both shielded (in blue) and unshielded (in red). For comparison, the gas behaviour in the $J_{\text{XR}} = 0$ case is shown in grey. Dashed lines denote the CMB temperature. All simulations except the $10^3 J_0$ case successfully collapse to high densities. Gas at low densities gets progressively hotter and gas in the loitering phase gets progressively cooler with increasing J_{XR} . Note that in all cases where the minihalo successfully proceeds to collapse, the shielded gas re-converges to the $J_{\text{XR}} = 0$ case prior to reaching sink formation densities.	56
3.7 Total gas mass within 1 pc of the highest density point in each simulation over cosmic time. Shielded simulations are denoted by solid lines, unshielded simulations by dashed lines. Both with and without shielding, as J_{XR} increases, the gas in the loitering phase becomes cooler. This lowers the Jeans mass, allowing the gas to collapse to high densities sooner.	58
3.8 Shown here are the Jeans mass (dotted lines) and total enclosed mass (solid lines) within a given radius for both the $J_{\text{XR}} = 0$ (upper panel) and $J_{\text{XR}} = 1000 J_0$ case (lower panel). Here we calculate the Jeans mass using the average density and temperature within that radius, extending out to the virial radius of the halo. The $J_{\text{XR}} = 0$ case is shown just prior to the formation of the first sink particle; the $J_{\text{XR}} = 1000 J_0$ case is shown at the maximum density reached over the course of the simulation.	62

3.9	Growth of individual sink particles over time. Sinks for the shielded simulations are coloured throughout in order of formation: blue, green, red, yellow, cyan, and purple. Lines end where one sink is accreted by another. The light grey lines show the growth history of sinks in the unshielded simulations for comparison. Note that in the absence of shielding, more sinks form, but the total mass remains roughly constant.	63
3.10	Density projection of the central 10000 AU of each simulation 5000 yr after formation of the first sink particle. From left to right: $J_{\text{XR}} = 0$, J_0 , $10 J_0$, $10^2 J_0$. Top row shows the face-on density projection; bottom row shows an edge-on projection. Black dots mark the location of all sink particles, and scale with the mass of the sink.	64
3.11	Total gas mass in successive radial bins of 500 AU centred on the highest density point in the simulation. Shown is the mass distribution just prior to the formation of the first sink particle.	65
3.12	The Toomre Q parameter versus radius shown 5000 yr after the first sink particle forms in each simulation. The accretion disc is susceptible to fragmentation when $Q \lesssim 1$, as is the case for the $J_{\text{XR}} = 0$ and $10 J_0$ cases.	66
3.13	From top to bottom: the rotational velocity, radial velocity, and Shu accretion rate versus distance to the centre of the minihalo for each simulation as denoted in the legend. The vertical gray line at 10^4 AU marks the approximate limit of the accretion disc, and the limit to which Figures 3.10, 3.11 and 3.12 are displayed. Note the significant discrepancies in the behaviour of the $J_{\text{XR}} = 10 J_0$ case in each panel.	67
4.1	Cosmic ray energy density u_{CR} as a function of redshift. Our models, from u_0 to $10^5 u_0$ are indicated by solid black lines, while the energy density in the CMB and the thermal energy density in the IGM are denoted by dashed and dotted black lines, respectively. The grey region shows the range of possible values for the magnetic field energy density in the IGM, and the dashed red line marks the most conservative upper limit on the CR energy density from Rollinde et al. (2006), as derived from the ${}^6\text{Li}$ abundance. Blue points indicate the redshift at which Halo 1 collapses to high densities for a given u_{CR} ; green points, the redshift at which Halo 2 collapses. Finally, purple points denote the energy densities employed by Stacy & Bromm (2007) to study the impact of a CR background using one-zone models calculated at $z = 21$	80

- 4.2 Ionisation and heating rates as a function of total gas number density for both a cosmic ray and an X-ray background at $z = 25$. In both panels, the solid blue lines denote the rate for our fiducial CR background, u_0 . The solid red lines show the fiducial X-ray rates from Hummel et al. (2015), while the dashed grey lines demonstrate the expected rates in the absence of gas self-shielding. The dash-dotted blue (red) lines mark the highest-intensity CR (X-ray) heating and ionisation rates investigated. For a given energy density, CRs are more effective at ionising and heating the gas; vertical placement on this chart is simply a matter of normalisation, stemming from the assumptions outlined in Section 4.2. Note that X-rays cause significantly more heating per ionisation event than CRs, but are strongly attenuated at high densities. CRs are significantly more penetrative in comparison.

4.3 Mass-weighted temperature-density distribution of the gas collapsing into Halo 1 (top) and Halo 2 (bottom), shown just prior to sink formation. Each panel shows the behaviour of gas collapsing under a CR background of a given strength. In each case, the behaviour of the gas in the $u_{\text{CR}} = 0$ case is reproduced for comparison (light grey); dashed lines denote the CMB temperature when collapse occurs. Gas at low densities gets progressively hotter and gas in the loitering phase gets progressively cooler with increasing u_{CR} . Note that the gas invariably proceeds to collapse, and converges toward a similar thermodynamic path as it approaches sink formation densities, regardless of the CR background strength.

4.4 From top to bottom, density-binned average gas temperature, H_2 fraction, and free electron fraction for both Halo 1 (left) and Halo 2 (right). As u_{CR} increases, the additional ionisation increases f_{e^-} , which in turn elevates f_{H_2} . Combined with the additional heating provided by the CR background, this allows H_2 cooling to activate at slightly lower densities and gas in the loitering phase to reach slightly lower temperatures, as seen in the top panel.

4.5 Total gas mass within 1 pc of the highest density point in each simulation over cosmic time. Top: Halo 1; bottom: Halo 2. As u_{CR} increases, the additional heating and ionisation allows the gas to fulfil the Rees-Ostriker criterion ($t_{\text{cool}} \lesssim t_{\text{ff}}$) sooner, expediting collapse to high densities. The sooner runaway collapse sets in, the less time gas has to accumulate in the centre of the minihalo, resulting in a lower total mass within 1 pc at simulation's end. The discontinuity seen in the growth of Halo 2 is a numerical artefact arising from the cut-out and refinement process.

4.6	Simulation structure for both Halo 1 (top) and Halo 2 (bottom) as seen in the final output, 5000 yr after the first sink forms. Shown is a density projection of the minihalo environment on progressively smaller scales for both the $u_{\text{CR}} = 0$ and $u_{\text{CR}} = 10^5 u_0$ simulations, as labelled. White boxes indicate the region depicted on the next smaller scale. From left to right: filamentary structure of the cosmic web near the minihalo formation site; minihalo formation at the intersection of several filaments; morphology within the ~ 100 pc virial radius of the minihalo. The density scale for each level is shown just to the right – note that the scaling changes from panel to panel. Note how the gas in the $u_{\text{CR}} = 10^5 u_0$ simulations appears smoothed out compared to the $u_{\text{CR}} = 0$ simulations. Not only do CRs heat and smooth the filamentary gas, the expedited collapse induced by CR ionisation leaves less time for low-density structure to form, since the collapse is shifted to an earlier epoch. As a result, the dynamical environment in which the sink particles form varies significantly between simulations.	93
4.7	Growth of individual sink particles in each simulation over time, with the first sink forming at $t = 0$. Lines end where one sink is accreted by another. The Halo 1 suite of simulations is shown in the left panel, Halo 2 in the right panel. The growth of the sinks in the corresponding $u_{\text{CR}} = 0$ is shown in grey in the background of each panel for comparison. There are no apparent trends with increasing u_{CR} – neither in typical sink mass nor in the number of fragments formed.	94
4.8	Density projection of the central 20 000 AU of each simulation 5000 yr after the formation of the first sink particle. Upper panel: Halo 1; lower panel: Halo 2. Each accretion disc is shown face-on; sink particle positions are identified by black dots whose size scales logarithmically with the mass of the sink. In each panel the accretion disk formed in the absence of any CR background is shown on the left; the corresponding u_{CR} -modified discs are shown to the right. Note the broad variation in both disc structure and spatial extent.	95
4.9	Density-binned average temperature (top) and Bonnor-Ebert mass (bottom) for Halo 1 (left) and Halo 2 (right) for all CR background strengths, as labelled. Overlaid on each panel are the one-zone calculations of Stacy & Bromm (2007), which only tracked the gas evolution up to densities of 10^6 cm^{-3} , insufficient to observe the u_{CR} -independent convergence in the thermodynamic state of the gas as it proceeds to runaway collapse.	97
5.1	Initializing a simulation, defining a <code>PartType</code> dataset, and loading data.	104

5.2	Loading non-standard particle fields and defining custom PartType classes. Within <code>gadfly</code> this is straightforward.	107
5.3	Unit handling in <code>gadfly</code> .	111
5.4	Example of a visualization produced by <code>gadfly</code> . This particular image shows the density distribution in a minihalo forming at $z = 25$ on 1 kpc scales, and is from a simulation run for Hummel et al. (2015).	113
A.1	Upper and lower limits for the number of PISNe per JWST FoV above redshift z with different feedback prescriptions. The observable numbers for a 10^6 s exposure assuming the He100 model are shown on the left; the R175 model is employed on the right. Solid blue lines show an upper limit to the observable number in the case of no feedback, solid red lines an estimate for the observable number in our conservative feedback scenario, and dashed red lines the number in the enhanced star formation case. Note that the x-axis is scaled independently in each panel.	120
A.2	Left: Lightcurves for the Kasen et al. (2011) He100 (top) and R175 (bottom) models as they would be observed by JWST’s F444W NIRCam filter at $z = 5, 10, 15, 20, 25$ and 30 . The flux limits for a 10^6 s (dashed line) and 10^4 s (dotted line) exposure are shown for reference. Right: The visibility time Δt_{vis} in years for He100 (top) and R175 (bottom) as a function of redshift for each of the NIRcam wide filters. Note that the axes are scaled independently.	121
A.3	The total number of PISNe observable with a campaign of 10^6 , 10^7 and 10^8 s (from top to bottom) as a function of total survey area for a given PISN model. In each case, the total campaign time is apportioned equally over the survey area to determine the exposure time for individual pointings. The blue region represents all PISNe, the red only PISNe from $z > 15$. Upper boundaries correspond to the no-feedback upper limit to the PISN rate and lower boundaries to the conservative feedback case. The dashed line marks one PISN visible. Note that not all axes are scaled the same.	122

Chapter One: Introduction

1.1 From the Big Bang to Now

How did we get here? This is one of the most fundamental questions humanity asks itself. At its most basic, this is also the question the field of cosmology attempts to answer: what is the origin of the Universe, how has it evolved over time, and what is its ultimate fate? Indeed, the past century has seen remarkable progress in this line of inquiry. Beginning with Einstein's publication of the general theory of relativity (Einstein, 1916), the past 100 years have seen our understanding of the Universe and our place in it revolutionized. In the mid-1920s we realized that the Universe is in fact much larger than just our Milky Way Galaxy (Hubble, 1925), and the diffuse nebulae observed by astronomers were actually (previously incomprehensibly) distant galaxies similar to our own. Starting with Hubble's 1929 discovery that the Universe is expanding (Hubble, 1929), and finally confirmed by Penzias and Wilson's detection of the Cosmic Microwave Background (CMB; Penzias & Wilson, 1965; Dicke et al., 1965), a strong body of evidence has led us to the conclusion that the Universe began in a Big Bang and has been expanding ever since. Other observations have since revealed that the overwhelming majority of the mass in the Universe is actually composed of invisible dark matter (Rubin et al., 1980), and the normal baryonic matter comprising all stars, planets, and every living thing accounts for only about a fifth of the total mass budget. In fact, normal matter constitutes an even smaller 4% of the total energy content of the Universe, with the majority consisting of dark energy, the phenomenon responsible for the observed acceleration of the Universe's

expansion (Riess et al., 1998; Perlmutter et al., 1999). Most recently the advent of precision cosmology, led by high resolution studies of the CMB, has allowed us to determine the age, composition, and shape of the Universe with multiple-digit precision. This has led to the conclusion that we live in a flat universe which is 13.8 billion years old and composed primarily of dark energy and dark matter (Ade et al., 2015).

While studies of the CMB have revealed much about the Universe on large scales, the CMB also provides a detailed picture of what the Universe looked like when atoms were first forming, \sim 400,000 years after the Big Bang. However, the Universe thus revealed had little in common with the Universe we observe today. At these early times, matter and radiation were distributed quite evenly, and deviations from perfect uniformity were only present on the level of one part in 100,000—a far cry from the complex, highly structured tapestry of planets, stars, and galaxies we see today. As even our deepest current observations reveal a Universe which is already highly structured, precisely how this transition occurred is one of the primary frontiers of modern cosmology.

When the next generation of astronomical facilities—including the *Square Kilometer Array* (SKA), *James Webb Space Telescope* (JWST), and 30-meter class ground-based telescopes like the *Giant Magellan Telescope* (GMT)—come online, they will allow us to peer much farther through space and time, opening even earlier epochs to observation. The JWST in particular is expected to reveal the formation of the first galaxies at $z \simeq 10$, and a detailed understanding of how these structures form will be crucial to interpreting the findings of these next-generation observatories. Coupled with ever more sophisticated simulations enabled by advances in both technology

and technique, we are rapidly approaching completion of a continuous timeline of cosmic history. By connecting *ab-initio*, state-of-the-art cosmological simulations of structure formation to next-generation observations we will for the first time be able to construct a complete picture of cosmic evolution, stretching all the way from the simple initial conditions of the early universe to the present epoch.

1.2 Cosmic Renaissance

The basic process by which the first stars and galaxies form has been thoroughly established within the standard Λ CDM model for hierarchical structure formation. Following the release of the CMB, cosmic evolution during the ‘dark ages’ was relatively simple, with small perturbations in the density of cold dark matter growing slowly under the influence of gravity. These over-densities eventually coalesce into gravitationally bound ‘minihalos’ within which the first stars formed roughly 100 million years after the Big Bang, initiating a cosmic ‘renaissance’ and marking a significant increase in the complexity of cosmic evolution (Barkana & Loeb, 2001; Miralda-Escudé, 2003; Bromm et al., 2009; Loeb, 2010). The light from these stars swept through the Universe, beginning the process of reionization (e.g., Meiksin, 2009), while the heavy elements forged in their cores and released in the violent supernova explosions marking their deaths began the process of chemical enrichment (e.g., Karlsson et al., 2013). Since structure in our Λ CDM Universe forms in a hierarchical manner, such that the dark matter halos hosting the first galaxies are built up from smaller progenitors which hosted the first stars, Pop III stars have a direct impact on the formation and evolution of all subsequent stages of galaxy formation, and thus are thus key drivers of cosmic evolution (Bromm, 2013).

The complex baryonic physics involved have so far prevented a definitive answer to this question, but the basic properties of these Pop III stars have been reasonably well established, with the consensus that the first stars formed in dark matter minihalos on the order of $10^5 - 10^6$ solar masses at redshifts $z \simeq 20 - 30$ (Couchman & Rees, 1986; Haiman et al., 1996; Tegmark et al., 1997). In the absence of any feedback, pioneering numerical work on the collapse of primordial gas into these halos, where molecular hydrogen is the only available coolant, suggested that the first stars were predominantly very massive, on the order of $100 M_{\odot}$ with a top-heavy initial mass function (IMF) (e.g., Bromm et al. 1999, 2002; Abel et al. 2002; Bromm & Larson 2004; Yoshida et al. 2006; O’Shea & Norman 2007). More recent work, aided by increased resolution, has revised this picture, finding that significant fragmentation occurs during the star formation process, resulting in lower characteristic masses and a much broader IMF than previously thought (Stacy et al., 2010; Clark et al., 2011a,b; Greif et al., 2011a, 2012; Stacy & Bromm, 2013; Hirano et al., 2014; Hosokawa et al., 2015). This has led to an emerging consensus that the Pop III initial mass function (IMF) was somewhat top-heavy with a characteristic mass of \sim a few $\times 10 M_{\odot}$ (Bromm, 2013).

While the formation of the very first stars is set by cosmological initial conditions, the formation of all subsequent generations is much more complex due to the feedback processes initiated by that very first episode of primordial star formation. The characteristic mass of the first stars is therefore crucial, as it largely determines the influence Pop III stars have on their environment, controlling both their total luminosity and ionizing radiation output (Schaerer, 2002), as well as the details of their eventual demise (Heger et al., 2003; Heger & Woosley, 2010; Maeder & Meynet, 2012), thus setting the initial conditions for the formation of the first galaxies.

1.3 The First Supernovae

One crucial element in any realistic model of galaxy formation is supernova (SN) feedback, both through direct radiative and mechanical feedback from the explosion itself, and via the chemical enrichment process. Supernova feedback is of particular importance in the early universe, as the first stars tended to be rather more massive than those formed today. In this thesis, we aim to better understand the role these violent explosions play in the formation of the first galaxies, particularly through radiative feedback.

Chapter 2 concerns the prospects for directly detecting the first supernovae. Stars in the mass range $140 - 260 M_{\odot}$ are expected to end their lives as extremely energetic Pair-Instability Supernovae (PISNe), which would be within the detection limits of the JWST even at $z = 30$. We tackle this question using a semi-analytic model to estimate the formation rate of minihalos hosting the first stars, coupled with a feedback prescription informed by simulations from Pawlik et al. (2011) to determine what fraction of these minihalos likely hosted a PISN. Given their brightness, the source density of these events is the limiting factor in their detection, even in the most optimistic scenario. We show that the optimal search strategy for finding a Pop III PISN is a mosaic-style search of many moderately deep exposures, as even rather high-redshift PISNe are unlikely to be missed, and a large area will need to be searched to ensure a detection. While scientific consensus on the characteristic mass of Pop III stars—and thus, the PISN rate—has shifted in recent years, PISNe will still occur, albeit at a lower rate.

Chapters 3 and 4 focus on the impact radiative feedback from the first supernovae has on star formation in neighboring minihalos. As these events occur in a

predominantly neutral medium, the vast majority of their ionizing output—both from the explosion itself, and the compact remnants left behind—is absorbed by the intergalactic medium (IGM). Consequently, most Pop III SN feedback is locally confined, similar to chemical feedback. However, the neutral hydrogen cross-section for X-rays and cosmic rays is small, allowing them to escape their host minihalos to build up an isotropic X-ray (Chapter 3) or cosmic ray (Chapter 4) background. This ionizing background radiation is then absorbed by high-density gas in neighboring minihalos, where it serves to enhance the ionization fraction. As free electrons are required to catalyze the formation of molecular hydrogen, which is the only available coolant in primordial gas, the presence of an ionizing background actually enhances the cooling efficiency of gas collapsing in pristine minihalos where no chemical enrichment has yet occurred. We show that for both moderate X-ray and cosmic ray backgrounds, this effect overwhelms the associated heating, resulting in a net cooling of the collapsing gas and expediting collapse to high densities. This effect is particularly pronounced for cosmic rays, as they cause very little heating per ionization event. The characteristic mass of the stars formed in the presence of such a background however appears to be quite robust, remaining stable even as the strength of the irradiating background varies by several orders of magnitude.

The primary tool employed throughout these investigations has been the numerical simulation of cosmological structure formation, specifically using the smoothed-particle hydrodynamics (SPH) simulation code GADGET-2 (Springel, 2005). Understanding the results of these simulations required a great deal of exploratory analysis, and in **chapter 5** we describe the novel software tools developed to enable this investigation, which have been released as the open-source GAdget DataFrame Library, or **gadfly**. The package is designed to leverage the capabilities of the broader python

scientific computing ecosystem, and provides a framework for analyzing particle-based GADGET and GIZMO (Hopkins, 2015) simulation data. `Gadfly` enables efficient memory management, includes utilities for unit handling, coordinate transformations, and parallel batch processing, and provides highly optimized routines for visualizing smoothed-particle hydrodynamics (SPH) datasets.

Chapter Two: The Source Density and Observability of Pair-Instability Supernovae from the First Stars

2.1 Introduction

Understanding the formation of the first stars and galaxies is one of the central challenges of modern cosmology, as they mark a significant increase in complexity from the simple initial conditions of the primordial universe during the ‘dark ages’ (e.g., Barkana & Loeb 2001; Miralda-Escudé 2003; Bromm et al. 2009; Loeb 2010). The basic properties of these so-called Population III (Pop III) stars have been reasonably well established, with the consensus that the first stars formed in dark matter ‘minihalos’ on the order of $10^5\text{--}10^6 M_\odot$ at high redshifts (Couchman & Rees, 1986; Haiman et al., 1996; Tegmark et al., 1997). Numerical simulations of the collapse of primordial metal-free gas into these halos, where molecular hydrogen is the only available coolant, had suggested that the first stars were predominantly very massive, with $M_* \gtrsim 100 M_\odot$ and a top-heavy initial mass function (IMF) (e.g., Bromm et al. 1999, 2002; Abel et al. 2002; Bromm & Larson 2004; Yoshida et al. 2006; O’Shea & Norman 2007). More recent work has found that the gas from which the first stars formed underwent significant fragmentation (Stacy et al., 2010; Clark et al., 2011b; Greif et al., 2011a, 2012), and experienced strong protostellar feedback (Hosokawa et al., 2011; Stacy et al., 2012a). These results have revised our picture of Pop III star formation, with lower characteristic masses (on the order of 50 rather than $100 M_\odot$)

and a much broader IMF now expected. The light from these stars ended the dark ages and fundamentally transformed the universe, beginning both the reionization (e.g, Meiksin 2009) and the chemical enrichment of the universe (e.g, Karlsson et al. 2013).

Given the top-heavy nature of Pop III star formation and the fact that low-metallicity stars are unlikely to undergo significant radiatively driven mass loss (Kudritzki, 2002), one interesting possibility is that some of the first stars died as pair-instability supernovae (PISNe), a scenario that has significant consequences for the chemical enrichment history of the universe (Heger & Woosley, 2002; Tumlinson et al., 2004; Karlsson et al., 2008). Basic one-dimensional models predict that stars with masses in the range $140\text{--}260 M_{\odot}$ will undergo a pair-production instability and explode completely (Barkat et al., 1967; Fraley, 1968). During core oxygen burning, a combination of high temperatures and relatively low densities results in the formation of e^{\pm} pairs, removing pressure support from the core. Following the subsequent contraction, the ignition of explosive oxygen burning completely disrupts the progenitor, resulting in a significant contribution to the metal enrichment of the surrounding medium. More recently, Chatzopoulos & Wheeler (2012) and Yoon et al. (2012) have found that stars with initial masses as low as $65 M_{\odot}$ can encounter the pair-production instability if they are rapidly rotating. In this scenario, strong rotationally induced mixing causes nearly homogeneous evolution, such that the star is converted almost entirely to helium before the next phase in its evolution begins. These extremely energetic explosions—approaching 10^{53} ergs for the most massive models—are very luminous, in part due to the large amount of ^{56}Ni produced, and are also very temporally extended as a result of the large mass ejected (Fryer et al., 2001; Heger & Woosley, 2002; Heger et al., 2003; Joggerst & Whalen, 2011; Kasen et al., 2011).

A second possibility for reaching such extreme explosion energies in slightly lower mass stars is the hypernova scenario for rapidly rotating stars that undergo core collapse (Umeda & Nomoto, 2003; Tominaga et al., 2007). During the collapse, accretion onto a central black hole powers a jet which induces a highly energetic explosion. While recent work has decreased the expected mass of the first stars, they have also been found to rotate more rapidly than previously thought (Stacy et al., 2011b), increasing the plausibility of this scenario. Evidence supporting this hypothesis has recently been presented by Chiappini et al. (2011).

While not an example of a Pop III star, the recent discovery of the extremely luminous supernova (SN) 2007bi, identified as a possible PISN, in a metal-poor dwarf galaxy at a redshift of $z \simeq 0.1$ (Gal-Yam et al., 2009) suggests that PISNe may be possible in the local universe under rare circumstances. Further supporting this picture, Woosley et al. (2007) have shown that SN 2006gy (Smith et al., 2007) is well modeled by a pulsational pair-instability model. For stars with initial masses in the range $\sim 100\text{--}140 M_\odot$, the star encounters the e^\pm production instability, but the resulting explosive ignition of oxygen is insufficient to unbind the star. Instead it ejects a shell of material before settling back into a stable configuration. The star encounters this instability several times until the mass of the helium core drops below $\sim 40 M_\odot$, after which the star can proceed to silicon burning and eventually undergo core-collapse.

With the upcoming launch of the *James Webb Space Telescope* (JWST) we will be able to probe the epoch of first light in unprecedented detail. While the first stars themselves are unlikely to be visible (e.g, Bromm et al. 2001; Pawlik et al. 2011), some of the SNe that end their lives should be within the detection limits of the JWST

(e.g., Mackey et al. 2003; Scannapieco et al. 2005; Gardner et al. 2006). While the basic properties of PISNe and the effect they have on their environment has been well studied (Mori et al., 2002; Bromm et al., 2003; Furlanetto & Loeb, 2003; Kitayama & Yoshida, 2005; Whalen et al., 2008; Wise & Abel, 2008; Greif et al., 2010), the source density of these events has yet to be well constrained.

The first attempt at estimating the number and observability of SNe at high redshift was made by Miralda-Escudé & Rees (1997), who calculated the all-sky SN rate based on estimates of the total metals produced by a typical SN and the observed metallicity of the intergalactic medium (IGM) at high redshifts. This yields ~ 1 SN yr^{-1} arcmin^{-2} at $z \sim 5$. Other early work attempted to model the SN rate based on the empirically determined star formation rate out to high redshifts ($z \sim 5$; e.g., Madau et al. 1998; Dahlén & Fransson 1999). It should be noted that these attempts focused on Type II SNe, not PISNe, which are the focus of the present work. Mackey et al. (2003) estimated the PISN rate based on their calculations of the Pop III star formation rate, predicting $\sim 2 \times 10^6$ PISNe yr^{-1} over the whole sky above $z = 15$. Weinmann & Lilly (2005) performed a similar analysis with more conservative estimates for the star formation rate, finding a PISN rate of ~ 4 yr^{-1} deg^{-2} above $z = 15$ and ~ 0.2 yr^{-1} deg^{-2} above $z = 25$, as well as concluding that PISNe should be observable out to $z = 50$ with the JWST.

Subsequent work by Wise & Abel (2005) determined the PISN rate based on the collapse of gas into dark matter minihalos. Accounting for radiative feedback, they concluded that ~ 0.34 PISNe yr^{-1} deg^{-2} were to be expected above $z = 10$, as well as briefly considering the detectability of PISNe at high redshifts based on models from Heger & Woosley (2002). Scannapieco et al. (2005) presented a more

thorough analysis of the visibility of PISNe based on a suite of numerical simulations spanning the range of theoretical PISN models using the implicit hydrodynamics code KEPLER. Mesinger et al. (2006b) presented a similar but more general halo mass function based analysis, considering the rates and detectability of all SNe; they briefly consider primordial PISNe, but focus on core-collapse SNe and their detectability. More recently, Trenti et al. (2009) explored the observable PISN rate within the context of the metal-free gas supply during the epoch of reionization.

Our work improves upon these investigations by incorporating updated PISN models from Kasen et al. (2011) and determining their observability using the published specifications of the Near Infrared Camera (NIRcam) on the JWST¹. In the final stages of the work on this paper we have become aware of the study by Pan et al. (2012), who have performed a similar analysis. This paper addresses the question of PISN observability in a nicely complementary way by employing a different normalization strategy. Different from our assumption that viable Pop III progenitors can only form in unenriched minihalos at $z \gtrsim 6$, Pan et al. (2012) derive the star formation rates required to produce sufficient photons for reionization. They then infer the PISN rate corresponding to different choices for the IMF. Their analysis is thus able to probe the character of star formation in the dwarf galaxies that are the main drivers of reionization, whereas we focus on the minihalos where Pop III stars first begin to form.

This paper is organized as follows. In Section 2 we describe our semi-analytic model for the PISN rate. We consider the ability of the JWST to detect PISNe at high redshift in Section 3, and our conclusions are gathered in Section 4. Through-

¹<http://www.stsci.edu/jwst/instruments/nircam>

out this paper we adopt a Λ CDM model of hierarchical structure formation, using cosmological parameters consistent with the WMAP 5-year results (Komatsu et al., 2009): $\Omega_m = 0.258$; $\Omega_\Lambda = 0.742$; $\Omega_b = 0.0441$; $h = 0.719$; $n_s = 0.96$; $\sigma_8 = 0.796$.

2.2 The PISN Rate

PISNe are produced only by very massive stars (Bromm et al., 2001; Schaerer, 2002; Heger et al., 2003), which are now expected to be rare even for Pop III star formation. After the first massive star forms, the resulting heating from photoionization quickly suppresses the density of the remaining gas in the minihalo, effectively halting star formation (Kitayama et al., 2004; Whalen et al., 2004; Alvarez et al., 2006). The energy released by the first PISN disperses the gas in the halo and contaminates it with metals (Bromm et al., 2003; Greif et al., 2007; Whalen et al., 2008; Wise & Abel, 2008; Greif et al., 2010). Subsequent episodes of star formation are thus delayed until the gas is able to recondense into more massive cosmological halos (Yoshida et al., 2004, 2007; Johnson et al., 2007; Alvarez et al., 2009). While star formation will resume at this point, the gas in these systems is expected to be enriched beyond the critical metallicity for the transition to Population II (Pop II) star formation (Wise & Abel, 2007, 2008; Greif et al., 2007, 2008, 2010). As a result, the stars that form will no longer be massive enough to reliably produce PISNe. These explosions are thus only expected to occur in minihalos containing pristine gas that has just crossed the density threshold for star formation via H₂ cooling, and only one PISN occurs per halo.

It is possible that the first stars formed in binaries or small multiples; however, the number of massive stars formed per minihalo is still of order unity (Stacy et al.,

2010; Clark et al., 2011b; Greif et al., 2011a). Given this, and assuming that the time required for the progenitor star to form, live and die is negligible (Heger et al., 2003), we can use the formation rate of minihalos to place a robust upper limit on the PISN rate.

The introduction of cosmic feedback has the potential to significantly alter this picture. Chemical enrichment induces a transition to lower mass Pop II star formation, and thus always has a negative effect on the PISN rate. Radiative feedback—especially H₂-dissociating Lyman-Werner (LW) feedback—has a more complicated effect. The destruction of molecular hydrogen by LW photons removes the ability of pristine gas to cool effectively. This suppresses star formation, and hence negatively affects the PISN rate. However this merely delays star formation; as the halo mass continues to increase, the gas eventually becomes self-shielding and proceeds with cooling and collapse. The delay effectively increases the amount of gas available when star formation begins. This increases the possibility of multiple massive stars forming simultaneously, positively affecting the PISN rate. To account for these possibilities, we consider three scenarios. First we estimate the PISN rate assuming that the first stars form unimpeded by cosmic feedback. Then we consider a conservative scenario in which both chemical and LW feedback affect the PISN rate, but only one star forms per halo. Finally, we allow for enhanced massive star formation in the LW-affected halos, and calculate the observable rate for each scenario.

2.2.1 No-Feedback Limit

In order to determine an upper limit to the PISN rate, we assume exactly one PISN per minihalo, forming as soon as the virial temperature of the minihalo exceeds the minimum value T_{crit} required for gas to cool and collapse to high densities. We set

this to 2200 K based on the results of simulations (see Section 2.2.2.1 for details).

The corresponding critical mass for collapse is given by

$$M_{\text{crit}} = 10^6 M_{\odot} \left(\frac{T_{\text{crit}}}{10^3 \text{K}} \right)^{3/2} \left(\frac{1+z}{10} \right)^{-3/2}, \quad (2.1)$$

where we assume a mean molecular weight of $\mu = 1.22$, appropriate for the almost completely neutral IGM at high redshifts (Barkana & Loeb, 2001).

We use the analytic Press-Schechter (PS) formalism for structure formation (Press & Schechter, 1974) to estimate the number density n_{PS} of minihalos of mass M at redshift z , given by

$$n_{\text{PS}}(M, z) = \sqrt{\frac{2}{\pi}} \frac{\rho_m}{M} \left| \frac{d \ln \sigma_0(M)}{d \ln M} \right| \nu_{c,z} e^{-\nu_{c,z}^2/2}, \quad (2.2)$$

where ρ_m is the background matter density, $\sigma_z(M)$ is the standard deviation of overdensities δ of mass M at redshift z , and $\nu_{c,z} = \delta_c/\sigma_z(M)$, where δ_c is the critical overdensity for collapse; the value used here is $\delta_c = 1.686$.

Converting from redshift to cosmic time $t(z)$, where

$$t(z) = \frac{1}{H_0} \int_z^\infty \frac{dz'}{(1+z')\sqrt{\Omega_m(1+z')^3 + \Omega_\Lambda}}, \quad (2.3)$$

a first order estimate for the PISN formation rate as a function of redshift is given by $\dot{n}_{\text{PISN}} \equiv dn_{\text{PS}}/dt$. However, this estimate is only valid while the rate of destruction of minihalos via mergers remains small compared to the formation rate. The Press-Schechter formalism only gives the total number of halos of a given mass at a given redshift. As a result, once mergers become important the rate of change of the total number of minihalos no longer traces the formation rate. To correct for this, we use the expression for the formation rate derived by Sasaki (1994)²:

$$\dot{n}_+(z) = \frac{\dot{D}}{D} n_{\text{PS}}(M_{\text{crit}}, z) \frac{\delta_c^2}{\sigma_0^2(M) D^2}, \quad (2.4)$$

²See Mitra et al. (2011) for a discussion of the validity of this expression.

where $D(z)$ is the growth factor. The PISN rate in this upper limit of no feedback, shown in Figure 2.2 (blue line), is then simply given by the halo formation rate:

$$\dot{n}_{\text{PISN}}(z) = \dot{n}_+(z). \quad (2.5)$$

2.2.2 Feedback

The preceding analysis has only nominally incorporated the baryonic physics involved through the critical mass for H_2 cooling. Gas will not successfully cool and collapse in all minihalos that reach the critical mass (e.g., Yoshida et al. 2003). The various feedback mechanisms responsible for this include photoheating from stars in nearby halos and the buildup of a background of H_2 dissociating LW photons. Chemical feedback will enrich the gas with metals, improving its ability to cool. However, gas that is enriched forms lower-mass Pop II stars, effectively reducing the PISN rate. These feedback mechanisms can be represented with distinct efficiency factors $\eta(z)$, such that the true PISN rate will be given by

$$\dot{n}_{\text{PISN}}(z) = \eta_{\text{chem}}(z) \eta_{\text{rad}}(z) \dot{n}_+(z). \quad (2.6)$$

We must include these effects in order to derive a realistic estimate for the PISN rate, which we henceforth refer to as the conservative feedback case.

2.2.2.1 Lyman-Werner Feedback

LW feedback is of particular importance in any discussion of feedback on the first stars as it dissociates the H_2 molecules primarily responsible for cooling primordial gas. This significantly reduces the ability of the gas to cool and works to suppress further star formation (Haiman et al., 1997; Omukai & Nishi, 1999; Ciardi et al., 2000; Haiman et al., 2000; Glover & Brand, 2001; Kitayama et al., 2001; Machacek

et al., 2001; Ricotti et al., 2001, 2002a,b; Yoshida et al., 2003; Omukai & Yoshii, 2003; Mesinger et al., 2006a). As the first stars form in $\gtrsim 3\sigma$ peaks in the Gaussian distribution of density fluctuations (Barkana & Loeb, 2001), we focus here on a similarly overdense environment in order to provide a conservative estimate of the effects of LW feedback on the PISN rate. While representative of the LW background in Pop III star formation sites, this is likely not representative of the ‘average’ LW background in the universe (e.g., Machacek et al. 2001; Mesinger et al. 2006a).

We will describe our radiative feedback simulations in detail elsewhere, and present only a brief summary here. We employ a set of two cosmological simulations using a modified version of the *N*-Body/TreePM SPH code GADGET (Springel, 2005; Springel et al., 2001a) to gauge the effects of LW feedback on the PISN rate. These simulations, carried out in a box of size $3.125 h^{-1}$ comoving Mpc and starting from a redshift of $z = 127$, were performed to investigate the formation of the first dwarf galaxies in $10^9 M_\odot$ halos at $z = 10$. In order to obtain high resolution in the halo containing the first galaxy while retaining information about structure on large scales, a zoomed simulation technique was used, with the highest resolution dark matter (gas) particles having a mass of 2350 (484) M_\odot . This allows halos with masses $\gtrsim 2 \times 10^5 M_\odot$, to be resolved with $\gtrsim 100$ dark matter particles.

The first of the simulations we employ is similar to simulation *Z4* presented in Pawlik et al. (2011), and follows the non-equilibrium chemistry and cooling of the primordial atomic and molecular gas, including star formation but not the associated feedback. It thus provides a useful reference against which the effects of LW feedback can be discussed. Here, gas particles were turned stochastically into star particles at densities $n_H > 500 \text{ cm}^{-3}$ on a dynamical time scale. Star particles were consid-

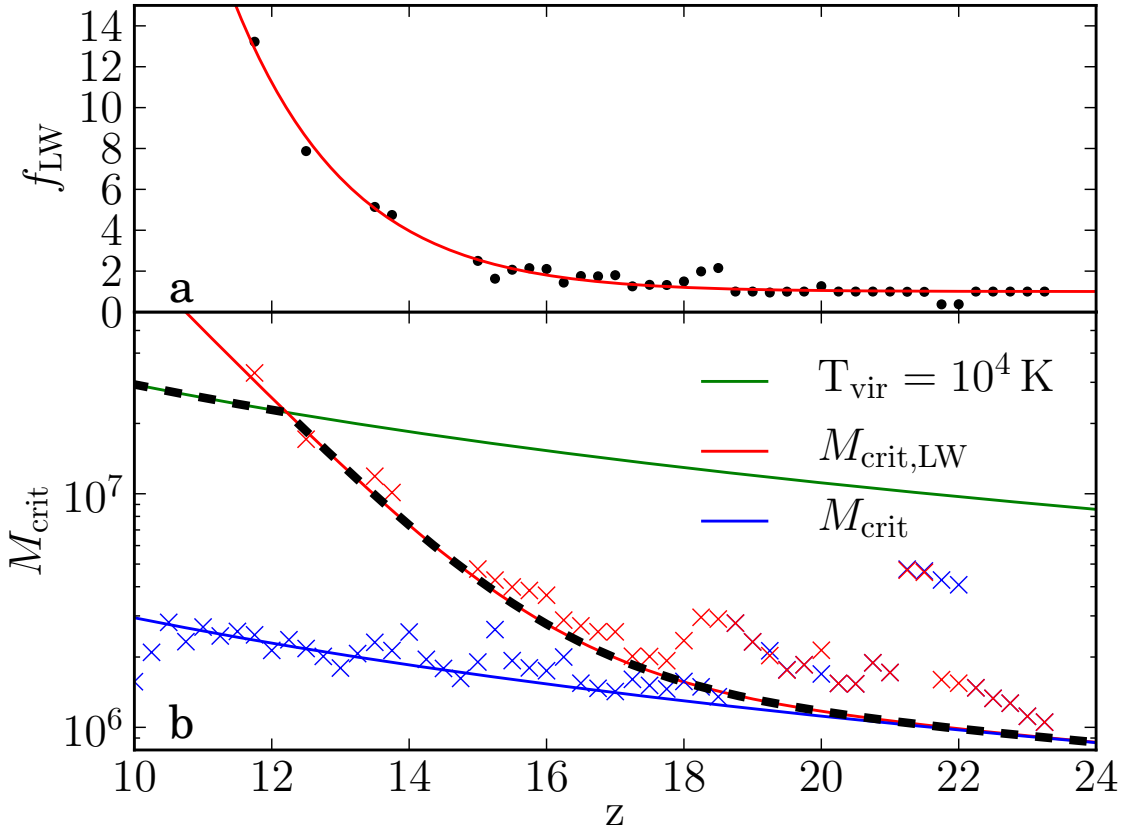


Figure 2.1: a) the factor f_{LW} by which LW feedback increases the critical mass for star formation; points show the results of the simulation, the red line our fit. b) The critical mass for star formation in both simulations. Blue crosses mark the critical mass for star formation in the absence of LW feedback, red crosses in its presence. The blue line shows the best fit critical mass from Eq. (2.1), given by a temperature of 2200 K; the red line the critical mass from Eq. (2.9) for LW feedback using the fit for f_{LW} given in Eq. (2.8). The green line marks the halo mass corresponding to a virial temperature of 10^4 K, and the black dashed line represents the critical mass employed, accounting for atomic cooling in halos with virial temperatures above 10^4 K.

ered simple stellar populations using the zero-metallicity top-heavy IMF models from Schaefer (2003). Henceforth this simulation is referred to as Simulation A.

The second simulation employed here, which we refer to as Simulation B, is identical to Simulation A except for the inclusion of LW feedback. Calculation of the feedback was carried out by considering the contribution from both star particles and a uniform LW background. The combined LW background is normalized to approximate the LW background evolution shown in Greif & Bromm (2006) in the optically thin limit, but with the application of a self-shielding correction (Wolcott-Green et al., 2011).

The efficiency of LW feedback, η_{LW} , can be expressed as the ratio of the formation rate of minihalos at the critical mass with LW feedback to that without:

$$\eta_{\text{LW}}(z) = \frac{\dot{n}_+(M_{\text{crit,LW}}, z)}{\dot{n}_+(M_{\text{crit}}, z)}. \quad (2.7)$$

This requires determining the factor $f_{\text{LW}}(z)$ by which LW feedback increases the critical mass for star formation. We do this by determining the critical mass required for stars to form in both simulations, as traced by the lowest mass halo that is actively forming stars for the first time. The resulting critical mass in each case is shown in Figure 2.1b; blue points denote the critical mass in Simulation A, red points in Simulation B. Without any negative feedback, we expect stars to form when the halo reaches the critical mass given in Eq. (2.1). We find the that the resulting critical mass in Simulation A is best fit by a critical virial temperature of 2200 K, as shown in Figure 2.1b. Note that this includes the effects of dynamical heating; gas in isolated halos would collapse and form stars at lower masses.

Determining the critical mass for star formation in the LW feedback simulation

in the same manner as above, we can then determine f_{LW} , shown in Figure 2.1a. We find that f_{LW} is well fit by a functional form of

$$f_{\text{LW}}(z) = -6.23 \times 10^{-5} \operatorname{erf}[0.094(z - 0.204)] + 6.23 \times 10^5, \quad (2.8)$$

for $z \geq 10$, where $\operatorname{erf}(z)$ is the error function. $M_{\text{crit,LW}}$ is then given by

$$M_{\text{crit,LW}} = f_{\text{LW}} M_{\text{crit}}, \quad (2.9)$$

shown in Figure 2.1b. When the virial temperature of the halo reaches 10^4 K, cooling via atomic hydrogen becomes efficient and molecular hydrogen becomes unimportant. Once this threshold is reached, LW feedback cannot further suppress star formation, and $M_{\text{crit,LW}}$ holds steady at a constant virial temperature of 10^4 K. This is reflected as an increase in the formation rate of halos affected only by LW feedback, as the formation rate of atomic cooling halos is increasing prior to $z = 10$. This transition can be clearly seen in Figure 2.2, marked by a sudden jump in the halo formation rate. As ionizing photons cannot easily escape the immediate vicinity of the star that produced them, their impact on neighboring halos is small compared to that of LW photons at the highest redshifts. We thus set $\eta_{\text{rad}} \simeq \eta_{\text{LW}}$ for simplicity. This approximation becomes increasingly unphysical close to the epoch of reionization at $z \sim 10$.

2.2.2.2 Chemical Feedback

The process of chemical enrichment is another crucial factor for determining the PISN rate. Gas that has been enriched beyond a critical metallicity of $Z_{\text{crit}} \sim 10^{-4} Z_{\odot}$ will no longer form Pop III stars (Bromm et al., 2001; Schneider et al., 2002; Bromm & Loeb, 2003), and hence no PISNe. Chemical feedback can thus be represented as

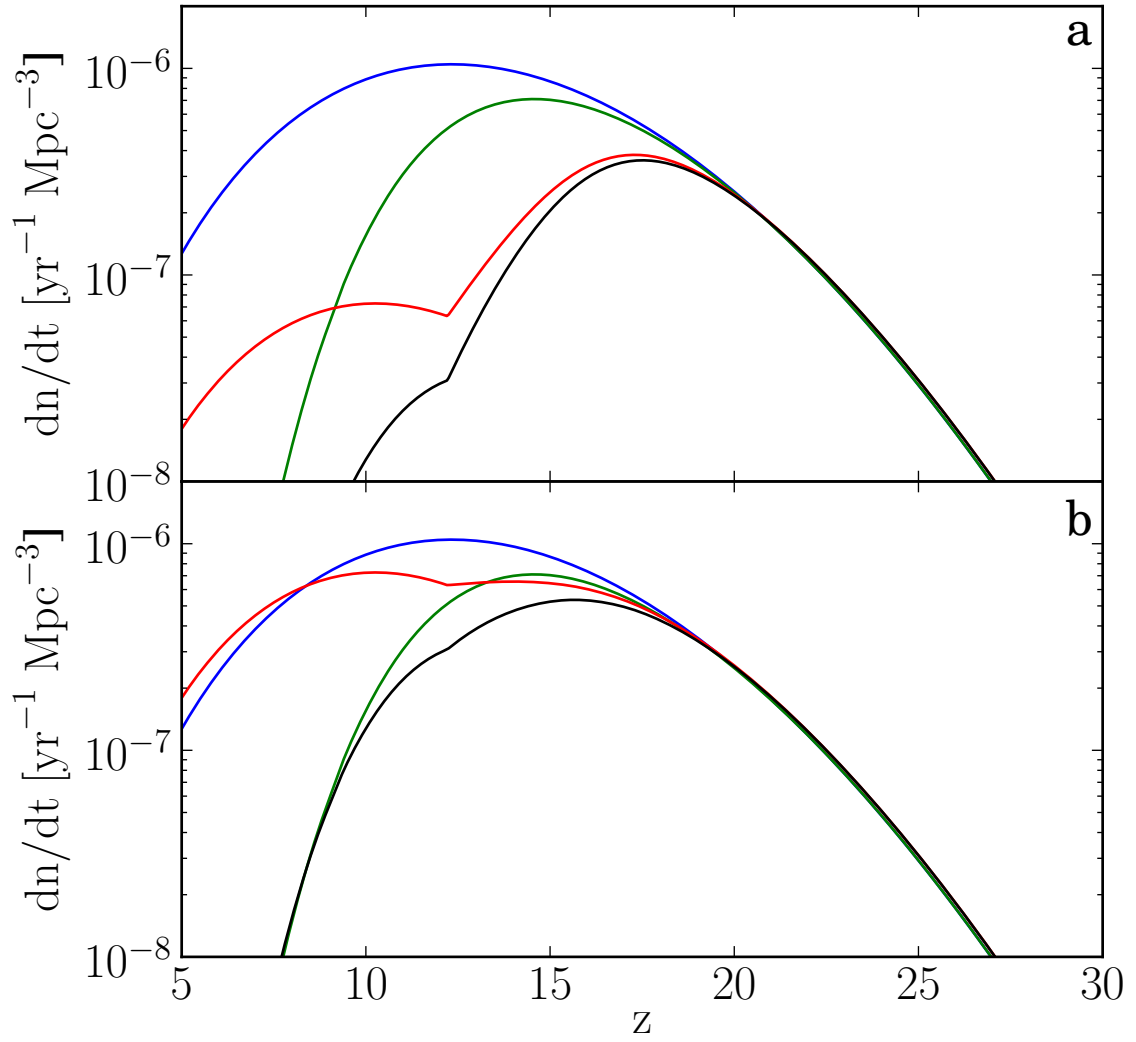


Figure 2.2: a) \dot{n}_{PISN} in the upper limit of no feedback (blue), with chemical feedback (green), LW feedback (red) and the resulting PISN rate for the conservative (chemical plus LW) feedback case (black). b) Same as (a), but for enhanced massive star formation.

the fraction of halos forming from pristine gas at a given redshift. Realistic three-dimensional simulations of this process starting from cosmological initial conditions have become possible in the past decade, showing that enrichment by Pop III SNe, if they are highly energetic, proceeds very inhomogeneously, enriching the IGM before penetrating into denser regions (Scannapieco et al., 2005; Greif et al., 2007; Tornatore et al., 2007; Wise & Abel, 2008; Maio et al., 2010).

In modeling η_{chem} , we use the results of Furlanetto & Loeb (2005). Their semi-analytic treatment of SN winds utilizes the Sedov (1959) solution for an explosion expanding into a uniform medium and yields a probability function $P_{pristine}(z)$ that the gas in a newly formed halo is pristine. This is plotted in Figure 2 of their paper for various strengths of chemical feedback. We identify this quantity as the fraction of newly collapsed halos that have been polluted with metals, η_{chem} . Given the recent detection of pristine gas at $z = 3$ by Fumagalli et al. (2011), we choose the weakest feedback scenario presented by Furlanetto & Loeb (2005) among the scenarios that incorporate a clustering of sources. The resulting PISN rate is given by the green line in Figure 2.2.

2.2.3 Enhanced Massive Star Formation

Gas cooling and subsequent star formation in halos affected by LW feedback can be delayed until nearly an order of magnitude more gas is available for star formation (Figure 2.1). This increases the likelihood that multiple massive stars form per halo, offsetting the negative effects of LW radiation considered above. We quantify this by positing that the number of PISNe produced per halo at redshift z is given by the ratio of the critical mass in the presence of LW feedback $M_{crit,LW}$ to the critical mass in the no-feedback case M_{crit} . For example, at $z = 17$, $M_{crit,LW}/M_{crit} \approx 1.4$, so for

every 10 pristine halos that form, 14 PISNe are produced. In this case the PISN rate is modified such that

$$\dot{n}_{\text{PISN}}(z) = \frac{M_{\text{crit,LW}}(z)}{M_{\text{crit}}(z)} \eta_{\text{chem}}(z) \eta_{\text{rad}}(z) \dot{n}_+(z). \quad (2.10)$$

The resulting enhanced PISN rate can be seen in Figure 2.2b. In contrast to the conservative feedback case, the net effect of LW feedback is much less significant here, with chemical feedback controlling the final PISN rate.

2.2.4 The Observable Rate

The observed PISN rate per unit time per unit redshift per unit solid angle is given by

$$\begin{aligned} \frac{dN}{dt_{\text{obs}} dz d\Omega} &= \frac{dN}{dt_{\text{obs}} dV} \frac{dV}{dz d\Omega} \\ &= \frac{1}{(1+z)} \frac{dN}{dt_{\text{em}} dV} r^2 \frac{dr}{dz}. \end{aligned} \quad (2.11)$$

Cosmological time dilation between t_{obs} and t_{em} is accounted for by the $(1+z)$ in the denominator; dV is the comoving volume element and $r(z)$ is the comoving distance to redshift z given by

$$r(z) = \frac{c}{H_0} \int_0^z \frac{dz'}{\sqrt{\Omega_m(1+z')^3 + \Omega_\Lambda}}, \quad (2.12)$$

where c/H_0 is the Hubble distance. With the assumptions outlined above, we estimate the PISN rate in events per year per comoving Mpc^3 in the source rest frame:

$$\frac{dN}{dt_{\text{em}} dV} = \dot{n}_{\text{PISN}}(z). \quad (2.13)$$

These results—shown in Figure 2.3—are in reasonable agreement with previous work; our no-feedback limit of one PISN per minihalo is somewhat more conservative than that employed by Weinmann & Lilly (2005), but in general agreement. Likewise, our

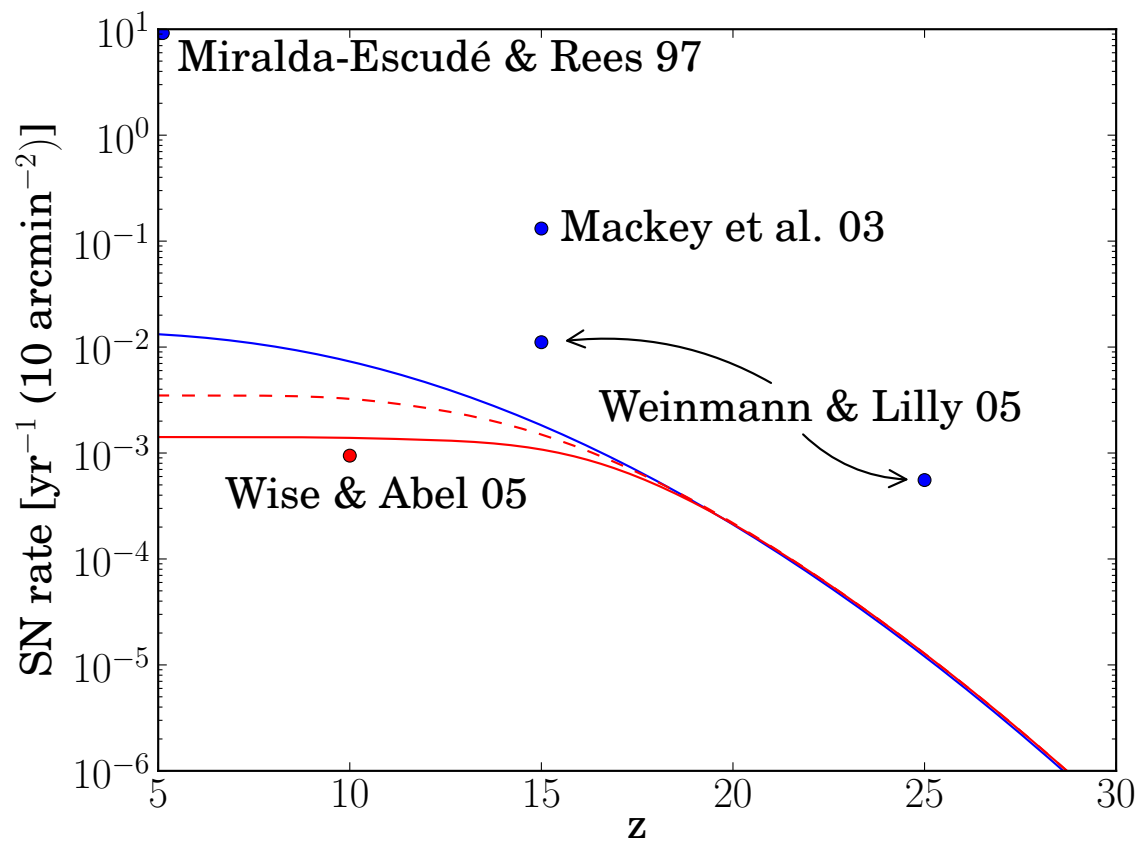


Figure 2.3: The observable PISN rates in number per year per JWST field of view above a given redshift in the upper limit of no feedback (blue line), in the conservative feedback case (solid red line), and the enhanced star formation case (dashed red line). The rates calculated by Miralda-Escudé & Rees (1997), Mackey et al. (2003), Weinmann & Lilly (2005) and Wise & Abel (2005) are also shown for reference. Red points account for feedback; blue points do not.

conservative feedback rate is in good agreement with the rate found by Wise & Abel (2005), which also accounted for feedback. The discrepancy with the remaining rates can be attributed to the fact that Mackey et al. (2003) employed an optimistic star formation efficiency of $\eta_* = 0.10$, while Miralda-Escudé & Rees (1997) performed a rough estimate of the all-sky supernova rate based on the observed metallicity of the IGM. This estimate of course includes Population I and II supernovae in addition to PISNe, and is included only for reference.

2.3 JWST Observability

While PISN explosions are predicted to be extremely energetic, the highest redshift events will still be unobservable, and those at lower redshifts will be above the detection limits of the JWST for only a fraction of their lifetimes. To determine the observability of these explosions we must consider both how bright they will be at a given redshift and how long they will remain visible. To span the uncertainties arising from variation in the progenitors of PISNe we consider a set of four models from Kasen et al. (2011), namely their R250, B200, R175 and He100 models. R250 and R175 are red supergiants of $250 M_\odot$ and $175 M_\odot$, respectively, spanning the mass range of successful explosions. We also consider a more compact $200 M_\odot$ blue supergiant (B200) and a $100 M_\odot$ bare helium core (He100). All models considered here die as PISNe, with explosion energies ranging from 7×10^{52} ergs (R250) to 2×10^{52} ergs (R175). The late-time luminosity is powered by the decay of ^{56}Ni produced during the explosion. $40 M_\odot$ of ^{56}Ni are produced in the R250 model, while only 5, 2 and $0.7 M_\odot$ are produced in He100, B200 and R175, respectively.

Bare helium cores, such as the He100 model, are of particular interest in light

of recent work finding that rapidly rotating stars can encounter the pair-production instability in progenitors with masses as low as $65 M_{\odot}$ (Chatzopoulos & Wheeler, 2012; Yoon et al., 2012). Combined with recent work finding that Pop III stars are both less massive and more rapidly rotating than previously thought (Stacy et al., 2010, 2011b, 2012a; Clark et al., 2011b; Greif et al., 2011a, 2012), the explosion of a rapidly rotating helium core formed by homogeneous evolution represents an intriguing possibility.

We first describe our technique for fitting a blackbody to these four PISN models before considering their visibility with the JWST. We then estimate the total observable number in each case and for each feedback prescription. Finally, we briefly discuss the challenges involved in actually identifying PISNe as such.

2.3.1 A Simple Lightcurve Model

In order to determine how long a PISN will be visible we must model the source spectrum. Given the large mass involved, the ejecta will remain optically thick until late times, so we make the reasonable assumption that the PISN emits as a blackbody for the majority of its visible lifetime. Using the U, B, V, R, I, J, H, and K absolute magnitude light curves presented in Kasen et al. (2011), we perform a least-squares fit to find the combination of temperature T and radius R_{SN} that best matches the broadband magnitudes at each point in time. This is done with the assumption that the specific luminosity of the PISN $L_{\text{SN},\lambda}$ at wavelength λ is given by

$$L_{\text{SN},\lambda} = 4\pi^2 R_{\text{SN}}^2 B_{\lambda}(T), \quad (2.14)$$

where B_{λ} is the Planck function. The resulting fits for the evolution of the temperature and radius of the PISN models are shown in Figure 2.4. Note that our blackbody

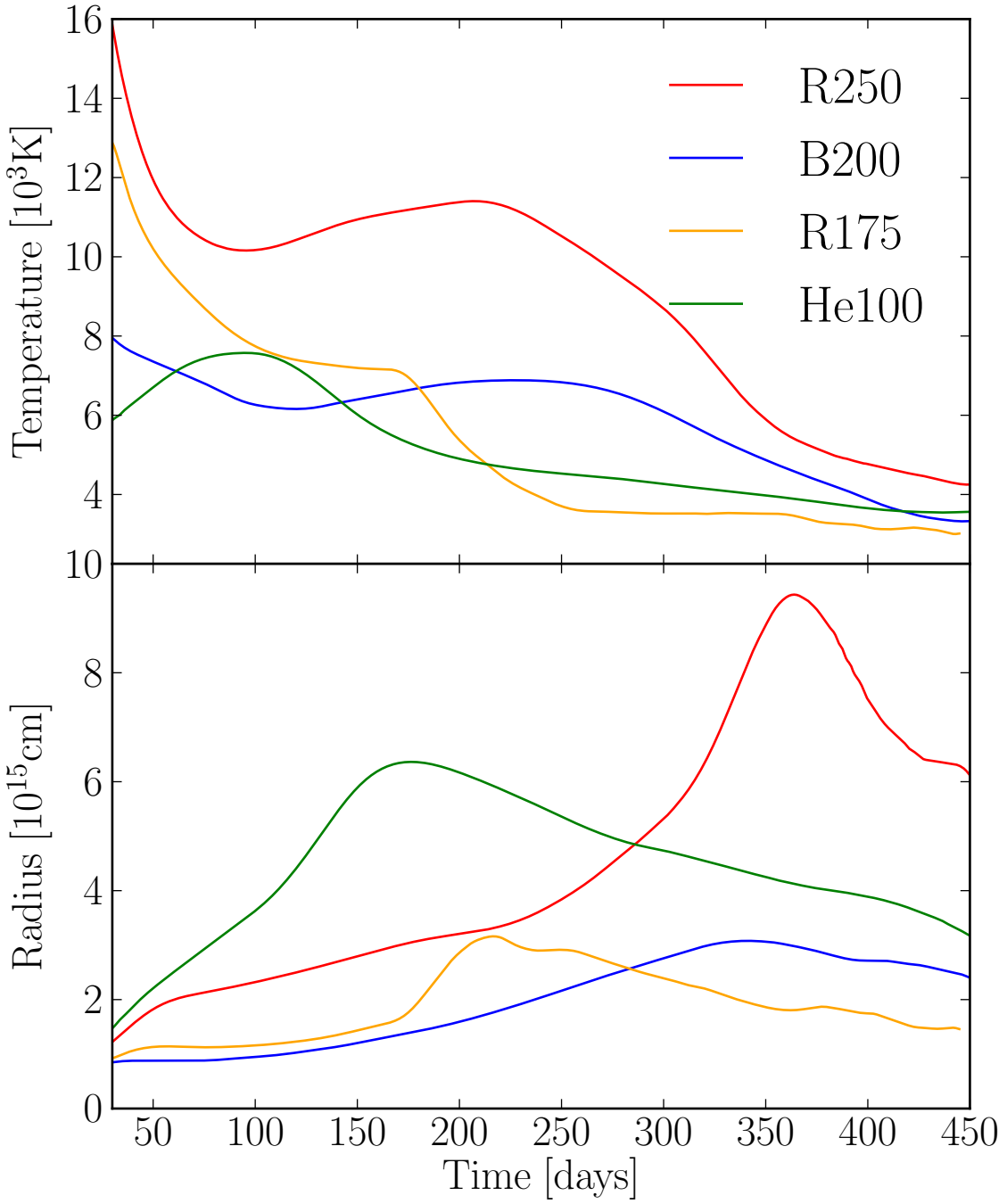


Figure 2.4: The temperature and radius of our blackbody fits as a function of source frame time since the explosion for models R250, B200, R175 and He100. The secondary rise in temperature seen in R250 and B200 is caused by the decay of ^{56}Ni reheating the ejecta at late times. Note also that the apparent radii begin to decrease again at late times; this can be interpreted as the photosphere receding into the ejecta as the material cools.

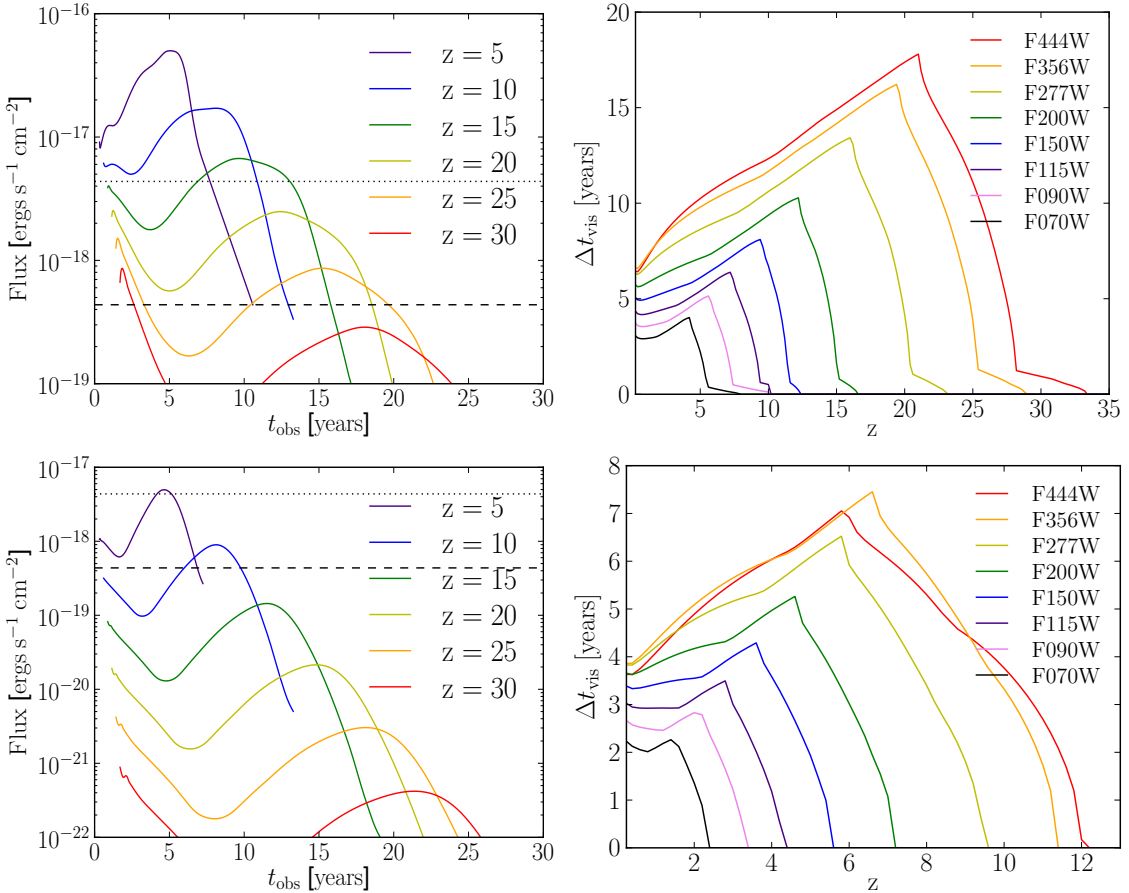


Figure 2.5: Left: Lightcurves for the Kasen et al. (2011) R250 (top) and B200 (bottom) models as they would be observed by JWST’s F444W NIRCam filter at $z = 5, 10, 15, 20, 25$ and 30 . The flux limits for a 10^6 s (dashed line) and 10^4 s (dotted line) exposure are shown for reference. Right: The visibility time Δt_{vis} in years for R250 (top) and B200 (bottom) as a function of redshift for each of the NIRcam wide filters. Note that the axes are scaled independently. Similar plots for models He100 and R175 are included in the appendix.

assumption breaks down at late times when the photosphere begins to recede into the ejecta. This is manifested as an apparent decrease in the radius of the PISN remnant.

With this information we can then calculate the specific flux $F_{\lambda,\text{em}}$ in the rest frame and—accounting for redshift and cosmological dimming—in the observer’s frame for

a source at redshift z :

$$F_{\lambda,obs}(T, R_{\text{SN}}, z) = \pi \left[\frac{R_{\text{SN}}}{D_L(z)} \right]^2 \frac{B_{\lambda'}(T)}{1+z}. \quad (2.15)$$

Here $\lambda' = \lambda/(1+z)$ accounts for redshifting, and the luminosity distance $D_L = (1+z)r(z)$ accounts for cosmological dimming. Convolving this spectrum with a filter function $\phi_x(\lambda)$ yields the observable flux in filter X:

$$F_{obs,x} = \int_0^\infty \phi_x(\lambda) F_{\lambda,obs}(T, R_{\text{SN}}, z) d\lambda. \quad (2.16)$$

2.3.2 Visibility

The NIRCam instrument on the JWST will observe the early universe through a number of narrow, medium-width, and wide filters³. The widest, longest-wavelength filter, F444W, will observe from 3.3 to 5.6 μm with a sensitivity limit of 24.5 nJy required for a 10σ detection in 10^4 seconds (Gardner et al., 2006). Shown in the left-hand column of Figure 2.5 is the observable flux as it would appear in the F444W NIRCam filter at various redshifts for the most and least easily observable models, R250 and B200, respectively. See Figure 2.7 for why these two were chosen; models He100 and R175 can be found in the appendix. The flux limits for the filter of $4.4 \times 10^{-19} \text{ erg s}^{-1} \text{ cm}^{-2}$ for a 10^6 s exposure and $4.4 \times 10^{-18} \text{ erg s}^{-1} \text{ cm}^{-2}$ for a 10^4 s exposure are also shown for reference. We see that the brightest explosions (R250) would be visible to beyond $z \sim 25$, but are never so bright as to be detectable with current generation telescopes. This is consistent with the non-detection by Frost et al. (2009) in a search of the *Spitzer*/IRAC Dark Field for possible Pop III PISN candidates.

³<http://www.stsci.edu/jwst/instruments/nircam/instrument-design/filters>

To account for absorption of flux by neutral hydrogen along the line of sight we implement a simple model of instant reionization at $z = 10$. For sources above this redshift, we assume no flux is observed shortward of the rest frame Ly α line. This is not relevant for the F444W NIRcam filter as Ly α does not redshift into the filter until $z \sim 40$, when the lightcurve is already far below even the 10^6 s sensitivity limit. It does however have an effect, albeit a small one, on the F115W and F090W filters.

At low redshifts the duration of the lightcurve presented in Kasen et al. (2011) is not quite long enough for the observed flux to reach the sensitivity limit; we extend it to the limit by extrapolating assuming a power-law scaling. The visible time Δt_{vis} is then simply given by the time the lightcurve is above the filter sensitivity limit. Shown in Figure 2.5 are the visibility times as a function of redshift for each of the NIRcam filters.

2.3.3 The Observable Number

With this estimate for Δt_{vis} , we may finally calculate the observable number of PISNe on the sky, given by the product of the PISN rate at z , as seen in the observer frame, and the time a PISN at z is visible, Δt_{vis} . This yields an estimate for the number of PISNe visible on the sky at any given time per unit redshift per unit solid angle:

$$\frac{dN}{dz d\Omega} \simeq \frac{dN}{dt_{obs} dz d\Omega} \Delta t_{vis}. \quad (2.17)$$

Figure 2.6 shows the number of PISNe per JWST field of view (FoV) above redshift z in a 10^6 s exposure for all three feedback cases for models R250 and B200. Models He100 and R175 can be found in the appendix. For the R250 model the results for a 10^4 s exposure are also included; B200 is not visible at high redshifts in a 10^4 s exposure.

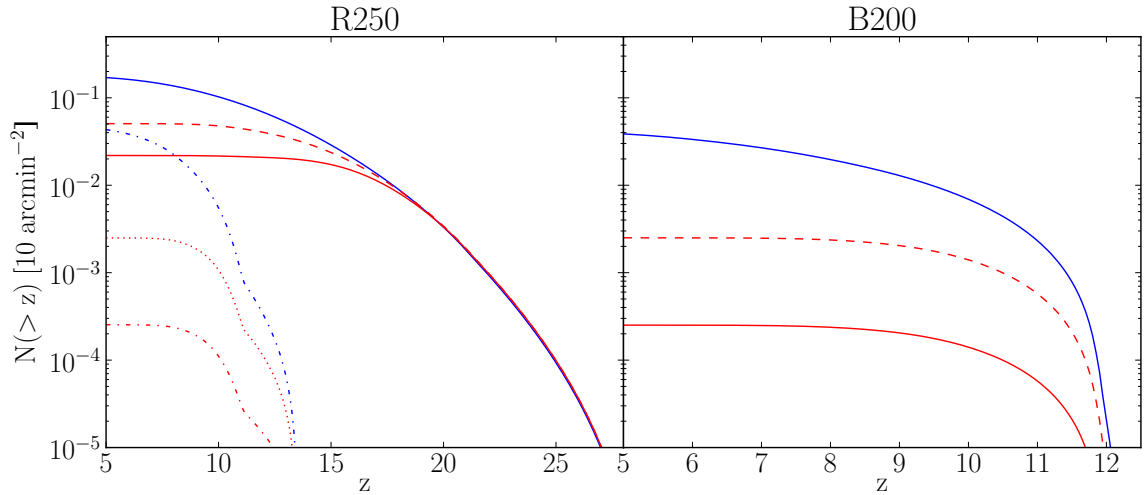


Figure 2.6: Upper and lower limits for the number of PISNe per JWST FoV above redshift z with different feedback prescriptions. The observable numbers for a 10^6 s exposure assuming the R250 model are shown on the left; the B200 model is employed on the right. Solid blue lines show an upper limit to the observable number in the case of no feedback, solid red lines an estimate for the observable number in our conservative feedback scenario, and dashed red lines the number in the enhanced star formation case. Note that the x-axis is scaled independently in each panel. Also shown in the R250 panel are the observable numbers for a 10^4 s exposure for the no-feedback (dot-dashed blue), conservative feedback (dot-dashed red), and enhanced star formation (dotted red) scenarios. The B200 model is not visible above $z = 5$ in a 10^4 s exposure.

In the optimistic case of an R250-type PISN with no feedback we expect ~ 0.2 PISNe per JWST FoV for a 10^6 s exposure. In the most pessimistic case of a B200-type PISN with strong negative feedback this number drops to $\sim 2.5 \times 10^{-4}$ per FoV. The actual number detected by the JWST will most likely lie somewhere within this range. Given this, we conclude that a single deep pencil-beam survey is unadvisable for detecting PISNe, as there aren't enough in a given field to ensure a detection, even in the most optimistic upper limit. This suggests that a mosaic search, covering a larger area with shorter exposure times, may be the best approach to ensure finding a Pop III PISN.

2.3.4 PISN Identification

The exceedingly long duration of their lightcurves poses a serious challenge for identifying PISNe. When combined with the cosmological time dilation factors involved, PISN lightcurves can last for decades; the highest redshift events will last longer than the projected mission lifetime for the JWST, making the detection of PISNe by searching for transients difficult at best. However, a multi-year campaign might be able to detect photometric variations; for example, the He100 model would appear to decline in brightness by ~ 0.3 magnitudes per year at redshift $z = 10$ (Kasen et al., 2011). Additionally, PISN colors become redder over time as the photosphere recedes into the ejecta and metal line blanketing suppresses flux in the bluer bands. While likely insufficient to unambiguously identify PISNe, this could be useful in selecting candidates for spectroscopic follow-up.

While the peak bolometric luminosities and spectra of PISNe resemble those of typical Type Ia and Type II supernovae (Joggerst & Whalen, 2011; Kasen et al., 2011), relatively little mixing occurs during the explosion (Joggerst & Whalen, 2011; Chen et al., 2011). As a result, PISNe mostly retain their onion-layer structure during the explosion, and metal lines do not appear in the spectrum until late times when the photosphere has receded deep into the ejecta. Some lighter elements may appear, but the early spectrum of a PISN will be devoid of Si, Ni and Fe lines (Joggerst & Whalen, 2011). This may provide the spectroscopic signature needed to identify PISNe.

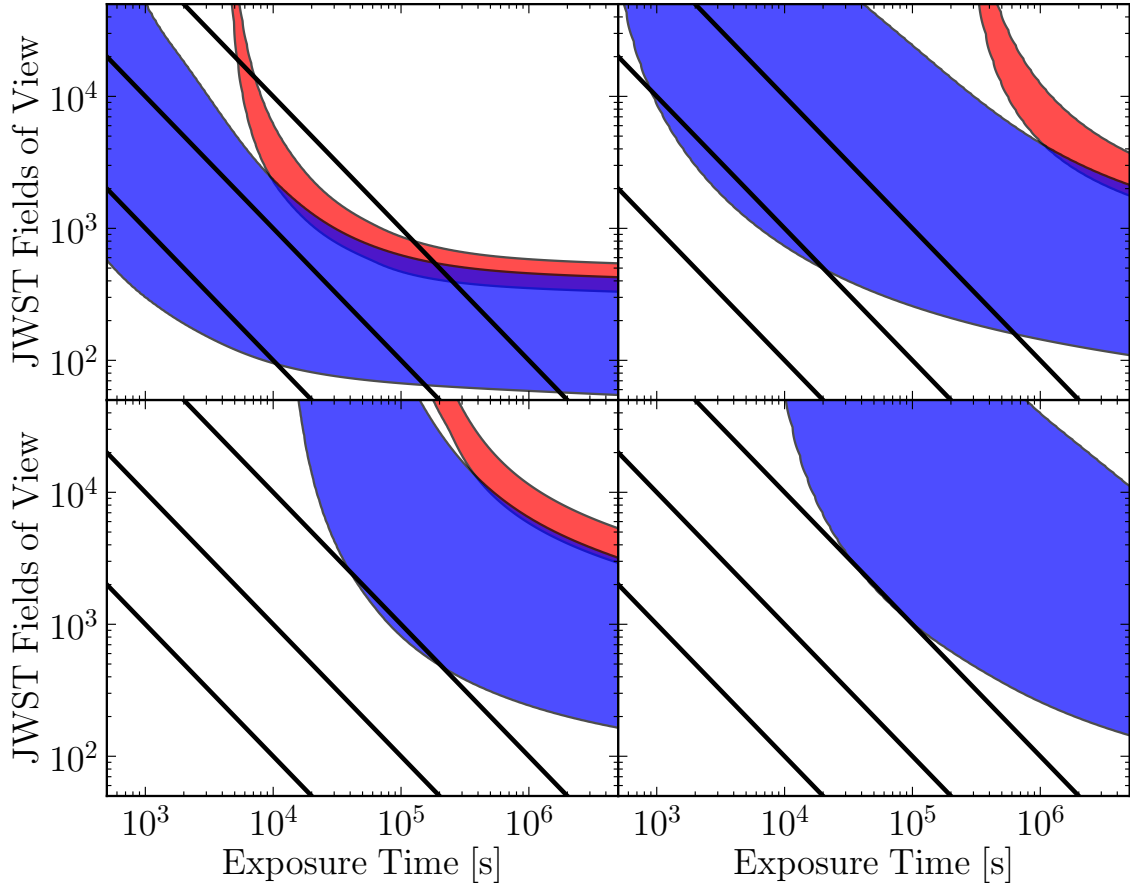


Figure 2.7: The observability of the R250, He100, B200, and R175 models (clockwise from upper left) from Kasen et al. (2011) using the JWST’s NIRcam F444W filter. Shown is the possible range for the number of JWST FoVs required to detect 10 sources as a function of exposure time. The blue range is for all PISNe, and the red for PISNe from $z > 15$. The lower boundaries correspond to the no-feedback upper limit to the PISN rate and the upper boundaries to the conservative feedback rate. From left to right, the black lines represent the number of pointings possible in a total of 10^6 , 10^7 , and 10^8 s for a given exposure time.

2.4 Discussion and Conclusions

In this work, we have examined the source density of PISNe from Pop III stars and considered their detectability with the JWST. We conclude that the limiting factor in detecting PISNe will be the scarcity of sources rather than their faintness, in agreement with the conclusions of Weinmann & Lilly (2005). The brightest PISNe should be readily detectable with the longest wavelength NIRcam filters out to $z \sim 25$; the problem is the overall scarcity of sources.

We have derived an estimate for the observable PISN rate, finding an upper limit of just over 0.01 PISNe per year per JWST FoV in the case of negligible chemical and radiative feedback. We also find that the inclusion of feedback can reduce the PISN rate by an order of magnitude, to ~ 0.001 per FoV. Accounting for the possibility of enhanced massive star formation in halos affected by LW radiation improves this rate slightly, to ~ 0.003 per FoV. The derived PISN rate then allows us to place an upper limit on the observable number of PISNe in a 10^6 s exposure of ~ 0.2 PISNe per JWST FoV in the no-feedback case. The most pessimistic case of a B200-type PISN with strong negative feedback reduces this number to $\sim 2.5 \times 10^{-4}$ per FoV, or one PISN per 4000 JWST fields of view.

The long duration of PISN lightcurves imply that spectroscopic follow-up of PISNe will likely be of great importance. PISN lightcurves can last for decades when combined with the cosmological time dilation factors at high redshifts, making the detection of PISNe by looking for transients untenable. However, a multi-year campaign could identify candidates photometrically, and the lack of metal lines in the spectrum at early times could provide a spectroscopic signature for identification.

We find that the main obstacle to observing PISNe is the paucity of sources. Beyond a moderate exposure time of a few times 10^4 s, the observability of bright PISNe is not a strong function of exposure time and is instead controlled by the source density; this is evident from Figure 2.7, where we have shown the number of JWST FoVs required to detect 10 PISNe (blue) as a function of exposure time for each of our PISN models. The upper boundaries correspond to our conservative estimate for the PISN rate in the presence of feedback, and the lower boundaries to the estimated rate without feedback. We can see that the decrease in the required number of JWST pointings slows considerably beyond $\sim 10^5$ s, hence a deep pencil-beam survey would not be advisable in searching for PISNe. Even for only high-redshift sources ($z > 15$; red) the dependence on exposure time is still minimal, being controlled by the lack of sources once the required imaging depth is reached.

Of particular interest in Figure 2.7 are the black lines representing the total number of pointings possible in 10^6 , 10^7 , and 10^8 s for a given exposure time and their location relative to the observability ranges in blue and red. 10^6 s is approximately the limit of what would be possible with a dedicated deep-field campaign; 10^7 s is the limit of the observations the JWST could make in a year assuming NIRCam is in use one third of the time; 10^8 s (~ 10 years) is the projected mission lifetime.

While the detection of a PISN from a ‘first’ star at very high redshifts would be exciting and is in fact possible given the detection limits of the JWST, the scarcity of sources at these redshifts means that such a detection would be highly contingent on serendipity. Even in the most optimistic case, with all available minihalos producing an R250-type PISN, the observability range for such events lies well above what is possible even in a full year of observations, though a few may be detected over the

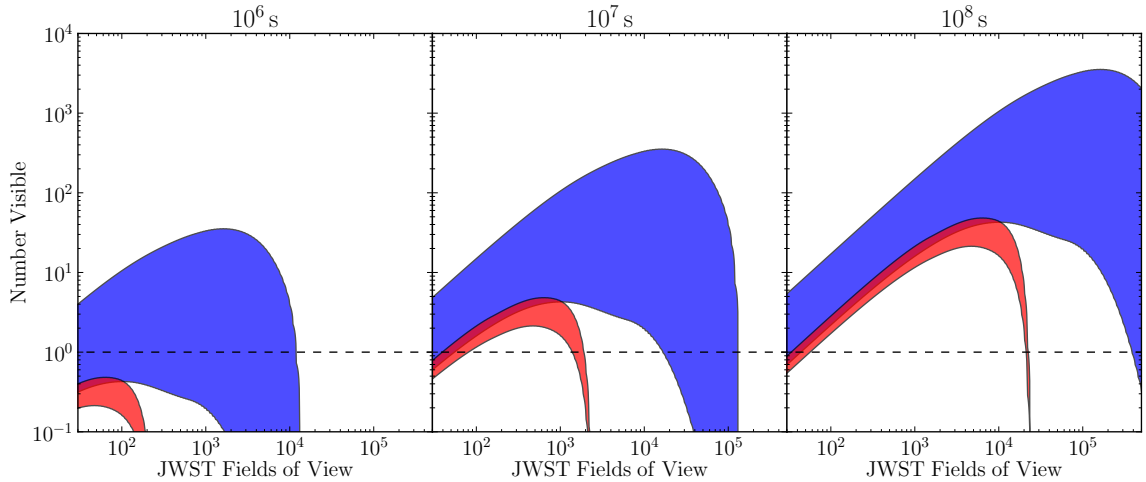


Figure 2.8: The total number of PISNe observable with a campaign of 10^6 , 10^7 and 10^8 s (from left to right) as a function of survey area for the R250 PISN model. In each case, the total campaign time is apportioned equally over the total survey area to determine the exposure time for individual pointings. The blue region represents all PISNe, the red only PISNe from $z > 15$. Upper boundaries correspond to the no-feedback upper limit to the PISN rate and lower boundaries to the conservative feedback case. For reference we mark the case of only one PISN visible (dashed line).

lifetime of the telescope. The detection of a PISN at lower redshifts appears to be more realistic. As the faintest PISNe (R175 and B200) are effectively unobservable, PISN searches should focus on looking for PISNe similar to the R250 and He100 models. In this case, the strategy with the highest likelihood of detection will be a mosaic survey of many moderately deep exposures. This is clear from Figure 2.8, where we show the number of PISNe that will be observable with the JWST in observing campaigns totalling 10^6 , 10^7 and 10^8 s for the R250 PISN model. The exposure time for each pointing varies with the total area covered by the survey in order to keep the total observing time constant. Upper boundaries correspond to the number visible in the no-feedback case, lower boundaries to the conservative feedback case. As in Figure 2.7, the blue region shows the observable number from all redshifts,

the red region only those from $z > 15$. We see that the observable number increases until the resulting exposure time is no longer sufficient to detect PISNe. The optimal search strategy then will be to cover as large an area as possible, going only as deep as necessary, possibly in a similar manner to the ongoing Brightest of Reionizing Galaxies survey with the *Hubble Space Telescope* (Trenti et al., 2011; Bradley et al., 2012).

Chapter Three: Population III Star Formation

Under X-ray Feedback

3.1 Introduction

The formation of the first stars in the Universe marked a watershed moment in cosmic history. It was during this as-yet unobserved epoch that our Universe began its transformation from the relatively simple initial conditions of the Big Bang to the complex tapestry of dark matter (DM), galaxies, stars and planets that we see today (Barkana & Loeb, 2001; Miralda-Escudé, 2003; Bromm et al., 2009; Loeb, 2010).

The radiation from these so-called Population III (Pop III) stars swept through the Universe, beginning the process of reionisation (Kitayama et al., 2004; Sokasian et al., 2004; Whalen et al., 2004; Alvarez et al., 2006; Johnson et al., 2007; Robertson et al., 2010), while the heavy elements forged in their cores and released in the violent supernova explosions marking their deaths began the process of chemical enrichment (Madau et al. 2001; Mori et al. 2002; Bromm et al. 2003; Heger et al. 2003; Umeda & Nomoto 2003; Tornatore et al. 2007; Greif et al. 2007, 2010; Wise & Abel 2008; Maio et al. 2011; recently reviewed in Karlsson et al. 2013). These effects are strongly dependent on the characteristic mass of Pop III stars, which determines their total luminosity and ionising radiation output (Schaerer, 2002), and the details of their eventual demise (Heger et al., 2003; Heger & Woosley, 2010; Maeder & Meynet, 2012). As a result, developing a thorough knowledge of how environmental effects influence the properties of these stars is crucial to understanding their impact on the

intergalactic medium (IGM) and subsequent stellar generations.

While the complexities of the various physical processes involved have so far prevented a definitive answer to this question, the basic properties of the first stars have been fairly well established, with the consensus that they formed in dark matter ‘minihaloes,’ having on the order of $10^5 - 10^6 M_\odot$ at $z \gtrsim 20$ (Couchman & Rees, 1986; Haiman et al., 1996; Tegmark et al., 1997). Pioneering numerical studies of the collapse of metal-free gas into these haloes, where molecular hydrogen was the only available coolant, suggested that Pop III stars were very massive—on the order of $100 M_\odot$ —due to the lack of coolants more efficient than H_2 (e.g., Bromm et al., 1999, 2002; Abel et al., 2002; Yoshida et al., 2003; Bromm & Larson, 2004; Yoshida et al., 2006; O’Shea & Norman, 2007). More recent simulations, benefiting from increased resolution, have found that significant fragmentation of the protostellar disc occurs during the star formation process, with the protostellar cores ranging in mass from ~ 0.1 to tens of solar masses (Stacy et al., 2010; Clark et al., 2011a,b; Greif et al., 2011a, 2012; Stacy & Bromm, 2013; Susa et al., 2014; Hirano et al., 2014, 2015), with a presumably flat initial mass function (IMF; Dopcke et al. 2013).

One intriguing outcome of these studies is that while the protostellar disc does indeed fragment, it only marginally satisfies the Gammie (2001) criterion for disc instability (Clark et al., 2011b; Greif et al., 2011a, 2012). While protostellar feedback is insufficient to stabilise the disc (Smith et al., 2011; Stacy et al., 2012a), it is possible that an external heating source could serve to stabilise the disc and prevent fragmentation. One promising source of such an external background is far-ultraviolet radiation in the Lyman-Werner (LW) bands (11.2-13.6 eV). While lacking sufficient energy to interact with atomic hydrogen, LW photons efficiently dissociate H_2

molecules, which serve as the primary coolant in primordial gas. This diminishes the ability of the gas to cool, but studies have found that the critical LW flux required to suppress H₂ cooling is far above the expected mean value of such radiation (Dijkstra et al., 2008). Another possible heating source was recently explored by Smith et al. (2012; see also Ripamonti et al. 2008, 2010) who investigated the ability of DM annihilation to suppress fragmentation of the protostellar disc. While such heating is unable to suppress star formation, it does serve to stabilise the disc, suppressing fragmentation within 1000 AU of the central protostar, at least for a while (Stacy et al., 2012b, 2014).

While LW radiation alone is unable to reliably suppress H₂ cooling in minihaloes, significant sources of LW photons, i.e., active star forming regions, contain large numbers of massive stars, and possibly mini-quasars as well (Kuhlen & Madau, 2005; Jeon et al., 2012, 2014). Not only do massive stars end their lives as supernovae, leaving behind remnants that are significant sources of X-rays, a significant fraction of these stars are likely to be in tight binaries (e.g., Clark et al., 2011b; Greif et al., 2012; Mirocha, 2014) and produce high-mass X-ray binaries (HMXBs). As the cross-section of neutral hydrogen for X-rays is relatively small, such photons easily escape their host haloes, building up a cosmic X-ray background (CXB; Oh 2001; Haiman et al. 2000; Venkatesan et al. 2001; Glover & Brand 2003; Cen 2003; Kuhlen & Madau 2005; Jeon et al. 2012, 2014). This CXB serves to both heat and increase the ionisation fraction of gas in neighbouring minihaloes, which in turn can serve to increase the H₂ fraction of the gas by increasing the number of free electrons available to act as catalysts.

In this paper we consider the effects of such an X-ray background on Pop III star

formation. In Section 3.2 we provide the cosmological context for this study, estimating both the expected intensity of the CXB, and the amount of additional heating required to prevent minihalo collapse. Our numerical methodology is described in Section 3.3, while our results are found in Section 3.4. Finally, our conclusions are gathered in Section 4.5. Throughout this paper we adopt a Λ CDM model of hierarchical structure formation, using the following cosmological parameters: $\Omega_\Lambda = 0.7$, $\Omega_m = 0.3$, $\Omega_B = 0.04$, and $H_0 = 70 \text{ km s}^{-1} \text{ Mpc}^{-1}$.

3.2 Cosmological Context

3.2.1 Early Cosmic X-ray Background

The predominant source of X-rays at high redshifts was likely HMXBs. Supermassive black holes were not yet common during this era, and while supernovae produce significant X-ray radiation, their transient nature precludes them from efficiently building up an X-ray background. We can calculate the energy density u_{XR} of X-rays produced by HMXBs as follows:

$$u_{\text{XR}}(z) = f_{\text{HMXB}} \Psi_*(z) \left(\frac{L_{\text{XR}}}{M_{\text{HMXB}}} \Delta t_{\text{HMXB}} \right) t_{\text{H}}(z) (1+z)^3, \quad (3.1)$$

where f_{HMXB} is the mass fraction of stars that form HMXBs, $\Psi_*(z)$ is the comoving star formation rate density (SFRD) as a function of redshift, and L_{XR} , M_{HMXB} and Δt_{HMXB} are the X-ray luminosity, mass and lifespan of a typical HMXB, respectively. The X-ray background accumulates over the Hubble time t_{H} , and the factor of $(1+z)^3$ accounts for the conversion from a comoving SFRD to a physical energy density.

We employ the SFRD calculated by Greif & Bromm (2006), but see Campisi et al. (2011) for a more recent calculation in the context of Pop III gamma-ray burst obser-

vations. The Greif & Bromm (2006) SFRD incorporates both Pop III and Population I/II star formation with self-consistent reionisation and chemical enrichment. Their SFRD history only extends out to $z = 30$; we extrapolate back to $z = 100$ using a simple log-linear fit.

The mass fraction of stars forming HMXBs, f_{HMXB} , is determined by the mass fraction of stars forming black holes f_{BH} , the fraction of black holes in binary systems f_{binary} and the fraction of binaries close enough for mass transfer to occur f_{close} . As their IMF is nearly flat with a characteristic mass of a few $\times 10 M_{\odot}$ (Bromm, 2013), we make the plausible assumption that half of all Pop III stars end up forming black holes. Recent work by Stacy & Bromm (2013) found that just over half of Pop III stars end up in binary pairs; we set f_{binary} accordingly. While the orbital distribution of nearby solar-type stars is well-studied (e.g., Duquennoy & Mayor, 1991), that of Pop III stars is still very uncertain (but see Stacy & Bromm, 2013). We therefore assume that the orbital distribution of Pop III stars is flat, i.e., $dN/d\log a$ is constant, with a minimum orbital radius of $a = 10 R_{\odot}$ and a maximum of 6.5 pc, which is approximately the size of the self-gravitating baryonic core of a minihalo. For mass transfer onto the BH to occur, the companion star must at some point exceed its Roche limit; hence we designate all binaries with orbital distances less than $100 R_{\odot}$ as ‘close.’ Doing so, we find that approximately 2/15 of Pop III binaries will be close enough for mass transfer to occur. Thus, for Pop III stars, we can estimate f_{HMXB} as follows:

$$f_{\text{HMXB}} = f_{\text{BH}} f_{\text{binary}} f_{\text{close}} \simeq \left(\frac{1}{2}\right) \left(\frac{1}{2}\right) \left(\frac{2}{15}\right) = \frac{1}{30}. \quad (3.2)$$

Assuming HMXBs accrete material at close to the Eddington limit, we can ap-

proximate

$$\frac{L_{\text{HMXB}}}{M_{\text{HMXB}}} \simeq l_{\text{EDD}} = 10^{38} \text{ erg s}^{-1} M_{\odot}^{-1}, \quad (3.3)$$

where L_{HMXB} is the bolometric luminosity. Following Jeon et al. (2014), we assume that the spectral distribution of the emerging radiation takes the form of a thermal multi-colour disc at frequencies below 0.2 keV, and that of a non-thermal power law at higher frequencies (e.g., Mitsuda et al., 1984). Assuming the entire accretion luminosity is emitted between 13.6 eV and 10 keV, the fraction of the total luminosity emitted between 1 and 10 keV is approximately 30%. We choose 1 keV for the lower limit as the cross section of neutral hydrogen increases rapidly at lower frequencies. X-rays below ~ 1 keV thus cannot efficiently contribute to a pervasive background. We therefore approximately set

$$L_{\text{XR}} \simeq \frac{3}{10} L_{\text{HMXB}}. \quad (3.4)$$

Assuming the typical lifespan of an HMXB is 10^7 yr (e.g., Belczynski et al., 2012; Jeon et al., 2012), the average intensity of this radiation $J_{\text{XR}}(z)$ is then given by

$$J_{\text{XR}}(z) = \int_{\nu_{\min}}^{\nu_{\max}} J_{\nu, \text{XR}}(z) d\nu = \frac{c}{4\pi} u_{\text{XR}}(z), \quad (3.5)$$

where $h\nu_{\min} = 1$ keV and $h\nu_{\max} = 10$ keV. Following Inayoshi & Omukai (2011), we employ

$$J_{\nu, \text{XR}}(z) = J_{\nu, 0}(z) \left(\frac{\nu}{\nu_0} \right)^{-1.5} \quad (3.6)$$

where $J_{\nu, 0}(z)$ is the specific X-ray intensity, $h\nu_0 = 1$ keV, and $J_{\nu, 0}(z)$ is the normalisation factor. In addition to this fiducial estimate for $J_{\text{XR}}(z)$, henceforth referred to as model J_0 , we consider three additional models with ten, one hundred and one thousand times the intensity of J_0 , as shown in Figure 3.1.

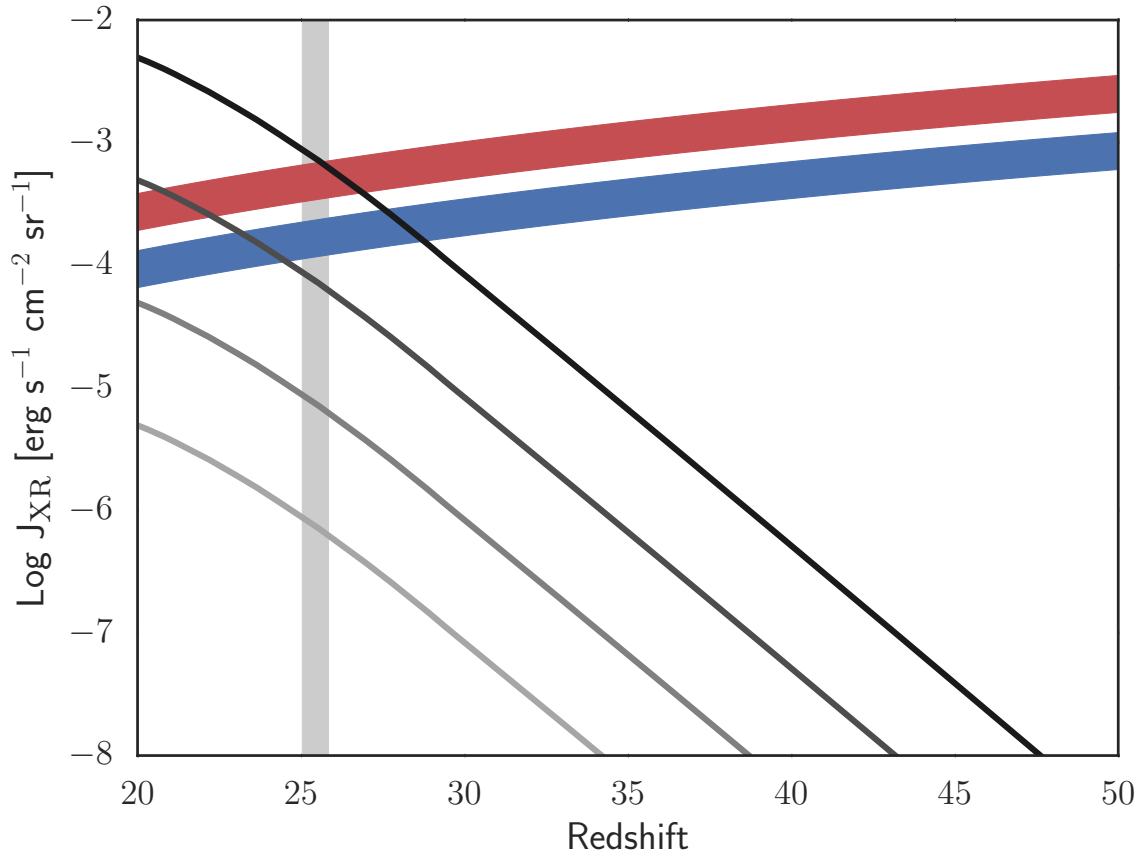


Figure 3.1: X-ray average intensity as a function of redshift. The lightest grey line represents our fiducial model J_0 , with successively darker grey lines denoting $10, 100$, and $1000 J_0$, respectively. The blue and red ranges denote the critical intensity above which collapse of the baryonic component into a $2 \times 10^5 M_\odot$ and $10^6 M_\odot$ halo is suppressed, respectively. In each case, the upper limit of the range assumes the contribution from secondary ionisation is negligible, while the lower limit denotes $J_{\text{XR,crit}}$ for maximally effective secondary ionisation. The vertical grey bar denotes the range of redshifts over which our minihaloes first reach $n = 10^{12} \text{ cm}^{-3}$.

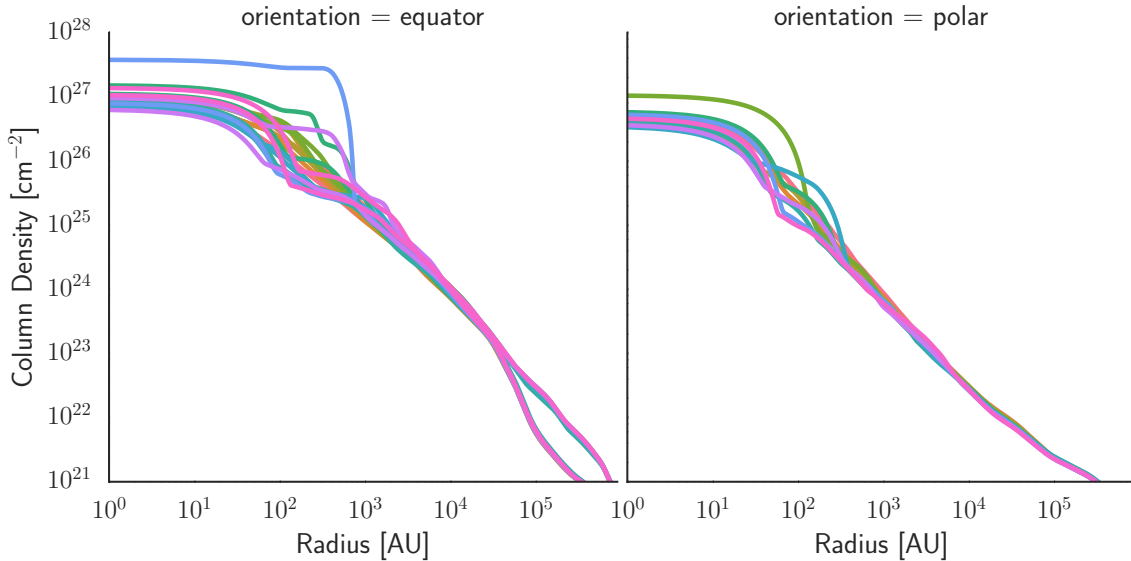


Figure 3.2: Cumulative column density along both polar and equatorial lines of sight approaching the centre of the minihalo. Shown is the column density for a selection of snapshots from just prior to the formation of the first sink particle to 5000 yr later, with different colors indicating different snapshots. Note that the scatter in the central 10^3 AU is larger in the equatorial plane than along the pole: as the accretion disc rotates, occasionally a sink particle orbiting the density-averaged centre lands within the chosen line of sight.

3.2.2 Jeans Mass Filtering under X-ray Feedback

The presence of an ionising X-ray background will necessarily heat the gas in the IGM. As a result, collapse into a minihalo will be suppressed when the thermal energy of the gas exceeds the baryonic gravitational potential energy of the minihalo in question. The baryonic gravitational potential energy of a minihalo prior to collapse is given by

$$|E_{\text{grav}}| \simeq \frac{\Omega_B}{\Omega_m} \frac{GM_{\text{vir}}^2}{R_{\text{vir}}}, \quad (3.7)$$

where G is the gravitational constant, M_{vir} is the virial mass, and R_{vir} is the virial radius of the minihalo. The gas in the minihalo will naturally undergo adiabatic heating as it is compressed, but the cooling provided by the formation of molecular

hydrogen keeps this process from halting collapse. An additional heating mechanism, provided here by X-rays, is required to prevent dissipational collapse of the gas. We approximate this excess thermal energy E_{th} as

$$E_{\text{th}} \simeq \Gamma_{\text{XR}} t_{\text{ff}} R_{\text{vir}}^3, \quad (3.8)$$

where Γ_{XR} is the X-ray heating rate per unit volume and t_{ff} is the freefall time on which gravity draws gas into the minihalo, given by

$$t_{\text{ff}} = \sqrt{\frac{3\pi}{32G\rho_b}}, \quad (3.9)$$

where ρ_b is the background density. To first order then, the critical heating rate $\Gamma_{\text{XR,crit}}$ for suppressing collapse is given by

$$\Gamma_{\text{XR,crit}} = \frac{\Omega_B}{\Omega_m} \frac{GM_{\text{vir}}^2}{t_{\text{ff}} R_{\text{vir}}^4}. \quad (3.10)$$

Utilising the fact that

$$M_{\text{vir}} \simeq \frac{4\pi}{3} R_{\text{vir}}^3 (200\rho_b) \quad (3.11)$$

and

$$\rho_b = \rho_0(1+z)^3, \quad (3.12)$$

where $\rho_0 = 2.5 \times 10^{-30} \text{ g cm}^{-3}$ is the average matter density at the present epoch, we can solve for $\Gamma_{\text{XR,crit}}$ as a function of halo mass and redshift:

$$\begin{aligned} \Gamma_{\text{XR,crit}}(M, z) &= 1.3 \times 10^{-28} \text{ erg s}^{-1} \text{ cm}^{-3} \\ &\times \left(\frac{M}{10^6 M_\odot}\right)^{\frac{2}{3}} \left(\frac{1+z}{20}\right)^{\frac{11}{2}}, \end{aligned} \quad (3.13)$$

where we have normalised to typical minihalo values.

Prior to minihalo virialisation, gas densities are relatively low, such that attenuation of the CXB as it penetrates the minihalo is negligible (see Figure 3.4). Given

this, Γ_{XR} is related to the intensity of the CXB as follows:

$$\Gamma_{\text{XR}} = 4\pi n \int_{\nu_{\min}}^{\nu_{\max}} J_{\nu, \text{XR}}(z) \sigma_{\nu} \left(1 - \frac{\nu_{\text{ion}}}{\nu}\right) d\nu + \Gamma_{\text{XR,sec}}, \quad (3.14)$$

where n is the gas number density and $\Gamma_{\text{XR,sec}}$ is the contribution to the heating rate from secondary ionisation. While the contribution of secondary ionisation events to the heating rate has a complicated dependence on the ionisation fraction (Shull & van Steenberg, 1985, see Section 3.3.4 for details), $\Gamma_{\text{XR,sec}}$ never enhances Γ_{XR} by more than a factor of two in the regime considered here. When secondary ionisation heating is negligible, we can similarly estimate the critical X-ray background required to suppress collapse:

$$J_{\text{XR,crit}}(M, z) = 3.4 \times 10^{-4} \text{ erg s}^{-1} \text{ cm}^{-2} \text{ sr}^{-1} \times \left(\frac{M}{10^6 M_{\odot}}\right)^{\frac{2}{3}} \left(\frac{1+z}{20}\right)^{\frac{5}{2}}. \quad (3.15)$$

When secondary ionisation heating is maximally effective then, $J_{\text{XR,crit}}$ will be a factor of two lower. Both limits for $J_{\text{XR,crit}}$ are shown in Figure 3.1 for both a 10^6 and a $2 \times 10^5 M_{\odot}$ minihalo. These can be interpreted as the approximate range in which the CXB will begin to have a significant impact on the collapse of gas into such a minihalo.

3.3 Numerical Methodology

3.3.1 Initial Setup

We use the well-tested N -body smoothed particle hydrodynamics (SPH) code GADGET-2 (Springel, 2005). We initialised our simulations in a periodic box of length 140 kpc (comoving) at $z = 100$ in accordance with a Λ CDM model of hierarchical

structure formation. An artificially enhanced normalisation of the power spectrum, $\sigma_8 = 1.4$, was used to accelerate structure formation. See Stacy et al. (2010) for a discussion of the validity of this choice. High resolution in this simulation was achieved using a standard hierarchical zoom-in technique for both DM and SPH particles. Three nested levels of additional refinement at 40, 30 and 20 kpc (comoving) were added, each centred on the point where the first minihalo forms in the simulation. As resolution increases, each ‘parent’ particle is replaced by eight ‘child’ particles, such that at the greatest refinement level, each original particle has been replaced by 512 high-resolution particles. These highest-resolution SPH particles have a mass $m_{\text{SPH}} = 0.015 M_\odot$, such that the mass resolution of the simulation is $M_{\text{res}} \simeq 1.5 N_{\text{neigh}} m_{\text{SPH}} \lesssim 1 M_\odot$, where $N_{\text{neigh}} \simeq 32$ is the number of particles used in the SPH smoothing kernel (Bate & Burkert, 1997).

3.3.2 Thermodynamics and Chemistry

Our chemistry and cooling network is the same as that described in Greif et al. (2009). We follow the abundances of H, H^+ , H^- , H_2 , H_2^+ , He, He^+ , He^{++} , D, D^+ , HD and e^- . All relevant cooling mechanisms, including cooling via H and He collisional excitation and ionisation, recombination, bremsstrahlung and inverse Compton scattering are accounted for. Of particular importance is cooling via the ro-vibrational modes of H_2 , which are excited by collisions with H and He atoms and other H_2 molecules. At high densities, additional H_2 processes must also be included in order to properly model the gas evolution. For example, three-body H_2 formation and the associated heating becomes important above $n \gtrsim 10^8 \text{ cm}^{-3}$ (Turk et al., 2011). The formation rates for these reactions are uncertain; we employ the intermediate rate from Palla et al. (1983). At densities greater than $\sim 10^9 \text{ cm}^{-3}$, the ro-vibrational lines for H_2 become

optically thick, decreasing the efficiency of such cooling. We employ the Sobolev approximation and an escape probability formalism to account for this (see Yoshida et al. 2006; Greif et al. 2011a for details).

3.3.3 Optical Depth Estimation

Over the length scale of our cosmological box, the X-ray optical depth of primordial gas is $\ll 1$ everywhere except approaching the centre of the star-forming minihalo. As the CXB radiation penetrates the minihalo, it will necessarily be attenuated due to the high column density N of the intervening gas. In order to estimate the optical depth, we directly calculate the column density approaching the centre of the accretion disc along both polar and equatorial lines of sight in the absence of a CXB. As shown in Figure 3.2, the column density remains essentially constant for the duration of the simulation, and has a simple power-law dependence on radius over several orders of magnitude up to the resolution limit of our simulation (~ 100 AU). This same power-law behaviour can be seen versus density as well, as shown in Figure 3.3. In addition we notice that for a given gas density, the column density along the pole is roughly a factor of 10 lower than along the equator. Performing an ordinary least squares fit to the combined data from several snapshots for $n > 10^4 \text{ cm}^{-3}$, we find that the column density along the pole and equator is well fit by

$$\log_{10}(N_{pole}) = 0.5323 \log_{10}(n) + 19.64 \quad (3.16)$$

and

$$\log_{10}(N_{eq}) = 0.6262 \log_{10}(n) + 19.57, \quad (3.17)$$

respectively, and does not change appreciably with increasing J_{XR} .

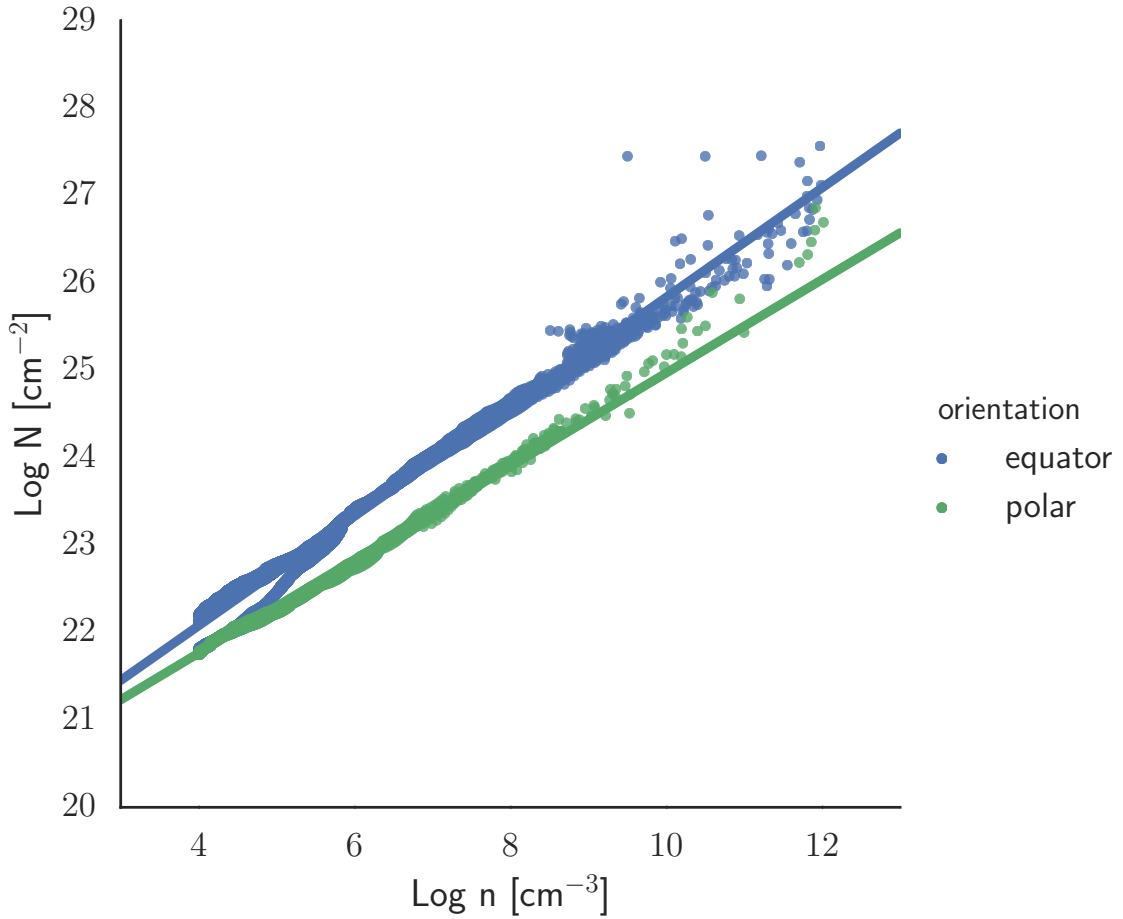


Figure 3.3: Column density as a function of gas number density along both polar (green) and equatorial (blue) lines of sight. Points sample the distribution of column density as a function of number density for their respective lines of sight across several snapshots, while the lines indicate the χ^2 best fit.

To account for this difference in column density, we assume every line of sight within 45 degrees of the pole (Hosokawa et al., 2011) experiences column density N_{pole} and every other line of sight experiences N_{eq} . Radiation within the opening angle is attenuated by $e^{-\sigma_\nu^i N_{pole}}$ while the remainder of the background is attenuated by $e^{-\sigma_\nu^i N_{eq}}$, allowing us to define an effective optical depth τ_{XR} such that

$$e^{-\tau_{XR}} = \frac{2\Omega_{pole}}{4\pi} e^{-\sigma_\nu^i N_{pole}} + \frac{4\pi - 2\Omega_{pole}}{4\pi} e^{-\sigma_\nu^i N_{eq}}, \quad (3.18)$$

(e.g., Clark & Glover, 2014). Here we use the standard expressions for the photoionisation cross sections σ_ν^i of hydrogen and helium (e.g., Barkana & Loeb, 2001; Osterbrock & Ferland, 2006) and define Ω_{pole} as

$$\Omega_{pole} = \int_0^{2\pi} d\phi \int_0^{\pi/4} \sin\theta d\theta = 1.84 \text{ sr}. \quad (3.19)$$

Accounting for this attenuation and incorporating the cosmic X-ray background described in Section 3.2.1, the resulting ionisation and heating rates for the $J_{XR} = J_0$ case at $z = 25$ as a function of total number density are shown in Figure 3.4.

3.3.4 X-ray Ionisation and Heating

To study the effects of X-ray ionisation and heating on primordial star formation, we implement a uniform CXB as discussed in Section 3.2.1. For further details, see Jeon et al. (2012, 2014). Accounting for attenuation of the incident X-ray radiation while penetrating the minihalo, the primary ionisation rate coefficient for chemical species i can be written as

$$k_{ion,p}^i = 4\pi \int_{\nu_{min}}^{\nu_{max}} \frac{J_\nu \sigma_\nu^i}{h\nu} e^{-\tau_{XR}} d\nu \quad (3.20)$$

where $\nu_{min} = 1 \text{ keV}/h$ and $\nu_{max} = 10 \text{ keV}/h$.

We include the effects of secondary ionisation from energetic electrons released by the absorption of X-ray photons by adopting the fitting formulae of Shull & van

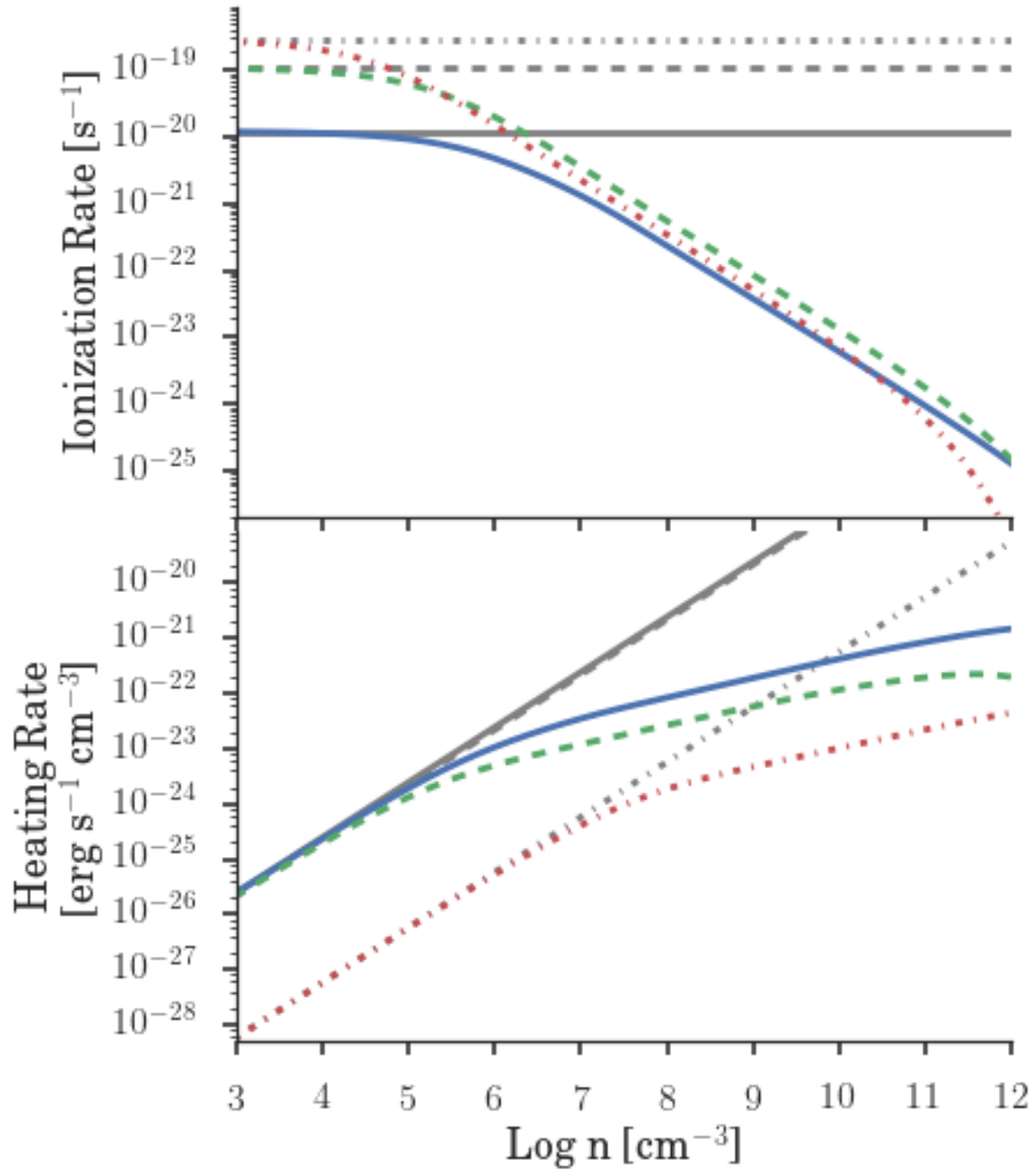


Figure 3.4: X-ray ionisation and heating rates for H I , He I and He II as a function of total number density for the $J_{\text{XR}} = J_0$ case at $z = 25$. In both panels, the solid blue, dashed green, and dash-dotted red lines denote H I , He I , and He II , respectively. The grey lines in each style demonstrate the expected rates in the absence of X-ray self-shielding for that species. H I dominates both ionisation and heating when the relative abundances of these species are accounted for, and we see that X-rays penetrating the minihalo experience significant attenuation above densities of $n \sim 10^6 \text{ cm}^{-3}$.

Steenberg (1985; see also Valdés & Ferrara 2008; Furlanetto & Stoever 2010), who calculated the fractions of the initial electron energy going into heating the surrounding gas, as well as into secondary ionisations of H I and He I (f_{H} and f_{He} , respectively). While such secondary ionisation events have a significant impact on the ionisation fraction of H I and He I, secondary ionisations of He II are negligible (Shull & van Steenberg, 1985), and are not included here. The effective ionisation rates are thus given by

$$k_{\text{ion}}^i = k_{\text{ion},p}^i + k_{\text{ion},\text{sec}}^i \quad (3.21)$$

where

$$k_{\text{ion},\text{sec}}^{\text{H I}} = f_{\text{H}} \left(\Gamma_{\text{H I}} + \frac{n_{\text{He I}}}{n_{\text{H I}}} \Gamma_{\text{He I}} \right) \frac{1}{13.6 \text{ eV}} \quad (3.22)$$

and

$$k_{\text{ion},\text{sec}}^{\text{He I}} = f_{\text{He}} \left(\Gamma_{\text{He I}} + \frac{n_{\text{H I}}}{n_{\text{He I}}} \Gamma_{\text{H I}} \right) \frac{1}{24.6 \text{ eV}}. \quad (3.23)$$

Here Γ_i is the heating rate at which excess energy from the initial X-ray photoionisation is released into the gas, given by

$$\Gamma_i = 4\pi n_i \int_{\nu_{\text{min}}}^{\nu_{\text{max}}} J_{\nu} \sigma_{\nu}^i \left(1 - \frac{\nu_{\text{ion}}^i}{\nu} \right) e^{-\tau_{\text{XR}}} d\nu, \quad (3.24)$$

where ν_{ion}^i is the ionisation threshold of the species in question; $h\nu_{\text{ion}} = 13.6 \text{ eV}$, 24.6 eV and 54.4 eV for hydrogen, neutral helium and singly ionised helium, respectively.

The fraction of the initial electron energy going into secondary ionisations depends on the hydrogen ionisation fraction $x_{\text{ion},H}$ as follows:

$$f_{\text{H}} = 0.3908 (1 - x_{\text{ion},H}^{0.4092})^{1.7592} \quad (3.25)$$

$$f_{\text{He}} = 0.0554 (1 - x_{\text{ion},H}^{0.4614})^{1.6660}. \quad (3.26)$$

Thus the total heating rate Γ_i^{tot} , including contributions from both primary and secondary ionizations, can be written as

$$\Gamma_i^{tot} = 4\pi n_i (1 - f_i) \int_{\nu_{min}}^{\nu_{max}} J_\nu \sigma_\nu^i \left(1 - \frac{\nu_{ion}^i}{\nu}\right) e^{-\tau_{xr}} d\nu. \quad (3.27)$$

3.3.5 Sink Particles

We employ the sink particle method described in Stacy et al. (2010). When the density of a gas particle exceeds $n_{max} = 10^{12} \text{ cm}^{-3}$, we replace it and all non-rotationally-supported particles within the accretion radius r_{acc} with a single sink particle. We set r_{acc} equal to the resolution length of the simulation: $r_{acc} = L_{res} \simeq 50 \text{ AU}$. Here,

$$L_{res} \simeq 0.5 \left(\frac{M_{res}}{\rho_{max}} \right)^{1/3}, \quad (3.28)$$

where $\rho_{max} = n_{max} m_H$. The sink thus immediately accretes the majority of the particles within its smoothing kernel, such that its mass M_{sink} is initially close to $M_{res} \simeq 1 M_\odot$. Once the sink is formed, additional gas particles and smaller sinks are accreted as they approach within r_{acc} of that sink particle. After each accretion event, the position and momentum of the sink particle is set to the mass-weighted average of the sink and the accreted particle.

Following the creation of a sink particle, its density, temperature and chemical abundances are no longer updated. The sink's density is held constant at 10^{12} cm^{-3} , and its temperature is kept at 650 K, typical for collapsing gas reaching this density; the pressure of the sink is set correspondingly. Assigning a temperature and pressure to the sink particle in this fashion allows it to behave as an SPH particle. This avoids the creation of an artificial pressure vacuum, which would inflate the accretion rate onto the sink (see Bromm et al., 2002; Martel et al., 2006). The sink's position and

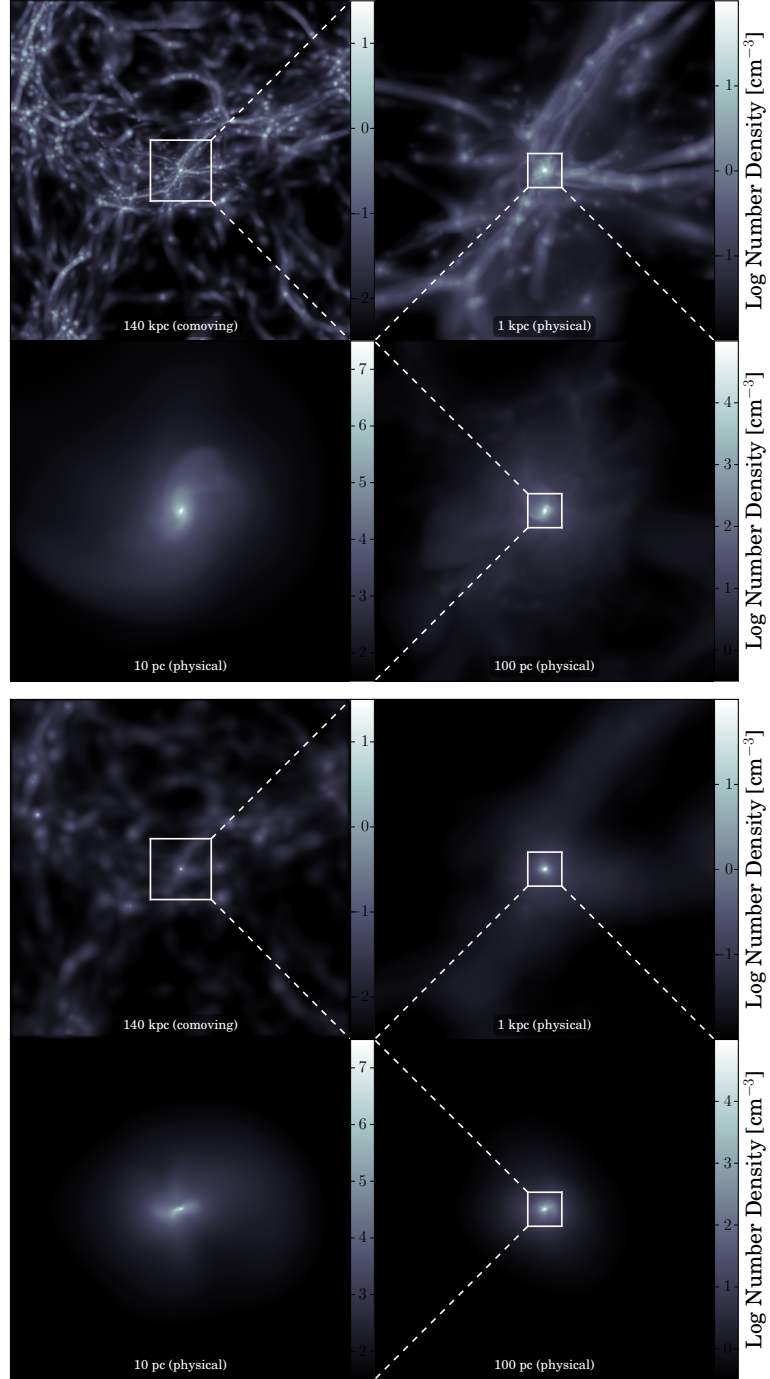


Figure 3.5: Density projection of the final simulation output 5000 yr after the formation of the first sink particle on progressively smaller scales for both the $J_{\text{XR}} = 0$ (top) and the shielded $J_{\text{XR}} = 10^2 J_0$ (bottom) simulations. White boxes indicate the region depicted on the next smaller scale. Clockwise from top left: full simulation box; minihalo and surrounding filamentary structure; central 100 pc of minihalo; central 10 pc. The density scale for each panel is included just to the right – note that the scaling changes from panel to panel. In both cases, note how the morphology approaches an increasingly smooth, spherical distribution on the smallest scales, where the gas is in quasi-hydrostatic equilibrium. In the shielded $J_{\text{XR}} = 10^2 J_0$ case, the low-density filamentary structure is smoothed out due to X-ray heating, whereas gas at high densities is shielded and proceeds to collapse unimpeded.

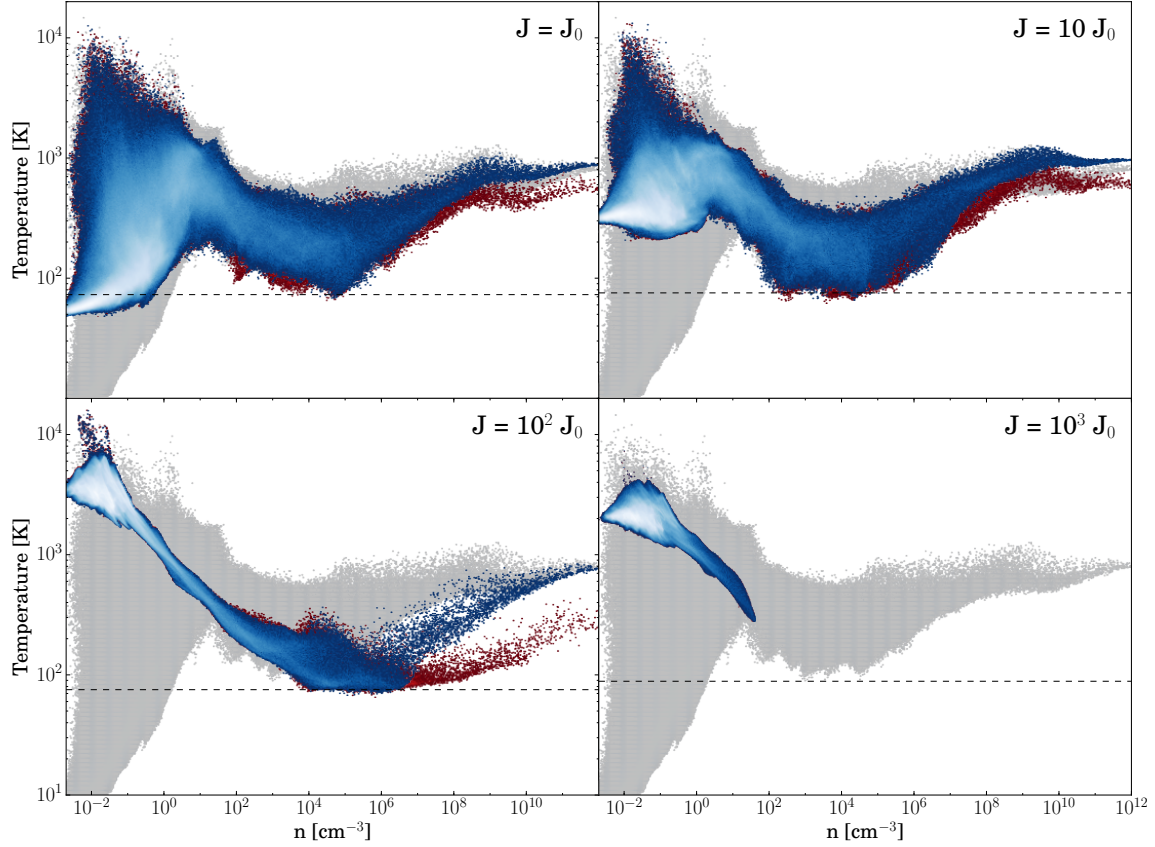


Figure 3.6: Mass-weighted temperature distribution of the collapsing gas in each simulation, shown just prior to sink formation—or maximum density reached in the case of the $10^3 J_0$ background. Each panel shows the behaviour of the gas in the presence of the CXB, both shielded (in blue) and unshielded (in red). For comparison, the gas behaviour in the $J_{\text{XR}} = 0$ case is shown in grey. Dashed lines denote the CMB temperature. All simulations except the $10^3 J_0$ case successfully collapse to high densities. Gas at low densities gets progressively hotter and gas in the loitering phase gets progressively cooler with increasing J_{XR} . Note that in all cases where the minihalo successfully proceeds to collapse, the shielded gas re-converges to the $J_{\text{XR}} = 0$ case prior to reaching sink formation densities.

momentum continue to evolve through gravitational and, initially, hydrodynamical interactions with the surrounding particles. As it gains mass and gravity becomes the dominant force, the sink behaves less like an SPH particle and more like a non-gaseous N -body particle.

3.4 Results

We perform a total of nine simulations, following each for 5000 years after the formation of the first sink particle in the simulation. Beyond our fiducial case of $J_{\text{XR}} = J_0$ and the standard case of $J_{\text{XR}} = 0$, we examine three additional simulations with $J_{\text{XR}} = 10$, 10^2 , and 10^3 times J_0 . The results of a $J_{\text{XR}} = 10^{-1} J_0$ simulation were indistinguishable from $J_{\text{XR}} = 0$. Not only is the CXB at high redshifts subject to fairly large uncertainties, but as Pop III star formation is highly biased there is likely a significant amount of cosmic variance. In addition, we also consider the optically-thin limit where $\tau_{\text{XR}} \rightarrow 0$. While physically unrealistic, these numerical experiments serve as comparison cases to more fully elucidate the physics in the properly shielded simulations.

3.4.1 Initial Collapse

3.4.1.1 Collapse under Enhanced Cooling

Figure 3.5 shows the final simulation output on various scales for both the $J_{\text{XR}} = 0$ and the shielded $J_{\text{XR}} = 10^2 J_0$ case. While the expected filamentary structure is visible in all cases, the effects of X-ray heating in the $J_{\text{XR}} = 10^2 J_0$ case are readily apparent, with the low-density filamentary gas experiencing significant heating. With the usual definition of the virial radius R_{vir} as $\rho = \rho_{\text{vir}} \equiv 178 \rho_b$, where ρ , ρ_{vir} and ρ_b are

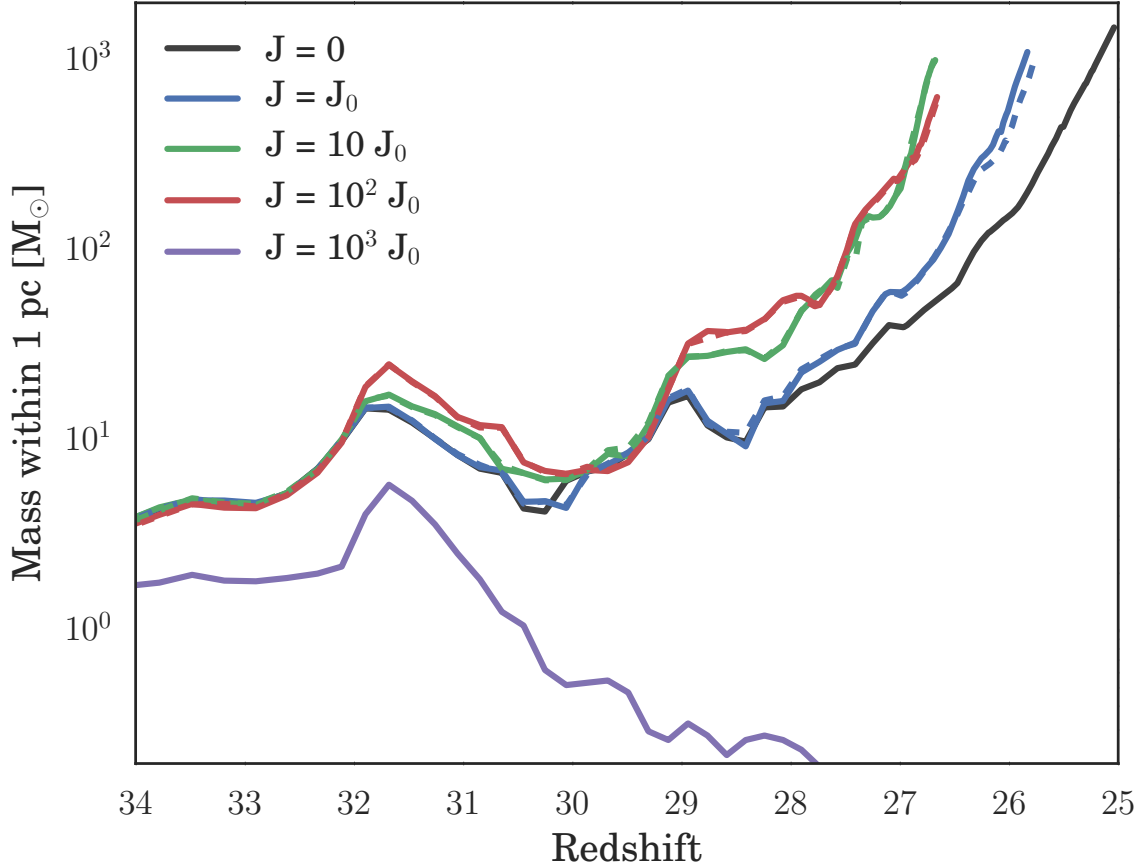


Figure 3.7: Total gas mass within 1 pc of the highest density point in each simulation over cosmic time. Shielded simulations are denoted by solid lines, unshielded simulations by dashed lines. Both with and without shielding, as J_{XR} increases, the gas in the loitering phase becomes cooler. This lowers the Jeans mass, allowing the gas to collapse to high densities sooner.

the average halo density, the density at the point of virialisation and the background density at the time of halo virialisation, we find that our $J_{\text{XR}} = 0$ minihalo collapses at $z = 25.04$ with $R_{\text{vir}} \simeq 85$ pc and $M_{\text{vir}} \simeq 2.1 \times 10^5 M_{\odot}$, typical for the minihalo environment (Bromm, 2013).

After the minihalo virialises, the gas continues to collapse in accordance with the standard picture of Pop III star formation (e.g., Stacy et al., 2010; Greif et al., 2012;

Stacy & Bromm, 2013). This picture is modified slightly in the presence of an X-ray background, but in the $J_{\text{XR}} = 0$ case the gas heats adiabatically until reaching $n \sim 1 \text{ cm}^{-3}$, attaining temperatures of $\sim 1000 \text{ K}$. Beyond this point, the gas is able to cool via the ro-vibrational modes of H_2 , reaching a minimum temperature of $\sim 200 \text{ K}$ at a density of $n \sim 10^4 \text{ cm}^{-3}$. After exiting the quasi-hydrostatic ‘loitering phase’ (Bromm et al., 2002), the gas enters runaway collapse until $n \sim 10^8 \text{ cm}^{-3}$, when three-body reactions become important. This process turns the gas fully molecular by $n \sim 10^{12} \text{ cm}^{-3}$, the density at which we form sink particles. As seen in Figure 3.6, this basic picture holds true even as we vary the strength of the CXB by several orders of magnitude.

We find that X-ray heating dominates at low densities in all cases, while above $n \sim 10^2 \text{ cm}^{-3}$ the additional cooling catalysed by X-ray ionisation exceeds it; the precise density at which this transition occurs depends on the strength of the CXB. This enhanced cooling significantly impacts the subsequent evolution of the gas as it collapses to high densities; the minimum temperature of the gas in the loitering phase approaches the CMB floor as J_{XR} increases, and—in the unshielded simulations—remains cooler than the $J_{\text{XR}} = 0$ case in all later stages of the collapse. This allows the gas to more easily fulfil the Jeans criterion and thus collapse sooner, as demonstrated by Figure 4.5.

When shielding is properly accounted for, the gas becomes optically thick to X-rays as it exits the loitering phase and proceeds to runaway collapse (see Figure 3.4). In the absence of continued X-ray ionisation, the free electron fraction decays, re-converging with that of the $J_{\text{XR}} = 0$ case. Consequently, the thermodynamic behaviour of the gas at high densities in the shielded simulations is remarkably similar,

even as we vary the CXB strength by several orders of magnitude as shown in Figure 3.6. This convergence under a wide range of X-ray backgrounds is similar to the behaviour noted by Stacy et al. (2011a) and Greif et al. (2011b) in the presence of dark matter–baryon streaming, though we observe an earlier—rather than a later—collapse.

3.4.1.2 Collapse Suppression

Minihalo collapse in the $J_{\text{XR}} = 1000 J_0$ case is completely suppressed. While the gas in the very centre of the minihalo does initially begin to cool via H₂, this process is quickly overwhelmed by heating from the increasingly strong X-ray background. Despite reaching densities and temperatures approaching $n \simeq 50 \text{ cm}^{-3}$ and $T \simeq 200 \text{ K}$ this cold core is eventually dissipated as the CXB continues to heat the gas. The reason for this suppression is demonstrated clearly in Figure 3.8, where we have shown the enclosed mass and the Jeans mass as a function of radius for both the $J_{\text{XR}} = 0$ and the $J_{\text{XR}} = 1000 J_0$ case. Here, we calculate the Jeans mass using the average density and temperature within a given radius, extending out to the virial radius of the halo. The $J_{\text{XR}} = 0$ case is shown just prior to the formation of the first sink particle in that simulation; the $J_{\text{XR}} = 1000 J_0$ case is shown at the maximum density reached over the course of the simulation. While the enclosed mass in the $J_{\text{XR}} = 0$ minihalo exceeds the Jeans mass on all scales, and thus is universally collapsing, the cold core in the $J_{\text{XR}} = 1000 J_0$ minihalo never gains sufficient mass to exceed the Jeans criterion.

3.4.2 Sink Particle Formation and Accretion

3.4.2.1 Build-up of a Central Disc

Figure 3.9 shows the growth over time of all sink particles formed in our simulations, from the formation of the first sink to simulation’s end 5000 yr later. Sink particles are formed when the gas in the centre of the minihalo reaches 10^{12} cm^{-3} , and in all cases a central disc forms within 300 yr of the first sink particle, as seen in Figure 3.10, where we have shown the density structure of the central 10^4 AU of each simulation. In the absence of any X-ray irradiation, the accretion disc fragments and forms a stable binary system, in agreement with previous studies (e.g., Stacy et al., 2010; Clark et al., 2011a,b; Greif et al., 2011a, 2012). When self-shielding is properly accounted for, the thermodynamic state of the gas in X-ray irradiated minihaloes is remarkably similar to the $J_{\text{XR}} = 0$ case by the time it reaches sink formation densities. The mass distribution, however, is in all cases significantly steeper than in the $J_{\text{XR}} = 0$ case, as shown in Figure 3.11. This is a direct consequence of the earlier collapse discussed in Section 3.4.1.1: the sooner the gas collapses to high densities, the less time is available for gas to accumulate in the centre of the minihalo.

Once sink formation densities are achieved, there is no clear trend in the subsequent behaviour of the sink particles formed—either in number or accretion rate. As seen in Table 3.1, both the virial mass of the minihalo and the cold core mass (defined here as $n \geq 10^2 \text{ cm}^{-3}$) decrease with increasing J_{XR} , as expected given the earlier collapse induced by a stronger CXB. However, at higher densities the $10 J_0$ case breaks this trend, suggesting that the final stages of the collapse are somewhat chaotic, and influenced more by small-scale randomness related to turbulence than by the strength of the CXB.

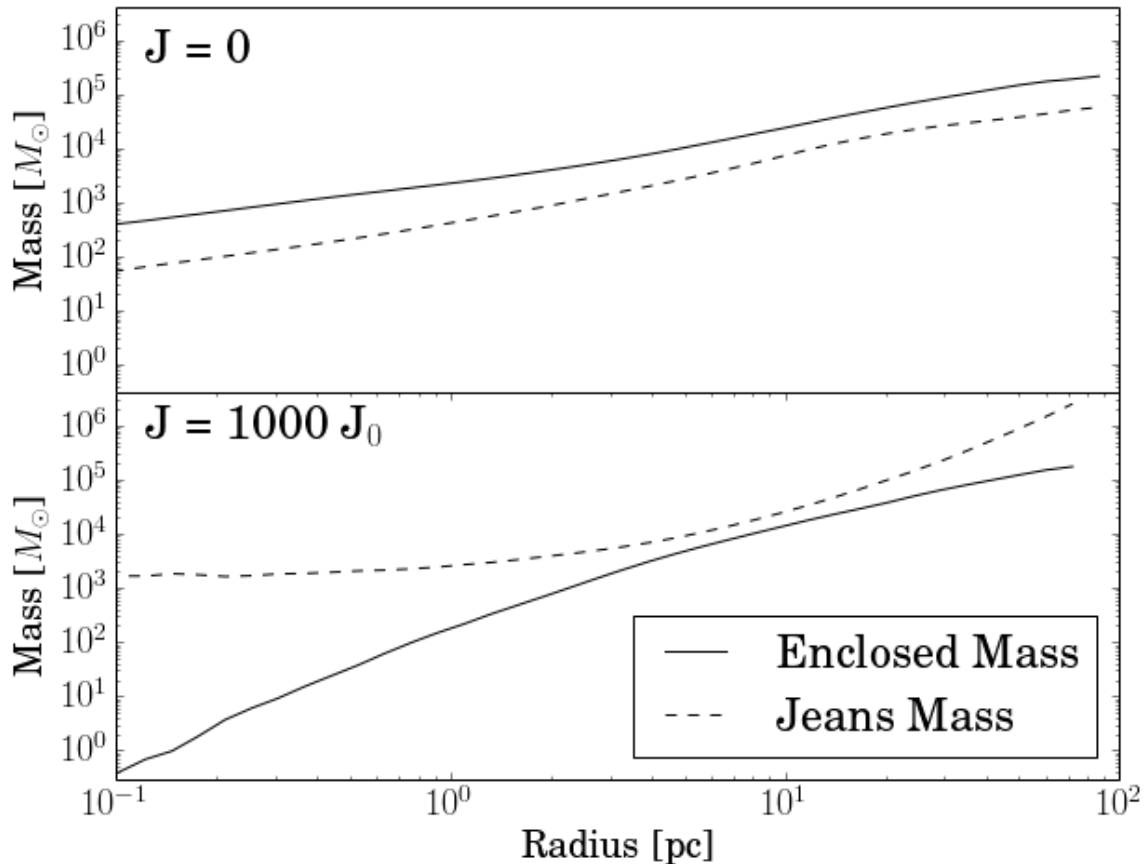


Figure 3.8: Shown here are the Jeans mass (dotted lines) and total enclosed mass (solid lines) within a given radius for both the $J_{\text{XR}} = 0$ (upper panel) and $J_{\text{XR}} = 1000 J_0$ case (lower panel). Here we calculate the Jeans mass using the average density and temperature within that radius, extending out to the virial radius of the halo. The $J_{\text{XR}} = 0$ case is shown just prior to the formation of the first sink particle; the $J_{\text{XR}} = 1000 J_0$ case is shown at the maximum density reached over the course of the simulation.

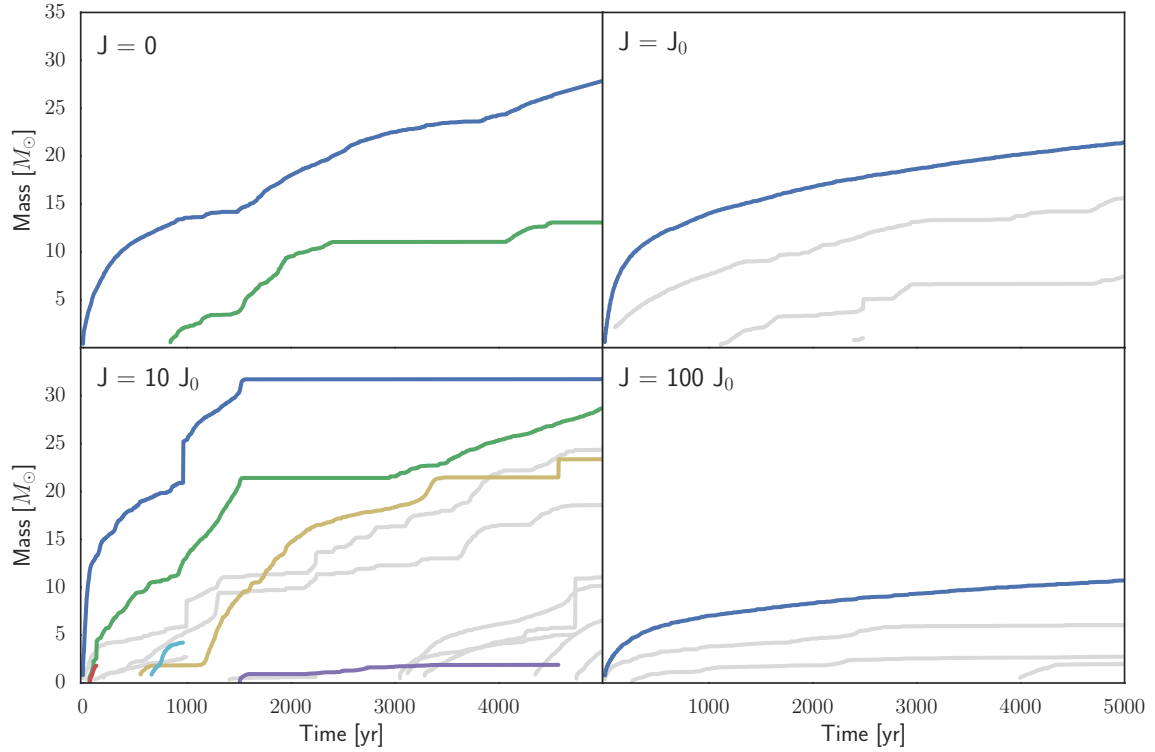


Figure 3.9: Growth of individual sink particles over time. Sinks for the shielded simulations are coloured throughout in order of formation: blue, green, red, yellow, cyan, and purple. Lines end where one sink is accreted by another. The light grey lines show the growth history of sinks in the unshielded simulations for comparison. Note that in the absence of shielding, more sinks form, but the total mass remains roughly constant.

Table 3.1: Total gas mass in various minihalo components for each simulation at $t = 5000$ yr. Here we have defined M_{core} and M_{disc} as the total gas mass with $n \geq 10^2 \text{ cm}^{-3}$ and $n \geq 10^8 \text{ cm}^{-3}$, respectively. These values are independent of whether shielding is included.

J_{XR}	M_{vir} ($10^4 M_{\odot}$)	M_{core} ($10^3 M_{\odot}$)	M_{disc} (M_{\odot})	M_{sink} (M_{\odot})
0	2.4	2.5	100	41
J_0	2.2	2.2	60	23
$10 J_0$	1.9	2.1	130	74
$100 J_0$	1.2	1.3	30	11

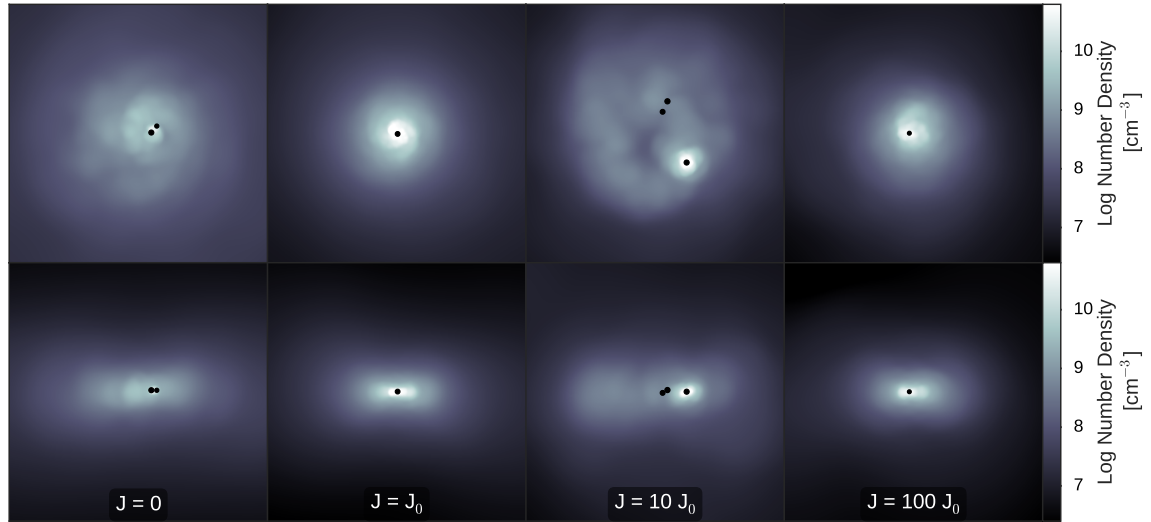


Figure 3.10: Density projection of the central 10000 AU of each simulation 5000 yr after formation of the first sink particle. From left to right: $J_{\text{XR}} = 0, J_0, 10 J_0, 10^2 J_0$. Top row shows the face-on density projection; bottom row shows an edge-on projection. Black dots mark the location of all sink particles, and scale with the mass of the sink.

3.4.2.2 Disc Fragmentation

In the absence of shielding, the gas invariably fragments, forming a binary or small multiple within 1000 yr. When shielding is properly accounted for though, excess cooling of the disc ($n \gtrsim 10^8 \text{ cm}^{-3}$; see Figure 3.6) is eliminated, and fragmentation is suppressed. In fact, only a single sink particle forms in both the $J_{\text{XR}} = J_0$ and $100 J_0$ cases, and while the $10 J_0$ simulation still fragments, it does so considerably less than in the absence of shielding. We may quantify this using the Toomre Q parameter (Toomre, 1964):

$$Q = \frac{c_s \kappa}{\pi G \Sigma} \quad (3.29)$$

where c_s is the gas sound speed, κ is the epicyclic frequency of the disc, and Σ is the surface density; we replace κ with the orbital frequency Ω , as appropriate for

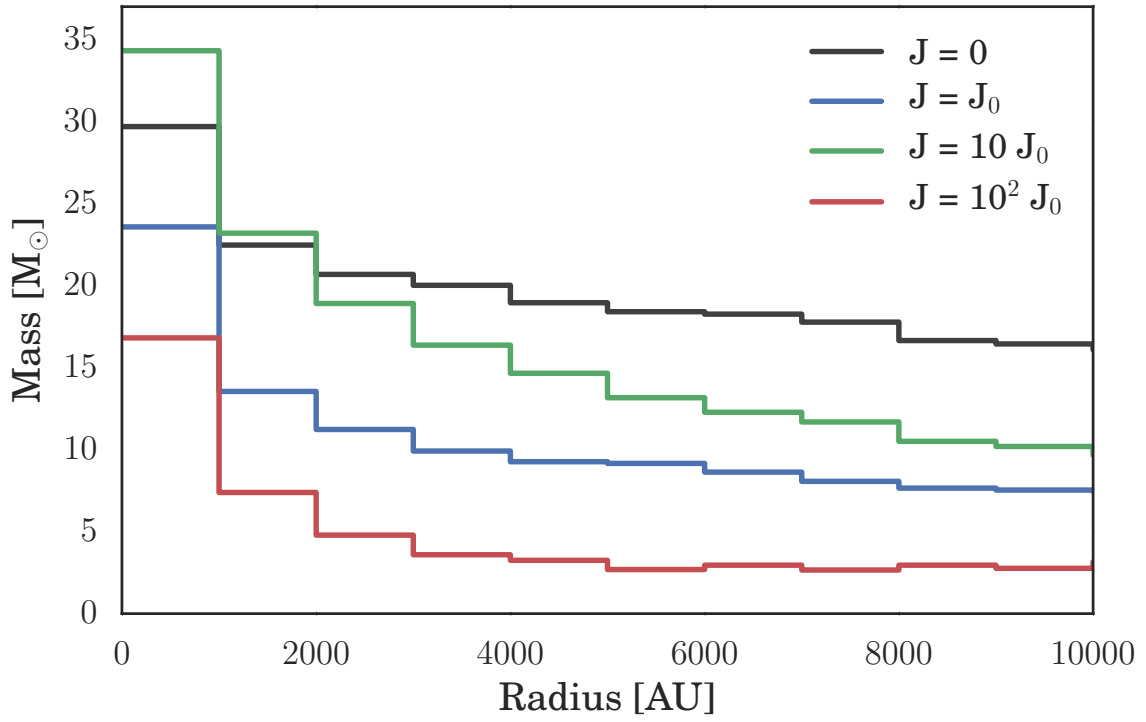


Figure 3.11: Total gas mass in successive radial bins of 500 AU centred on the highest density point in the simulation. Shown is the mass distribution just prior to the formation of the first sink particle.

Keplerian discs. While the Q parameter specifically applies to infinitely thin isothermal discs, it is correct to within a factor of order unity when applied to thick discs (Wang et al., 2010), as is the case here. Figure 3.12 shows the Q parameter evaluated in mass-weighted spherical shells centred on the accretion disc 5000 yr after the first sink particle has formed. As the mass within these shells is dominated by the disc component, applying this analysis to the disc particles alone would have a negligible impact on the results (e.g., Greif et al., 2012). The $J_{\text{XR}} = 0$ and $10 J_0$ simulations maintain $Q \lesssim 1$ throughout the disc, and are thus susceptible to fragmentation. On the other hand, save for the central few hundred AU, where they approach the resolution limit of the simulation, the J_0 and $100 J_0$ discs stay well above $Q = 1$, hence

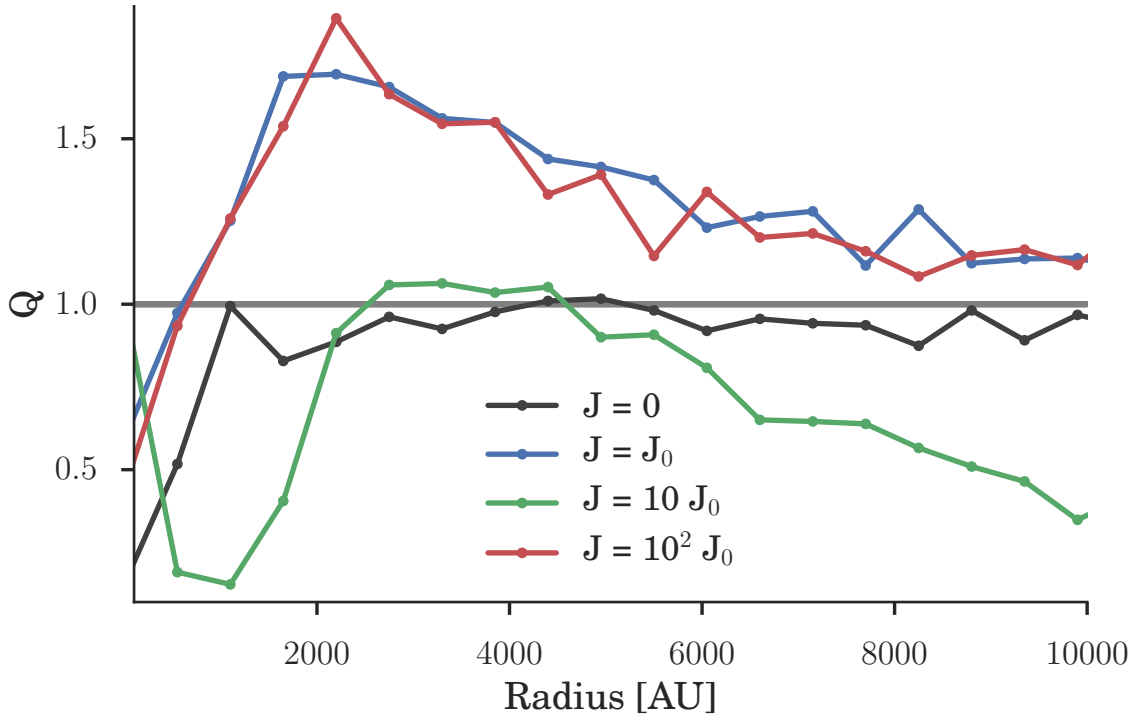


Figure 3.12: The Toomre Q parameter versus radius shown 5000 yr after the first sink particle forms in each simulation. The accretion disc is susceptible to fragmentation when $Q \lesssim 1$, as is the case for the $J_{\text{XR}} = 0$ and $10 J_0$ cases.

the lack of fragmentation.

While the $J_{\text{XR}} = 10 J_0$ minihalo also collapses early, in the same manner as the J_0 and $100 J_0$ simulations, it still experiences significant fragmentation. This is primarily due to the specific details of its collapse history, modulated by small-scale turbulence, rather than the precise value of J_{XR} , and can be understood by examining the velocity profile of the minihalo, shown in Figure 3.13 along with the Shu accretion rate (Shu, 1977) for mass-weighted spherical bins out to ~ 10 pc. While the inner regions of the $10 J_0$ accretion disc exhibit approximately Keplerian rotation in line with the other simulations, the gas at large radii experiences significantly less rotational support.

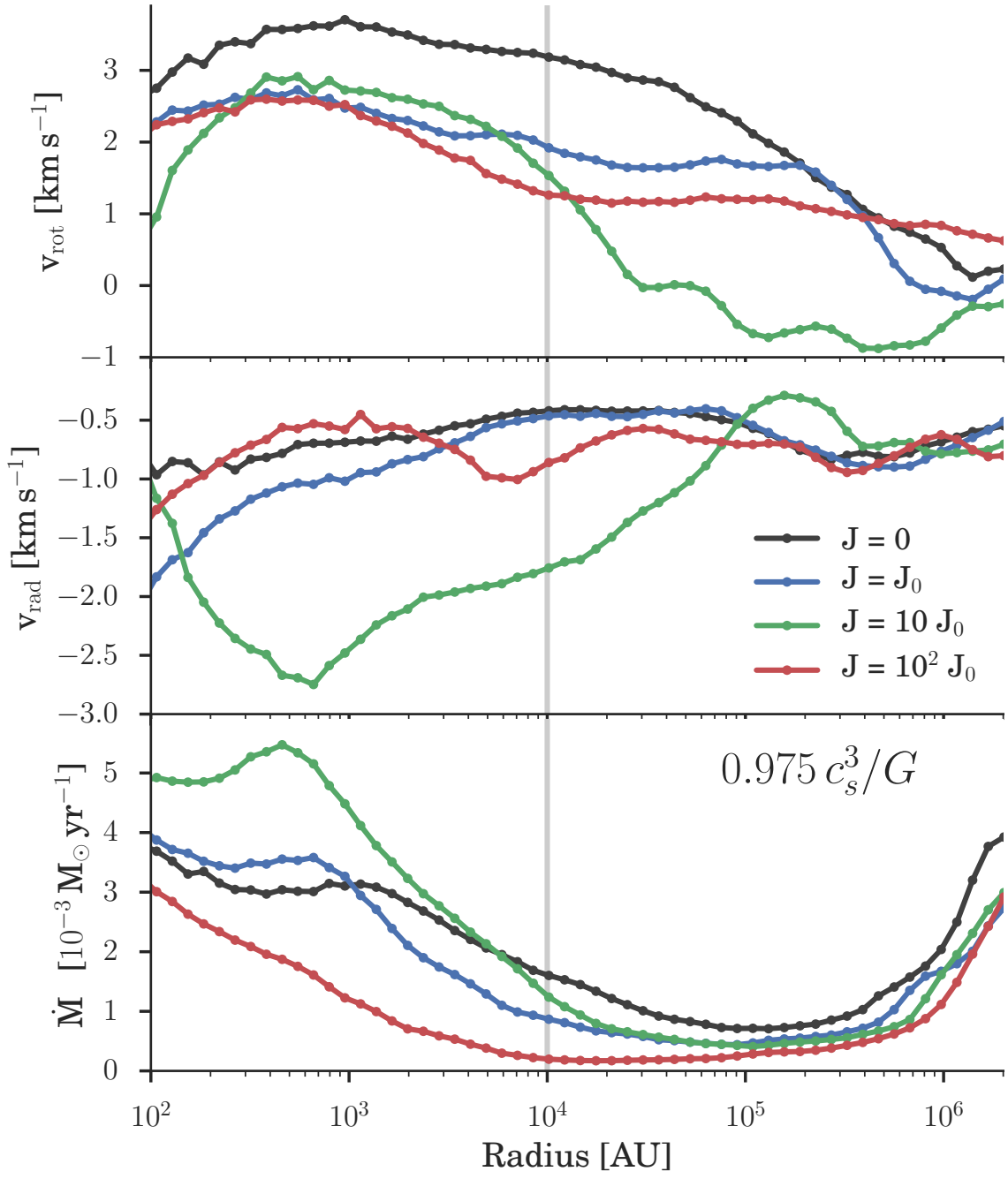


Figure 3.13: From top to bottom: the rotational velocity, radial velocity, and Shu accretion rate versus distance to the centre of the minihalo for each simulation as denoted in the legend. The vertical gray line at 10^4 AU marks the approximate limit of the accretion disc, and the limit to which Figures 3.10, 3.11 and 3.12 are displayed. Note the significant discrepancies in the behaviour of the $J_{\text{XR}} = 10 J_0$ case in each panel.

This results in a much larger infall velocity, leading in turn to a higher accretion rate. This overwhelms the ability of the accretion disc to support itself against the growth of perturbations, resulting in significant fragmentation.

3.5 Summary and Conclusions

We have performed a suite of cosmological simulations employing a range of CXB models, focusing on the impact of such a background on Pop III stars forming in a minihalo. As three-body processes turn the gas fully molecular by $n = 10^{12} \text{ cm}^{-3}$, following the evolution of the gas up to this density allows us to fully capture the impact of a CXB on H₂ and HD cooling in the gas. After the gas reaches 10^{12} cm^{-3} we form sink particles, enabling us to study the subsequent evolution of the system, which we follow for an additional 5000 yr.

X-rays have two competing effects on primordial gas, as ionising the gas serves to both heat it and increase the number of free electrons, which catalyse the formation of molecular hydrogen. As H₂ is the main coolant in primordial gas, this actually enhances cooling. We find that heating dominates in low density gas, but is overwhelmed at higher densities by the enhanced cooling X-rays provide. The transition between these two regimes occurs between $n = 1$ and 100 cm^{-3} , depending on the strength of the CXB.

Previous work investigating the impact of a CXB on structure formation in the early universe has generally been found to increase the supply of cold gas in a given halo (Haiman et al., 2000; Venkatesan et al., 2001; Glover & Brand, 2003; Cen, 2003; Kuhlen & Madau, 2005; Jeon et al., 2012). In particular, Kuhlen & Madau (2005) found the increase in cold gas available for star formation was greatest in

2×10^5 – $10^6 M_\odot$ minihaloes, where the increase could exceed 1–2 orders of magnitude for moderate X-ray ionisation rates. This comports with our findings—allowing the X-ray irradiated haloes to evolve to the same cosmic time as the $J_{\text{XR}} = 0$ minihalo would result in a relatively larger supply of cold dense gas. As X-rays penetrating the minihalo begin to experience significant attenuation above $n \sim 10^6 \text{ cm}^{-3}$ though, the primary impact of a CXB is on gas in the loitering phase and below. While X-ray heating dominates below $n \sim 1 \text{ cm}^{-3}$, minihaloes that overcome this impediment collapse earlier, as the cooler gas in the loitering phase requires a smaller Jeans mass to proceed to high densities.

The X-ray background is severely attenuated by the time it reaches sink formation densities. As a result its impact on the gas temperature is largely neutral, with the subsequent behaviour of the sink particles formed influenced more by small-scale turbulence than the strength of the CXB. Consequently, the characteristic mass of the stars formed is quite stable even as we vary the CXB strength by several orders of magnitude, and does not change dramatically even when the supply of cold gas in the centre of the minihalo is significantly increased, as in the $10 J_0$ case. Instead, this causes the disc to fragment, forming several protostellar cores.

It should be noted that these findings are somewhat sensitive to the density at which the minihalo becomes opaque to X-rays. While we found no difference in the total column density between simulations, a more robust estimate of the local column density would be beneficial (e.g., Hartwig et al., 2015; Safranek-Shrader et al., 2012). Additionally, there is a possibility that the more rapid minihalo collapse induced by a strong CXB may have an impact on the velocity dispersion of the infalling gas, suppressing fragmentation and possibly increasing the mass of the stars

formed. While our simulations lack sufficient resolution to verify this, the findings of Clark et al. (2011a) suggest that stars forming in pre-ionised minihaloes experience more turbulence, resulting in a somewhat larger characteristic mass than in pristine minihaloes. Finally, our findings may have implications for reionisation and the 21-cm signal (Furlanetto et al., 2006; Mirocha, 2014): while the impact on the number of fragments and characteristic mass of Pop III appears to be nearly neutral, low-density gas is still smoothed by X-ray heating, thus resulting in a lower IGM clumping factor.

Chapter Four: Population III Star Formation Under Cosmic Ray Feedback

4.1 Introduction

Cosmic rays (CRs) have long been known to play an important role in the complex physics and chemistry of the interstellar medium (ISM) in local galaxies (Spitzer & Tomasko 1968; Spitzer & Scott 1969; Glassgold & Langer 1973; Goldsmith & Langer 1978; Cravens & Dalgarno 1978; Mannheim & Schlickeiser 1994; Tielens 2005; recently reviewed by Strong et al. 2007; Grenier et al. 2015). They are an effective source of ionisation and heating in various environments, from preheating the primordial intergalactic medium (IGM; Sazonov & Sunyaev, 2015), to driving outflows in the diffuse ISM (e.g., Enßlin et al., 2007; Jubelgas et al., 2008; Salem & Bryan, 2014; Hanasz et al., 2013; Booth et al., 2013; Salem et al., 2014), to providing an important (often dominant) source of heating and ionisation in deeply embedded gas clouds and protostellar discs (Spitzer, 1978; Dalgarno et al., 1999; Indriolo et al., 2009; Padovani et al., 2009; Glassgold et al., 2012; Padovani et al., 2013, 2015).

CRs are particularly interesting in the context of Population III (Pop III) star formation, as they provide a continually replenished source of free electrons, enhancing the formation of molecular hydrogen—the only coolant available in primordial gas (Abel et al., 1997; Galli & Palla, 1998; Bromm et al., 2002). This enhances the ability of the gas to cool, modifying the characteristic density and temperature at which runaway gravitational collapse sets in, and possibly the characteristic mass of the stars

thus formed. The characteristic mass of Pop III is critical, as it largely controls the extent to which the first stars influence their environment, determining both their total luminosity and ionising radiation output (Schaerer, 2002), in addition to the details of their eventual demise (Heger et al., 2003; Heger & Woosley, 2010; Maeder & Meynet, 2012). As such, a thorough understanding of how the very first stars impact subsequent episodes of metal-free star formation—sometimes referred to as Pop III.1 and Pop III.2, respectively (McKee & Tan, 2008)—is crucial to developing a comprehensive picture of cosmic evolution.

In the absence of any feedback, pioneering numerical studies suggested that the very first stars were quite massive—on the order of $100 M_{\odot}$ (e.g., Bromm et al., 1999, 2002; Abel et al., 2002; Yoshida et al., 2003; Bromm & Larson, 2004; Yoshida et al., 2006; O’Shea & Norman, 2007). However, more recent simulations, aided by increased resolution, have found that significant fragmentation occurs during the star formation process (Stacy et al., 2010; Clark et al., 2011a,b; Greif et al., 2011a, 2012; Stacy & Bromm, 2013; Hirano et al., 2014; Hosokawa et al., 2015), leading to the emerging consensus that the Pop III initial mass function (IMF) was somewhat top-heavy with a characteristic mass of \sim a few $\times 10 M_{\odot}$ (Bromm, 2013). While the contribution these stars make to chemical enrichment (Madau et al. 2001; Mori et al. 2002; Bromm et al. 2003; Heger et al. 2003; Umeda & Nomoto 2003; Tornatore et al. 2007; Greif et al. 2007, 2010; Wise & Abel 2008; Maio et al. 2011; recently reviewed in Karlsson et al. 2013) and reionisation (Kitayama et al., 2004; Sokasian et al., 2004; Whalen et al., 2004; Alvarez et al., 2006; Johnson et al., 2007; Robertson et al., 2010) have been well studied, the consequences for Pop III stars forming in neighbouring minihaloes have been less thoroughly explored.

As Pop III stars form in a predominantly neutral medium, the majority of their ionising output is absorbed, allowing only radiation less energetic than the Lyman- α transition to escape the immediate vicinity of the star-forming halo. While far-ultraviolet radiation in the Lyman-Werner (LW) bands (11.2 – 13.6 eV) lacks sufficient energy to interact with atomic hydrogen, it can still effectively dissociate molecular hydrogen. However, studies have found that the expected mean value of such radiation is far below the critical LW flux required to suppress H₂ cooling (Dijkstra et al., 2008). At the high energy end, the neutral hydrogen cross section for X-rays and cosmic rays is small, allowing them to easily escape their host mini-haloes. We recently investigated the impact of a cosmic X-ray background generated by high-mass X-ray binaries on primordial star formation (Hummel et al., 2015); here we focus on the impact of a CR background consisting of particles accelerated in supernova shock waves via the first-order Fermi process (see Section 4.2).

While the uncertainties involved in estimating the strength of the high- z CR background are huge, measurements of the ⁶Li abundance from metal-poor stars in the Galactic halo provide a useful constraint: the observed abundance of ⁶Li is approximately 1000 times higher than predicted by big bang nucleosynthesis (Asplund et al., 2006), strong evidence for the existence of a CR spallation channel to provide a ⁶Li bedrock abundance prior to the bulk of star formation (Rollinde et al., 2005, 2006). Production of this first pervasive CR background by shock-acceleration in Pop III supernovae dovetails nicely with the upper limits this places on the CR energy density at high redshifts (Rollinde et al., 2006).

Early studies of the impact of CRs on primordial star formation focused on the production of ultra-high-energy CRs (UHECRs) by the decay of ultra-heavy X particles

(Shchekinov & Vasiliev, 2004; Vasiliev & Shchekinov, 2006; Ripamonti et al., 2007).

With energies above the Greisen–Zatsepin–Kuzmin (GZK) cutoff (Greisen, 1966; Zatsepin & Kuz'min, 1966), UHECRs interact with the cosmic microwave background (CMB) to produce ionising photons, which in turn enhance the free electron fraction of the gas. Other work investigated the direct collisional ionisation of neutral hydrogen by SN shock-generated CRs, using one-zone models to determine the impact of a CR background on the chemical and thermal evolution of the gas in a minihalo (Stacy & Bromm, 2007; Jasche et al., 2007). These studies found that the presence of a CR background enhanced molecular hydrogen formation in the minihalo, cooling the gas and lowering the Jeans mass, and by extension, the characteristic mass of the stars formed. We expand upon these one-zone models, using three-dimensional *ab initio* cosmological simulations to investigate the impact of a CR background on Pop III stars forming in a minihalo.

This paper is organized as follows: In Section 4.2 we provide the cosmological context for this study, estimating the expected intensity of the CR background. Our numerical methodology is described in Section 4.3, while our results are presented in Section 4.4. Finally, our conclusions are gathered in Section 4.5. Throughout this paper we adopt a Λ CDM model of hierarchical structure formation, using the following cosmological parameters, consistent with the latest measurements from the Planck Collaboration (Ade et al., 2015): $\Omega_\Lambda = 0.7$, $\Omega_m = 0.3$, $\Omega_B = 0.04$, and $H_0 = 70 \text{ km s}^{-1} \text{ Mpc}^{-1}$.

4.2 Cosmic Rays in the Early Universe

While there are several possible sources of CRs at high redshifts including primordial black holes, topological defects, supermassive particles, and structure formation shocks, the most likely source in the early Universe is supernova (SN) explosions (e.g., Ginzburg & Syrovatskii, 1969; Biermann & Sigl, 2001; Stanev, 2004; Pfrommer et al., 2006), wherein CRs are accelerated by the SN shock wave via the first-order Fermi process (e.g., Bell, 1978). In this scenario, high-energy particles diffuse back and forth across the shock front, increasing their energy by a small percentage each time, and resulting in a differential spectrum of CR number density per energy (Longair, 1994) of the form

$$\frac{dn_{CR}}{d\epsilon} = \frac{n_{norm}}{\epsilon_{min}} \left(\frac{\epsilon}{\epsilon_{min}} \right)^{-2}, \quad (4.1)$$

where n_{CR} is the CR number density, ϵ is the kinetic energy of the CR, ϵ_{min} is the low-energy cutoff of the CR spectrum, and n_{norm} is a normalising density factor.

The value of ϵ_{min} is crucial, as the ionisation cross-section of non-relativistic CRs varies roughly as ϵ^{-1} for $\epsilon \gtrsim 10^5$ eV. Higher energy CRs thus travel much farther between interactions and are less able to effectively deposit their energy into the gas, such that the low-energy end of the CR spectrum provides the majority of the ionisation and heating. While estimates of the lowest possible energy CR protons could gain in a SN shock wave vary significantly, below 10^5 eV the velocity of the CR drops below the approximate orbital velocity of electrons in the ground state of atomic hydrogen, and the interaction cross-section diminishes rapidly (Schlickeiser, 2002).

We therefore employ $\epsilon_{min} = 10^6$ eV as the lower bound for the CR background in our simulations. While CRs with energies below 10^6 eV may account for $\sim 5 - 50$

percent of the CR energy budget, they also deposit a substantial fraction of their energy into the IGM (Sazonov & Sunyaev, 2015). Consequently, they are unable to efficiently contribute to the build-up of a large-scale CR background. We thus neglect the contribution such CRs make to the ionisation and heating of primordial gas. However, this introduces only minor errors, as shown by Stacy & Bromm (2007). Using one-zone models, they found that extending the CR spectrum to as low as $\epsilon_{\min} = 10^3$ eV altered the resulting ionisation and heating rates by less than a factor of two. It should also be noted that the uncertainty in ϵ_{\min} is on par with that for the fraction of the SN energy going into CR production, f_{CR} , which is expected to be $\sim 10 - 20$ percent (Caprioli & Spitkovsky, 2014). Here we assume $f_{CR} = 0.1$.

The upper limit of the CR energy spectrum ϵ_{\max} depends on the strength of the ambient magnetic field in the local ISM, as the Fermi acceleration process is linearly dependent on the magnetic field through which the SN shock wave propagates. As the strength, generation mechanism, and distribution of magnetic fields in the early Universe remain highly uncertain (Durrer & Neronov, 2013), we set $\epsilon_{\max} = 10^{15}$ eV, a typical maximum value from Fermi acceleration theory in SN shocks (e.g., Blandford & Eichler, 1987). So long as ϵ_{\max} is below the GZK cutoff, ϵ_{GZK} , at that redshift, given by (Stacy & Bromm, 2007)

$$\epsilon_{GZK}(z) = \frac{5 \times 10^{19} \text{ eV}}{1 + z}, \quad (4.2)$$

the precise value of ϵ_{\max} is not crucial, since the great majority of the heating and ionisation is provided by CRs near ϵ_{\min} .

Magnetic fields also play an important role in isotropising the CR background. We may estimate the effective mean free path over which a CR can freely propagate before being significantly impacted by the presence of a magnetic field B using the

Larmor radius r_L , where for a proton,

$$r_L = \frac{\gamma m_H \beta c^2}{eB}. \quad (4.3)$$

Here, γ is the Lorentz factor of the CR; m_H , the proton mass; e , the proton charge; c , the speed of light, and βc is the CR velocity. The CR background at redshift z for protons with energy ϵ may then be considered fully isotropic if $r_L(\epsilon) \ll D_H(z)$ where $D_H(z)$ is the Hubble distance at that epoch. Recent observations have placed lower bounds on the modern-day intergalactic magnetic field strength ranging from 10^{-18} G (Dermer et al., 2011) to 3×10^{-16} G (Neronov & Vovk, 2010), while other estimates place the field strength as high as 10^{-15} G (Ando & Kusenko, 2010). Simply accounting for flux freezing, the magnetic field at redshift z is given by

$$B(z) = B_0(1+z)^2, \quad (4.4)$$

where B_0 is the magnetic field at the current epoch. The magnetic field strength in the IGM at $z = 20$ then was likely in the range 4×10^{-16} to 4×10^{-13} G. The magnetic field strength required to fully randomize the path of a 10^{15} eV CR proton is $\sim 10^{-14}$ G; we may therefore assume the CR background is fully isotropic to the limit of our CR spectrum. The Larmor radius for a 10^6 eV CR proton in a 10^{-15} G magnetic field, on the other hand, is ~ 10 pc. While unable to freely propagate, under the assumption that magnetic fields at these redshifts are disordered on pc scales, such CRs will diffuse through the IGM with a diffusion coefficient $D = cr_L$. Given that the typical physical distance L between minihaloes at $z = 20$ —derived from the Press-Schechter (1974) formalism—is ~ 5 kpc, the diffusion time between minihaloes, $t_{\text{diff}} = L^2/D$, is of order 10^{14} s, less than the Hubble time at this epoch. 10^6 eV CRs are thus able to build up a locally isotropic background on scales larger than the typical distance between minihaloes. On the scale of our simulation boxes (see

Section 4.3.1), CRs are thus able to build up an effectively uniform and isotropic background from 10^6 to 10^{15} eV, an assumption we make throughout the remainder of our analysis.

Normalising the differential CR spectrum with the aforementioned limits ϵ_{\min} and ϵ_{\max} to the total energy density in cosmic rays, u_{CR} , results in a CR energy spectrum increasing over cosmic time in the following fashion:

$$\frac{dn_{\text{CR}}}{d\epsilon}(z) = \frac{u_{\text{CR}}(z)}{\epsilon_{\min}^2 \ln \epsilon_{\max}/\epsilon_{\min}} \left(\frac{\epsilon}{\epsilon_{\min}} \right)^{-2}. \quad (4.5)$$

Here we estimate u_{CR} as follows:

$$u_{\text{CR}}(z) = f_{\text{CR}} E_{\text{SN}} f_{\text{SN}} \Psi_*(z) t_H(z) (1+z)^3, \quad (4.6)$$

where f_{CR} is the fraction of the SN explosion energy E_{SN} going into CR production, f_{SN} is the mass fraction of stars formed which die as SNe, and $\Psi_*(z)$ is the comoving star formation rate density (SFRD) as a function of redshift, which we assume to be constant over a Hubble time t_H . The factor of $(1+z)^3$ accounts for the conversion from a comoving SFRD to a physical energy density. As in Hummel et al. (2015), we base our estimate of $u_{\text{CR}}(z)$ on the Pop III SFRD calculated by Greif & Bromm (2006), but see Campisi et al. (2011) for a more recent calculation.

The mass fraction of Pop III stars dying as SNe depends strongly on their IMF, and while the complex physical processes at play in gas collapsing from IGM to protostellar densities have so far prevented a definitive answer to this question, the emerging consensus is that the Pop III IMF was somewhat top-heavy with a characteristic mass of \sim a few $\times 10 M_\odot$ (Bromm, 2013). Given this, we assume one SN is produced for every $50 M_\odot$ of stars formed and each SN-producing star dies quickly as a core-collapse explosion with $E_{\text{SN}} = 10^{51}$ erg, 10 percent of which goes into CR production.

This fiducial estimate for $u_{\text{CR}}(z)$ —henceforth referred to as model u_0 —is shown in Figure 4.1, where we compare the energy density in CRs to the gas thermal energy density in the IGM, the range of estimates for the IGM magnetic field energy density, and the energy density of the cosmic microwave background. We also mark the most conservative upper limits placed on u_{CR} by Rollinde et al. (2006), calculated using the observed overabundance of ${}^6\text{Li}$ compared to big bang nucleosynthesis. Given the huge uncertainties inherent in estimating the strength of the high- z CR background, we also consider five additional models with 10 , 10^2 , 10^3 , 10^4 , and 10^5 times the energy density of model u_0 , as shown in Figure 4.1. This allows us to bracket the plausible range of energy densities, from values comparable to the IGM thermal energy density to just below the upper limits from ${}^6\text{Li}$ abundance measurements.

4.3 Numerical Methodology

Using the well-tested N -body smoothed particle hydrodynamics (SPH) code GADGET-2 (Springel, 2005), we perform our simulations using the same chemistry network and sink particle method as described in Hummel et al. (2015); the relevant details are summarized below. In addition to using the same initial conditions as in Hummel et al. (2015) to allow for a comparison of the impact of X-rays versus cosmic rays on the primordial gas, we perform a second suite of simulations using new initial conditions. The minihalo in these simulations collapses at a lower redshift; this allows us to ensure our results are not being influenced by the CMB temperature floor.

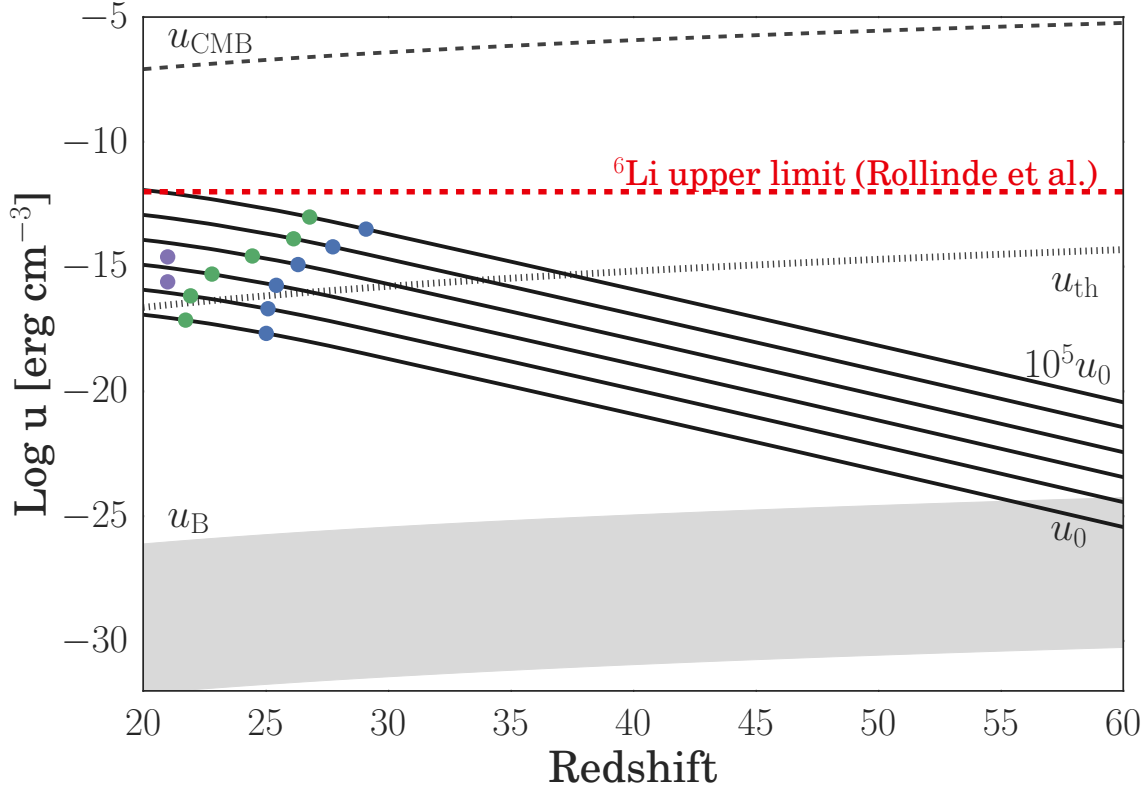


Figure 4.1: Cosmic ray energy density u_{CR} as a function of redshift. Our models, from u_0 to $10^5 u_0$ are indicated by solid black lines, while the energy density in the CMB and the thermal energy density in the IGM are denoted by dashed and dotted black lines, respectively. The grey region shows the range of possible values for the magnetic field energy density in the IGM, and the dashed red line marks the most conservative upper limit on the CR energy density from Rollinde et al. (2006), as derived from the ${}^6\text{Li}$ abundance. Blue points indicate the redshift at which Halo 1 collapses to high densities for a given u_{CR} ; green points, the redshift at which Halo 2 collapses. Finally, purple points denote the energy densities employed by Stacy & Bromm (2007) to study the impact of a CR background using one-zone models calculated at $z = 21$.

4.3.1 Initial Setup

The first set of simulations (henceforth referred to as Halo 1) use the same initial conditions as Hummel et al. (2015) and Stacy et al. (2010), and are initialised at $z = 100$ in a 140 comoving kpc box with periodic boundary conditions. To accelerate structure formation within the simulation box an artificially enhanced normalisation of the power spectrum, $\sigma_8 = 1.4$, was used, but the simulations are otherwise initialised in accordance with a Λ CDM model of hierarchical structure formation. For a discussion of the validity of this choice, see Stacy et al. (2010). High resolution in these simulations is achieved using a standard hierarchical zoom-in technique, with nested levels of refinement at 40, 30, and 20 kpc (comoving). Using this technique, the highest resolution SPH particles have a mass $m_{\text{SPH}} = 0.015 \text{ M}_\odot$, yielding a minimum mass resolution $M_{\text{res}} \simeq 1.5 N_{\text{neigh}} m_{\text{SPH}} \lesssim 1 \text{ M}_\odot$ for the simulation. Here $N_{\text{neigh}} = 32$ is the number of particles used in the SPH smoothing kernel (Bate & Burkert, 1997).

The initial conditions for the second set of simulations (henceforth referred to as Halo 2) are derived from the simulations described in Stacy & Bromm (2013). These simulations were initialised at $z = 100$ in a 1.4 comoving Mpc box in accordance with the same Λ CDM structure formation model as Halo 1, but with $\sigma_8 = 0.9$ rather than the artificially enhanced $\sigma_8 = 1.4$ used in Halo 1. The use of ‘marker sinks’ for regions reaching densities beyond $n = 10^3 \text{ cm}^{-3}$ rather than following the gas to higher densities allows for the efficient identification of the first 10 minihaloes to form within the box; we select the final minihalo to form—i.e., Minihalo 10 from Stacy & Bromm (2013)—for further study. After identifying the location of the final minihalo, the cosmological box is re-initialised at $z = 100$ using a standard zoom-in technique with two nested levels of refinement used to improve resolution surrounding

the selected minihalo. Each ‘parent’ particle within the most refined region is split into 64 ‘child’ particles, with a minimum mass of $m_{\text{gas}} = 1.85 \text{ M}_{\odot}$ and $m_{DM} = 12 \text{ M}_{\odot}$. These refined simulations are then run until the gas approaches the typical onset of runaway collapse at $n = 10^4 \text{ cm}^{-3}$.

4.3.1.1 Halo 2 Cut-out and Refinement

Once the simulation reaches 10^4 cm^{-3} all particles beyond 10 comoving kpc from the centre of the collapsing minihalo are removed to conserve computational resources. To achieve a maximum resolution comparable to Halo 1, all particles within the 10 comoving kpc volume are split into two child particles placed randomly within the smoothing kernel of the parent particle. This particle-splitting is repeated twice more; all particles within 8 comoving kpc are replaced by 8 child particles; within 6 comoving kpc, each of these child particles is split into an additional 8 for a total of 128 child particles in the most refined region. At each step, the mass of the parent particle is evenly divided among the child particles and the smoothing length is set to $hN_{\text{new}}^{-1/3}$, where h is the smoothing length of the parent and N_{new} is the number of child particles created. All particles inherit the same entropy, velocity, and chemical abundances as their parent, ensuring conservation of mass, internal energy, and momentum.

While our cut-out technique leads to a rarefaction wave propagating inward from the suddenly introduced vacuum boundary condition, the average sound speed at the edge of the most refined region is $\sim 1 \text{ km s}^{-1}$. As a result the wave only travels $\sim 0.5 \text{ pc}$ over the remaining 400,000 yr of the simulation, a negligible fraction of the $\sim 350 \text{ pc}$ physical box size.

4.3.2 Chemistry and Thermodynamics

We employ the chemistry network described in detail by Greif et al. (2009), which follows the abundance evolution of H, H⁺, H⁻, H₂, H₂⁺, He, He⁺, He⁺⁺, D, D⁺, HD and e⁻. All relevant cooling mechanisms are accounted for, including H and He collisional excitation and ionisation, recombination, bremsstrahlung and inverse Compton scattering.

In order to properly model the chemical evolution at high densities, H₂ cooling induced by collisions with H and He atoms and other H₂ molecules is also included. Three-body reactions involving H₂ become important above $n \gtrsim 10^8 \text{ cm}^{-3}$; we employ the intermediate rate from Palla et al. (1983), but see Turk et al. (2011) for a discussion of the uncertainty of these rates. In addition, the efficiency of H₂ cooling is reduced above $\sim 10^9 \text{ cm}^{-3}$ as the ro-vibrational lines of H₂ become optically thick above this density. To account for this we employ the Sobolev approximation together with an escape probability formalism (see Yoshida et al. 2006; Greif et al. 2011a for details).

4.3.3 Cosmic Ray Ionisation and Heating

Each time a CR proton ionises a hydrogen atom, an electron with average energy $\langle E \rangle = 35 \text{ eV}$ is produced (Spitzer & Tomasko, 1968). Including the ionization energy of 13.6 eV, the CR proton loses approximately 50 eV per scattering. This necessarily places a limit on how many scatterings a CR proton can undergo before losing all its energy to ionisation, as well as limiting the distance it may travel. This distance may be described by a penetration depth

$$D_p(n, \epsilon) \approx \frac{\beta c \epsilon}{-(d\epsilon/dt)_{ion}} \quad (4.7)$$

where (Schlickeiser, 2002)

$$-\left(\frac{d\epsilon}{dt}\right)_{ion}(n, \epsilon) = 1.82 \times 10^{-7} eV s^{-1} n_H f(\epsilon), \quad (4.8)$$

$$f(\epsilon) = (1 + 0.0185 \ln \beta) \frac{2\beta^2}{\beta_0^3 + 2\beta^3}, \quad (4.9)$$

and

$$\beta = \sqrt{1 - \left(\frac{\epsilon}{m_H c^2} + 1\right)^{-2}}. \quad (4.10)$$

Here, $(d\epsilon/dt)_{ion}$ is the rate at which a CR proton loses energy to ionisation. β_0 is the cutoff below which the interaction between CRs and the gas decreases sharply; we use $\beta_0 = 0.01$, appropriate for CRs travelling through a neutral IGM (Stacy & Bromm, 2007). As $D_p(n, \epsilon)$ is the mean free path of CRs of energy ϵ travelling through a gas with number density n , we may define an effective cross-section $\sigma_{CR}(n, \epsilon)$ for the interaction

$$\sigma_{CR}(n, \epsilon) = \frac{1}{n D_p(n, \epsilon)}. \quad (4.11)$$

As the CR penetration depth is \gg than the box size everywhere except approaching the centre of the star-forming minihalo, we may estimate the column density N —and thus, the CR attenuation along a given line of sight—using the same technique described in Hummel et al. (2015). The gas column density approaching the centre of the accretion disk varies by roughly an order of magnitude between the polar (N_{pole}) and equatorial ($N_{equator}$) directions, with the column density along these lines of sight well fit by

$$\log_{10}(N_{pole}) = 0.5323 \log_{10}(n) + 19.64 \quad (4.12)$$

and

$$\log_{10}(N_{equator}) = 0.6262 \log_{10}(n) + 19.57, \quad (4.13)$$

respectively. We assume every line of sight within 45 degrees of the pole experiences column density N_{pole} while every other line of sight experiences $N_{equator}$ (Hosokawa et al., 2011), allowing us to calculate an effective optical depth such that

$$e^{-\tau_{CR}} = \frac{2\Omega_{pole}}{4\pi} e^{-\sigma_{CR}N_{pole}} + \frac{4\pi - 2\Omega_{pole}}{4\pi} e^{-\sigma_{CR}N_{eq}}, \quad (4.14)$$

where

$$\Omega_{pole} = \int_0^{2\pi} d\phi \int_0^{\pi/4} \sin\theta d\theta = 1.84 \text{ sr}. \quad (4.15)$$

Accounting for this attenuation of the CR background and following the treatment of Stacy & Bromm (2007) and Inayoshi & Omukai (2011), the cosmic ray heating rate Γ_{CR} and ionisation rate k_{CR} are given by

$$\Gamma_{CR} = \frac{E_{heat}}{50 \text{ eV}} \int_{\epsilon_{min}}^{\epsilon_{max}} \left| \left(\frac{d\epsilon}{dt} \right)_{ion} \right| \frac{dn_{CR}}{d\epsilon} e^{-\tau_{CR}} d\epsilon, \quad (4.16)$$

and

$$k_{CR} = \frac{\Gamma_{CR}}{n_H E_{heat}}, \quad (4.17)$$

where $\epsilon_{min} = 10^6 \text{ eV}$, $\epsilon_{max} = 10^{15} \text{ eV}$, n_H is the number density of hydrogen, and E_{heat} is the energy deposited as heat per interaction (Schlickeiser, 2002). While CRs lose about 50 eV per interaction, only about 6 eV of that goes towards heating in a neutral medium (Spitzer & Scott, 1969; Shull & van Steenberg, 1985); we set E_{heat} accordingly.

Here we assume the incident CR background is composed solely of protons, and all interactions occur with hydrogen only. While this neglects the slight difference in average CR energy loss per interaction for hydrogen (36 eV; Bakker & Segrè 1951) as compared to helium (40 eV; Weiss & Bernstein 1956), the resulting error in the employed heating and ionisation rates is sufficiently small for our purposes (see Jasche et al. 2007 for a more rigorous treatment).

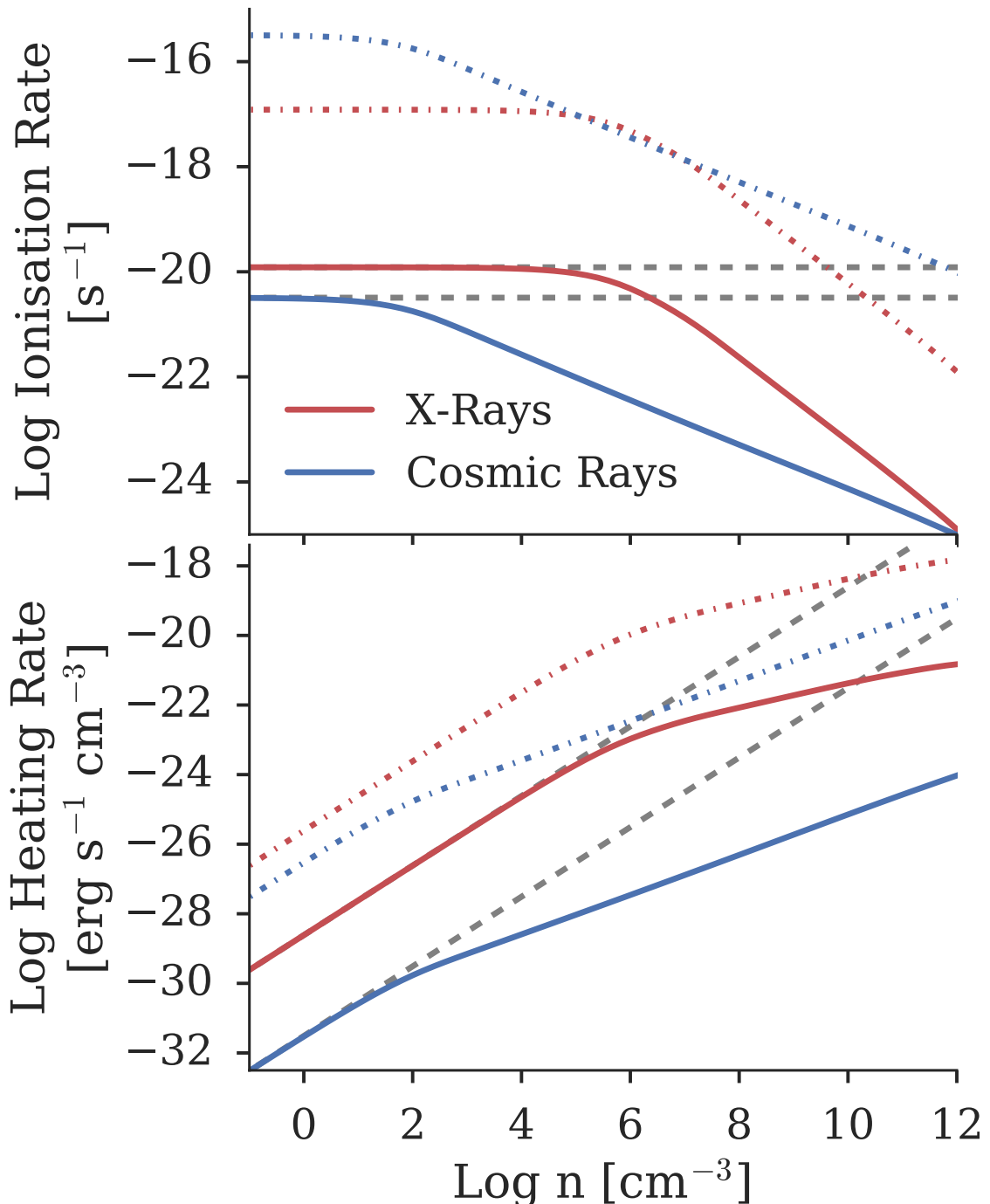


Figure 4.2: Ionisation and heating rates as a function of total gas number density for both a cosmic ray and an X-ray background at $z = 25$. In both panels, the solid blue lines denote the rate for our fiducial CR background, u_0 . The solid red lines show the fiducial X-ray rates from Hummel et al. (2015), while the dashed grey lines demonstrate the expected rates in the absence of gas self-shielding. The dash-dotted blue (red) lines mark the highest-intensity CR (X-ray) heating and ionisation rates investigated. For a given energy density, CRs are more effective at ionising and heating the gas; vertical placement on this chart is simply a matter of normalisation, stemming from the assumptions outlined in Section 4.2. Note that X-rays cause significantly more heating per ionisation event than CRs, but are strongly attenuated at high densities. CRs are significantly more penetrative in comparison.

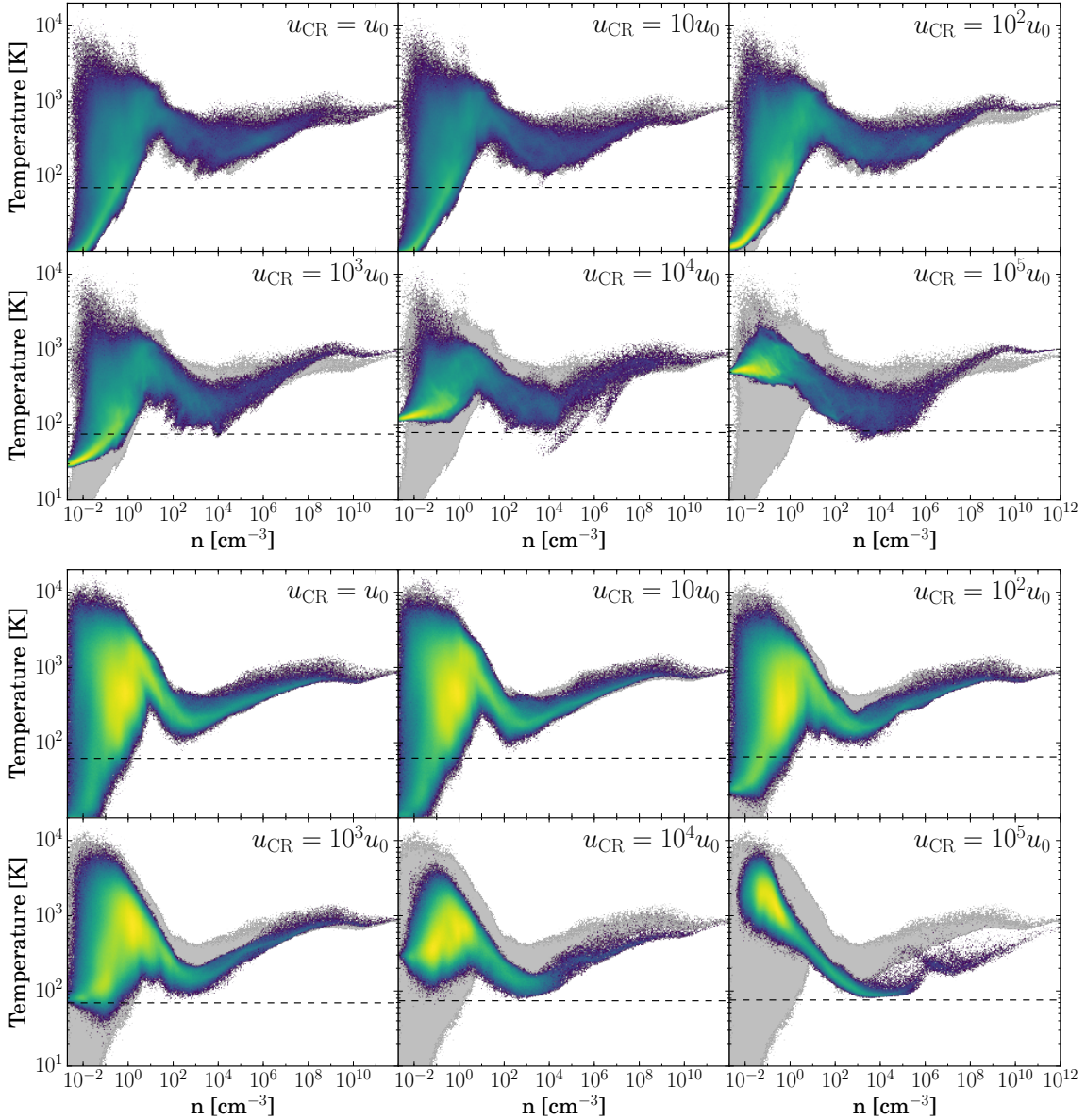


Figure 4.3: Mass-weighted temperature-density distribution of the gas collapsing into Halo 1 (top) and Halo 2 (bottom), shown just prior to sink formation. Each panel shows the behaviour of gas collapsing under a CR background of a given strength. In each case, the behaviour of the gas in the $u_{\text{CR}} = 0$ case is reproduced for comparison (light grey); dashed lines denote the CMB temperature when collapse occurs. Gas at low densities gets progressively hotter and gas in the loitering phase gets progressively cooler with increasing u_{CR} . Note that the gas invariably proceeds to collapse, and converges toward a similar thermodynamic path as it approaches sink formation densities, regardless of the CR background strength.

The resulting heating and ionisation rates for both the $u_{\text{CR}} = u_0$ and $10^5 u_0$ cases are shown in Figure 4.2, along with the expected rates in the absence of attenuation. Also shown are the highest and lowest X-ray heating and ionisation rates considered in Hummel et al. (2015). Compared to X-rays, CRs produce significantly less heating per ionisation event and penetrate to much higher densities before being attenuated; the X-ray heating and ionisation rates fall off much faster as the gas becomes optically thick.

4.3.4 Sink Particles

Our sink particle method is described in Stacy et al. (2010). When a gas particle exceeds $n_{\text{max}} = 10^{12} \text{ cm}^{-3}$, it and all non-rotationally-supported particles within the accretion radius r_{acc} are replaced by a single sink particle. We set r_{acc} equal to the resolution length of the simulation: $r_{\text{acc}} = L_{\text{res}} \simeq 50 \text{ AU}$, where

$$L_{\text{res}} \simeq 0.5 \left(\frac{M_{\text{res}}}{\rho_{\text{max}}} \right)^{1/3}, \quad (4.18)$$

and $\rho_{\text{max}} = n_{\text{max}} m_{\text{H}}$. Upon creation, the sink immediately accretes the majority of the particles within its smoothing kernel, resulting in an initial mass for the sink particle M_{sink} close to $M_{\text{res}} \simeq 1 M_{\odot}$. Following its creation, the density, temperature, and chemical abundances of the sink particle are no longer updated. The sink's density and temperature are held constant at 10^{12} cm^{-3} and 650 K, respectively; the pressure of the sink is set accordingly. Assigning a temperature and pressure to the sink particle allows it to behave as an SPH particle, thus avoiding the creation of an unphysical pressure vacuum which would artificially enhance the accretion rate onto the sink (see Bromm et al., 2002; Martel et al., 2006). Once the sink is formed, additional particles (including smaller sinks) are accreted as they approach within

r_{acc} of that sink particle, and the position and momentum of the sink particle is set to the mass-weighted average of the pre-existing sink and the accreted particle.

4.4 Results

4.4.1 Initial Collapse

4.4.1.1 CR-enhanced H₂ Cooling

The gas in both Halo 1 and Halo 2 invariably collapses to high densities, even as we vary the CR background strength by five orders of magnitude. As seen in Figure 4.3, the collapse occurs in accordance with the standard picture of Pop III star formation (e.g., Greif et al., 2012; Stacy & Bromm, 2013; Hirano et al., 2014; Hosokawa et al., 2015), albeit slightly modified by the presence of a CR background. In each case, the gas heats adiabatically as it collapses until reaching $\sim 10^3$ K, at which point H₂ cooling is activated. This allows the gas to cool to ~ 200 K, whereupon it enters a ‘loitering’ phase (Bromm et al., 2002), increasing in density quasi-hydrostatically until sufficient mass accumulates to trigger the Jeans instability, typically between 10^4 cm^{-3} and 10^6 cm^{-3} . Runaway collapse then proceeds until three-body reactions become important at $n \sim 10^8 \text{ cm}^{-3}$; this turns the gas fully molecular by $n \sim 10^{12} \text{ cm}^{-3}$, at which point we insert sink particles.

As demonstrated in Figure 4.4, increasing u_{CR} both heats the gas and boosts the resulting ionisation fraction. This in turn increases the efficiency of H₂ formation, enhancing cooling and allowing gas in the loitering phase to reach progressively lower temperatures. In fact, the additional cooling is sufficient to cool the gas all the way to the CMB floor when $u_{\text{CR}} \gtrsim 10^4 u_0$. However as the gas exits the loitering

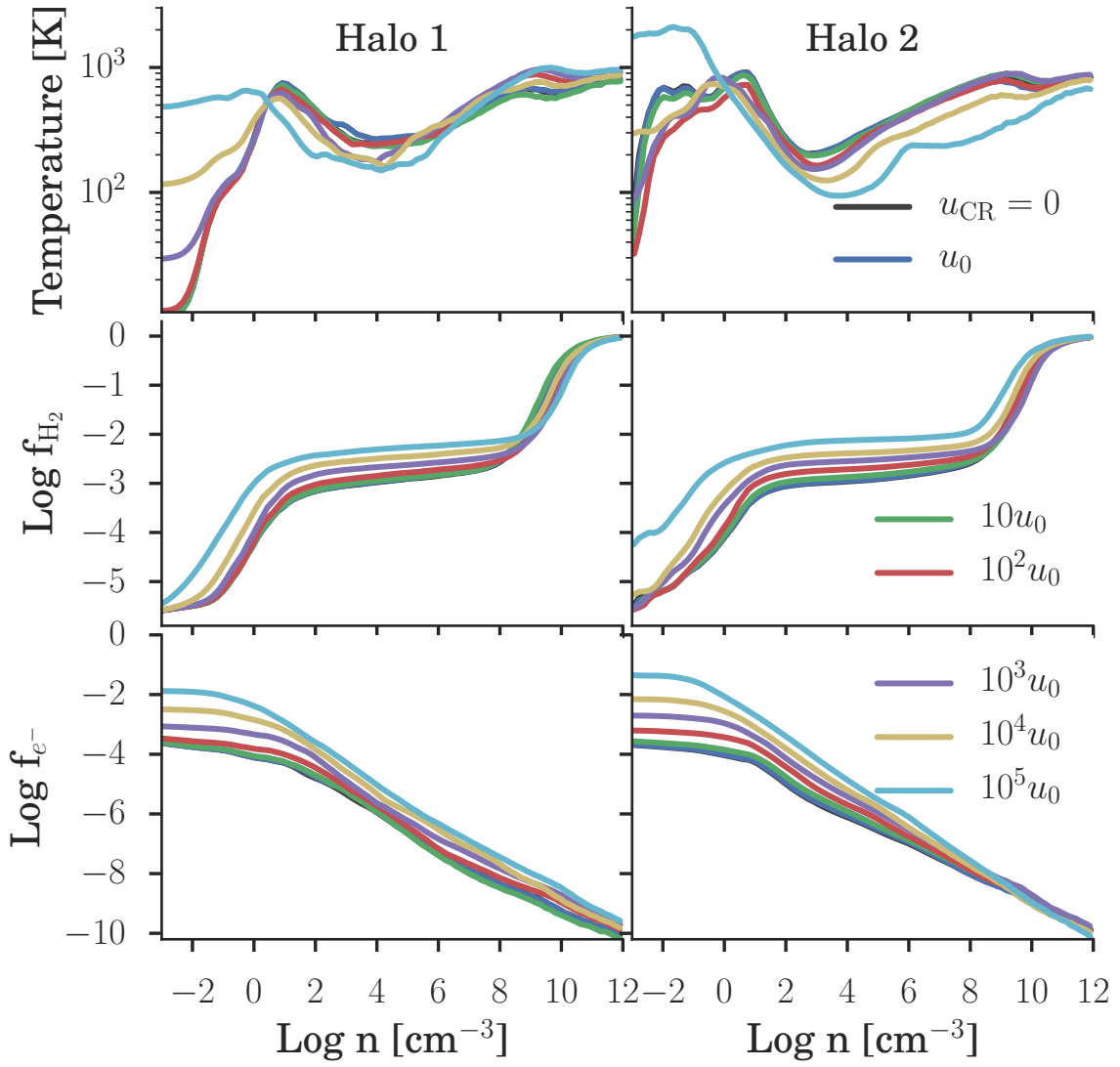


Figure 4.4: From top to bottom, density-binned average gas temperature, H_2 fraction, and free electron fraction for both Halo 1 (left) and Halo 2 (right). As u_{CR} increases, the additional ionisation increases f_{e^-} , which in turn elevates f_{H_2} . Combined with the additional heating provided by the CR background, this allows H_2 cooling to activate at slightly lower densities and gas in the loitering phase to reach slightly lower temperatures, as seen in the top panel.

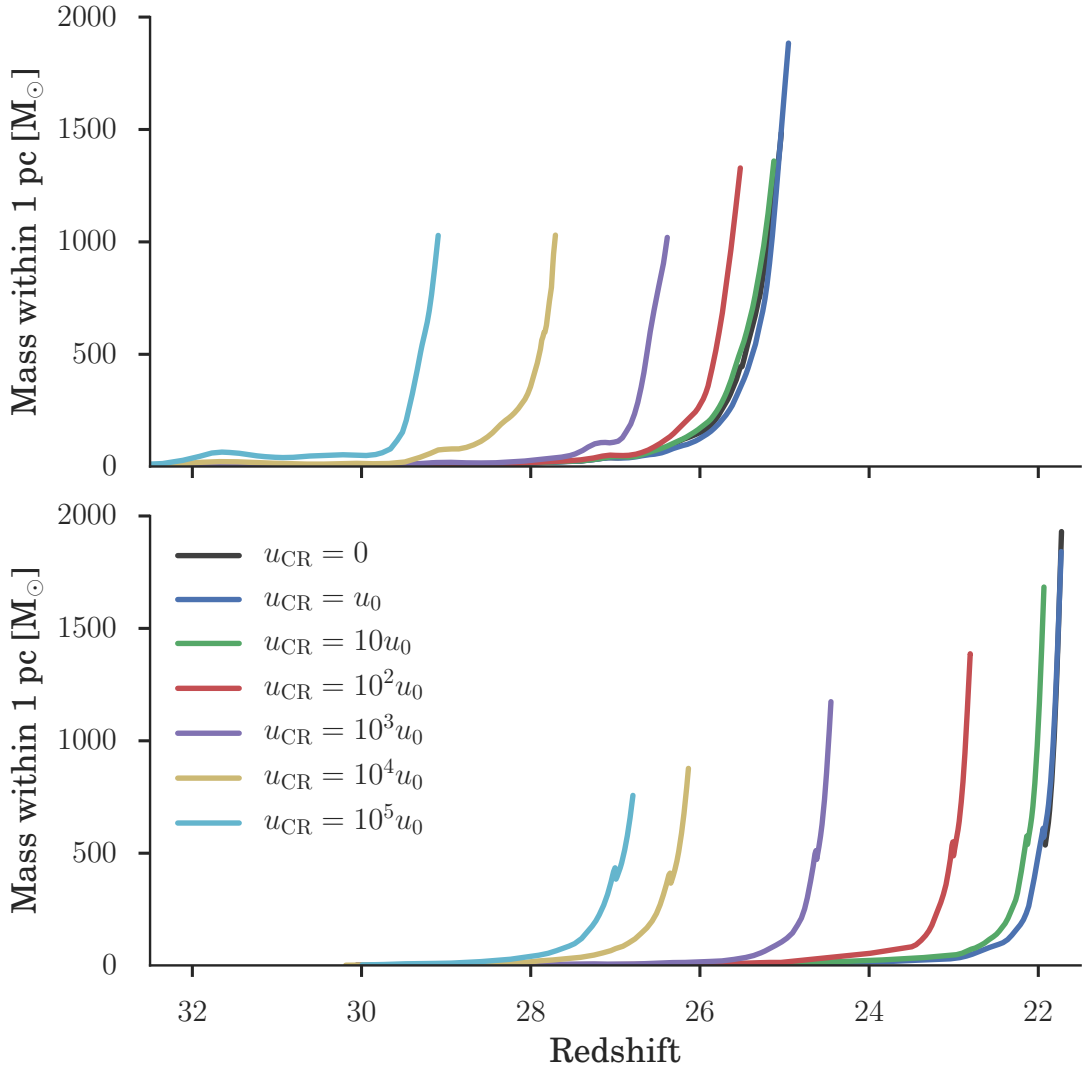


Figure 4.5: Total gas mass within 1 pc of the highest density point in each simulation over cosmic time. Top: Halo 1; bottom: Halo 2. As u_{CR} increases, the additional heating and ionisation allows the gas to fulfil the Rees-Ostriker criterion ($t_{\text{cool}} \lesssim t_{\text{ff}}$) sooner, expediting collapse to high densities. The sooner runaway collapse sets in, the less time gas has to accumulate in the centre of the minihalo, resulting in a lower total mass within 1 pc at simulation's end. The discontinuity seen in the growth of Halo 2 is a numerical artefact arising from the cut-out and refinement process.

phase and proceeds to higher densities, the CR optical depth increases significantly. In concert with the onset of three-body processes this renders CR ionisation and heating ineffective at high densities. As a result, the thermal behaviour of the gas increasingly resembles that seen in the $u_{\text{CR}} = 0$ case as the collapse proceeds. To wit, by the time we form sink particles at 10^{12} cm^{-3} the thermodynamic state of the gas is remarkably similar, even as we vary the CR background strength by five orders of magnitude. This convergence under a wide range of environmental conditions is similar to that seen in the presence of both an X-ray background (Hummel et al., 2015) and DM–baryon streaming (Stacy et al., 2011a; Greif et al., 2011b).

4.4.1.2 Expedited Collapse

Boosting the H₂ fraction in the gas lowers the density threshold for efficient cooling, allowing the gas to fulfil the Rees-Ostriker criterion sooner by driving the cooling time t_{cool} below the freefall time t_{ff} (Rees & Ostriker, 1977). This is demonstrated in Figure 4.4, where we see the density at which the gas begins to cool drop as the CR background strength increases. This necessarily expedites the subsequent phases of the collapse, as seen clearly in Figure 4.5, where we show the total gas mass within 1 pc (physical) of the minihalo’s centre as a function of redshift. The impact this has on the environment in which the minihalo collapses is seen in Figure 4.6, where we show the final simulation output on various scales for Halo 1 and Halo 2, both in the absence of any CR background ($u_{\text{CR}} = 0$) and with $u_{\text{CR}} = 10^5 u_0$. Low density filamentary gas is heated and prevented from collapsing, reducing the clumping of the IGM and possibly impacting the early stages of reionisation. Gas above a u_{CR} -dependent density threshold on the other hand experiences enhanced cooling and thus has its collapse expedited. As a result, the dynamical environment in which

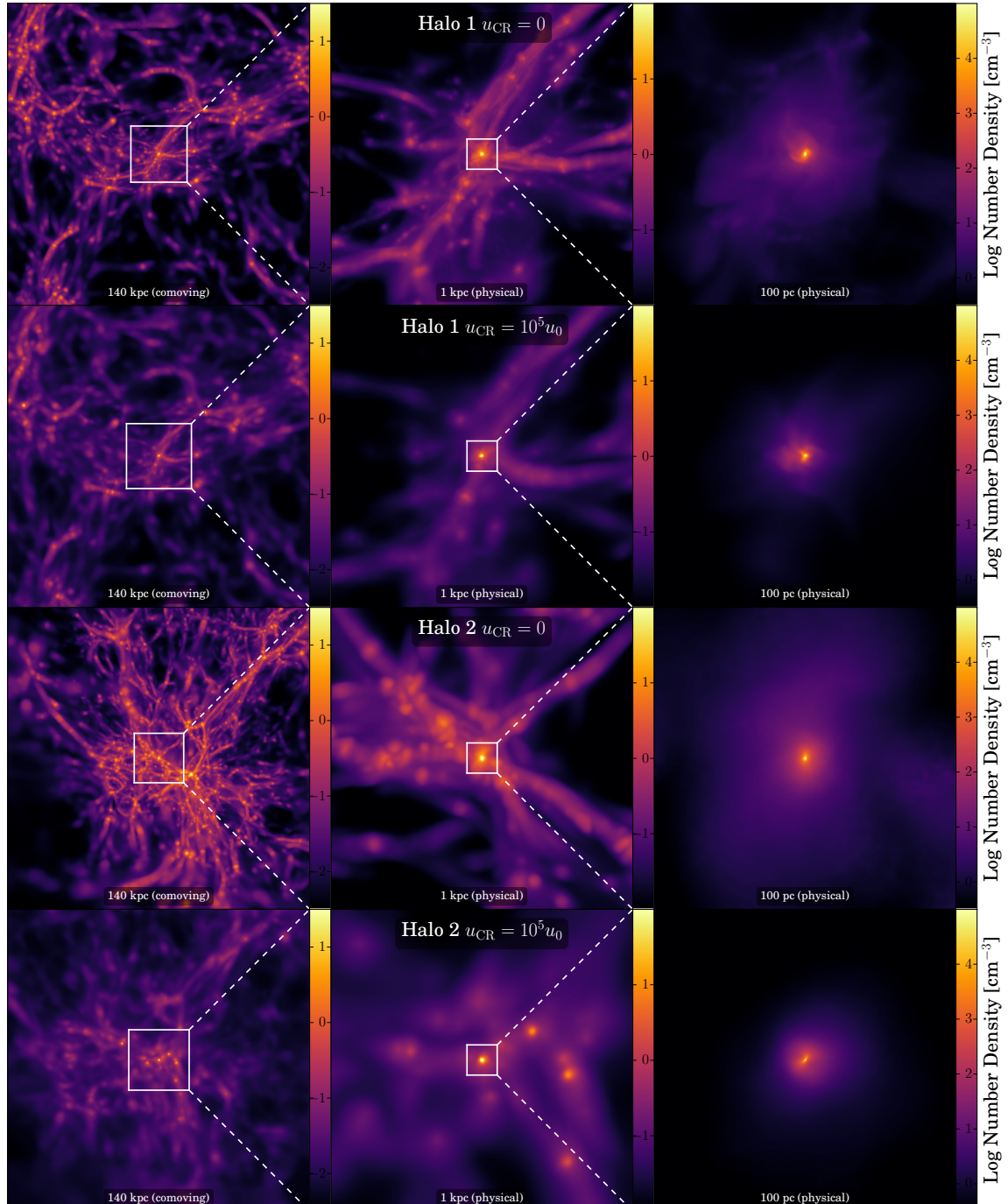


Figure 4.6: Simulation structure for both Halo 1 (top) and Halo 2 (bottom) as seen in the final output, 5000 yr after the first sink forms. Shown is a density projection of the minihalo environment on progressively smaller scales for both the $u_{\text{CR}} = 0$ and $u_{\text{CR}} = 10^5 u_0$ simulations, as labelled. White boxes indicate the region depicted on the next smaller scale. From left to right: filamentary structure of the cosmic web near the minihalo formation site; minihalo formation at the intersection of several filaments; morphology within the ~ 100 pc virial radius of the minihalo. The density scale for each level is shown just to the right – note that the scaling changes from panel to panel. Note how the gas in the $u_{\text{CR}} = 10^5 u_0$ simulations appears smoothed out compared to the $u_{\text{CR}} = 0$ simulations. Not only do CRs heat and smooth the filamentary gas, the expedited collapse induced by CR ionisation leaves less time for low-density structure to form, since the collapse is shifted to an earlier epoch. As a

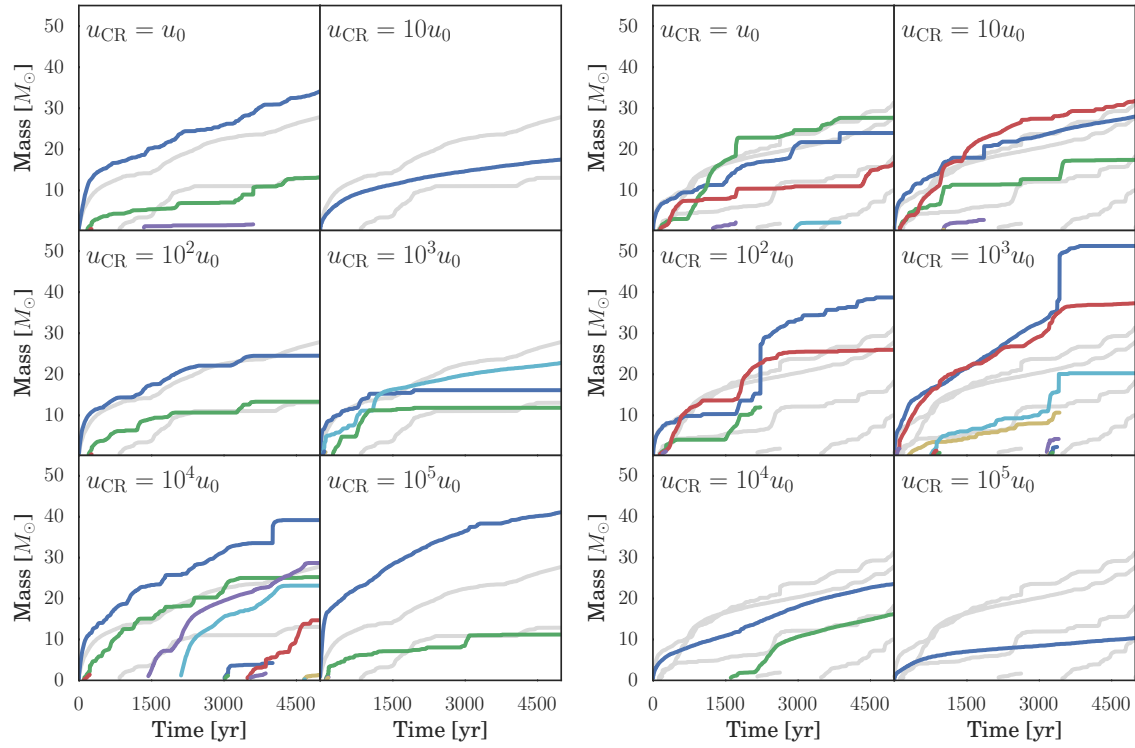


Figure 4.7: Growth of individual sink particles in each simulation over time, with the first sink forming at $t = 0$. Lines end where one sink is accreted by another. The Halo 1 suite of simulations is shown in the left panel, Halo 2 in the right panel. The growth of the sinks in the corresponding $u_{\text{CR}} = 0$ is shown in grey in the background of each panel for comparison. There are no apparent trends with increasing u_{CR} – neither in typical sink mass nor in the number of fragments formed.

the first sink particles form varies significantly depending on the strength of the CR background.

4.4.2 Star Formation

4.4.2.1 Protostellar Fragmentation and Growth

Figure 4.7 shows the growth over time of all sink particles formed in our simulations, from formation of the first sink particle to simulation’s end 5000 yr later when radiative feedback can no longer be ignored. The first sink particle forms when the gas in

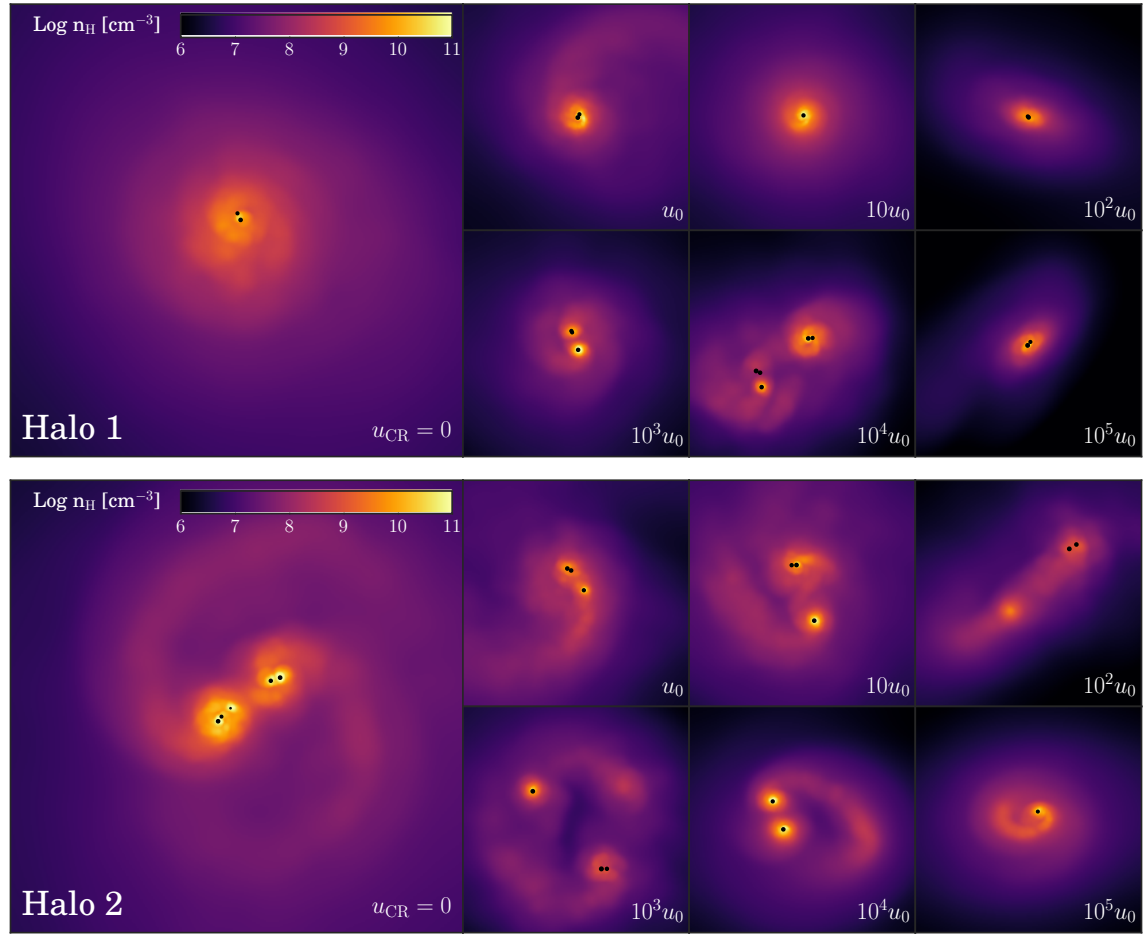


Figure 4.8: Density projection of the central 20 000 AU of each simulation 5000 yr after the formation of the first sink particle. Upper panel: Halo 1; lower panel: Halo 2. Each accretion disc is shown face-on; sink particle positions are identified by black dots whose size scales logarithmically with the mass of the sink. In each panel the accretion disk formed in the absence of any CR background is shown on the left; the corresponding u_{CR} -modified discs are shown to the right. Note the broad variation in both disc structure and spatial extent.

the centre of the minihalo reaches densities of 10^{12} cm^{-3} , and develops an accretion disk within a few hundred years. In all but three cases, this disk quickly fragments, forming a binary or small multiple within 500 yr. Sinks that survive longer than a few hundred years without undergoing a merger quickly accrete the surrounding gas, growing to \sim a few solar masses within 500 yr and typically reaching between 10 and $40 M_{\odot}$ by simulation’s end.

As is evident from Figure 4.7, there is no clear trend with u_{CR} in either protostellar growth or accretion rate, nor is there any trend in the total sink mass. For example, both the $10 u_0$ Halo 1 simulation and $10^5 u_0$ Halo 2 simulation form only a single sink while the $10^3 u_0$ Halo 2 simulation steadily forms a total of 14 sink particles over the 5000 yr period. This can be primarily attributed to the wide variety of dynamical environments in which the sink particles form—demonstrated in Figure 4.8, where we show the accretion disk structure of each simulation 5000 yr after the first sink formed. This variation is a direct consequence of the expedited collapse discussed in Section 4.4.1.2. As seen in Figure 4.6, expediting the initial collapse results in significant variation of the experienced gravitational potential; the collapse history of the gas and the dynamical environment in which the sinks form varies accordingly. Given the lack of any apparent trends with increasing u_{CR} , this suggests the final stages of the collapse are influenced more by small-scale turbulence than the strength of the CR background. While CRs may indeed alter the susceptibility of the disk to fragmentation, any such behaviour is masked by variations in the collapse history between simulations.

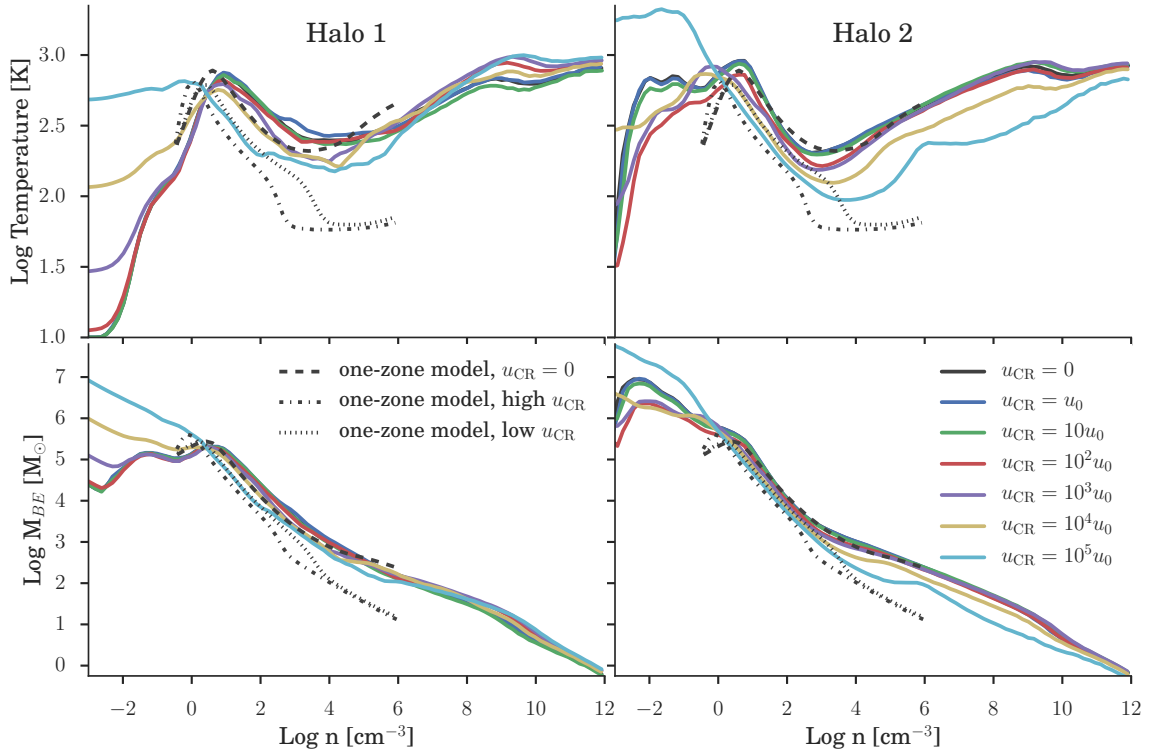


Figure 4.9: Density-binned average temperature (top) and Bonnor-Ebert mass (bottom) for Halo 1 (left) and Halo 2 (right) for all CR background strengths, as labelled. Overlaid on each panel are the one-zone calculations of Stacy & Bromm (2007), which only tracked the gas evolution up to densities of 10^6 cm^{-3} , insufficient to observe the u_{CR} -independent convergence in the thermodynamic state of the gas as it proceeds to runaway collapse.

4.4.2.2 Characteristic Mass

While the final stages of the collapse appear to be somewhat chaotic, with protostellar fragmentation driven primarily by small-scale turbulence rather than the CR background, the typical mass of the sinks formed remains quite stable across all simulations at $10 - 40 \text{ M}_\odot$. This is very much in line with the prevailing consensus for the expected mass of the first stars in the absence of any radiative feedback of \sim a few $\times 10 \text{ M}_\odot$ (Bromm, 2013). As noted in Section 4.4.1.1, the thermodynamic behaviour of the gas displays a remarkable similarity as it approaches sink formation densities,

regardless of u_{CR} . This suggests that the influence of the CR background is restricted to lower densities, with little to no effect on the protostellar cores from which the first stars ultimately form.

The universality of this characteristic mass is further supported by Figure 4.9, where we show the average gas temperature as a function of number density, as well as the approximate fragmentation mass scale, as estimated by the Bonnor-Ebert mass (e.g., Stacy & Bromm, 2007):

$$M_{BE} = 700 \text{ M}_\odot \left(\frac{T}{200 \text{ K}} \right)^{3/2} \left(\frac{n}{10^4 \text{ cm}^{-3}} \right)^{-1/2}, \quad (4.19)$$

where n and T are the number density and corresponding average temperature. Approaching sink formation densities M_{BE} is nearly independent of u_{CR} , in agreement with the observed lack of evolution in the sink mass.

Also shown in Figure 4.9 are the one-zone calculations from Stacy & Bromm (2007). Investigating the impact of a CR background on Pop III star formation in a $z = 21$ minihalo using the CR background strengths shown in Figure 4.1, their models suggested that a sufficiently strong background might decrease the fragmentation mass scale by an order of magnitude as a result of the cooler temperatures experienced during the loitering phase. While we observe similar behaviour from gas in the loitering phase, once the gas proceeds to runaway collapse its thermodynamic state quickly converges with that of the $u_{\text{CR}} = 0$ case, such that the fragmentation mass scale remains unaltered. Unfortunately the models of Stacy & Bromm (2007) only followed the gas evolution up to densities of 10^6 cm^{-3} , insufficient to observe this convergent behaviour.

4.5 Summary and Conclusions

We have performed two suites of cosmological simulations employing a range of CR backgrounds spanning five orders of magnitude in energy density. We follow the thermodynamic evolution of the gas as it collapses into a minihalo from IGM densities up to $n = 10^{12} \text{ cm}^{-3}$, at which point three-body processes have turned the gas fully molecular. This allows us to capture the combined impact of CR heating and ionisation on Pop III stars forming in the minihalo via its influence on H₂ and HD cooling. Once the gas reaches $n = 10^{12} \text{ cm}^{-3}$, we form sink particles and follow the subsequent evolution of the system for 5000 yr, after which point radiative feedback from the forming protostars can no longer be ignored, and our simulations are terminated.

While it also serves to heat the gas, the primary impact of the CR background is to increase the number of free electrons in the collapsing gas, catalysing the formation of additional molecular hydrogen, which in turn enhances the H₂ cooling efficiency. This decreases the cooling time, allowing the gas to fulfil the Rees-Ostriker criterion sooner and expediting minihalo collapse. Each simulation therefore collapses to high density at a different epoch, and the resulting variation in experienced gravitational potential causes the collapse history—and thus the accretion disk structure—to differ greatly between simulations.

Our first suite of simulations (Halo 1) used the same initial conditions as our prior investigation of a cosmic X-ray background (Hummel et al., 2015), allowing for a direct comparison of the results. CRs are much less efficient than X-rays at heating the gas, such that the collapse suppression observed for a sufficiently strong X-ray background does not occur here. While expedited collapse is observed in the presence of an X-ray background as well, the effect is somewhat more pronounced here owing

to the more efficient nature of CR ionisation, as there is less associated heating to partially counteract the enhanced cooling.

Our second suite of simulations focused on a minihalo collapsing at $z \simeq 21.5$ in the $u_{\text{CR}} = 0$ case in order to allow a more direct comparison to the results of Stacy & Bromm (2007), and control for the influence of the CMB temperature floor on our results. While we find similar evidence for a lower gas temperature in the loitering phase, extending our study beyond the $n = 10^6 \text{ cm}^{-3}$ limit of Stacy & Bromm (2007) revealed that the thermodynamic path of the collapsing gas—and thus, the fragmentation mass scale—begins to converge with that of the $u_{\text{CR}} = 0$ case for $n \gtrsim 10^6 \text{ cm}^{-3}$. This convergence is observed in all simulations for both Halo 1 and Halo 2, with the thermodynamic state of the gas becoming nearly independent of u_{CR} by the time we form sink particles at $n = 10^{12} \text{ cm}^{-3}$. The remarkable similarity in the thermodynamic state of the gas just prior to sink formation suggests the presence of a CR background has little impact on the characteristic mass of the stars formed. Indeed, the typical mass of the sink particles formed is quite robust, remaining stable across all simulations at $10 - 40 M_{\odot}$, very much in line with the expected mass of the first stars in the absence of external radiative feedback. In fact, this robust behaviour is observed under a variety of environmental conditions, including X-ray irradiation (Hummel et al., 2015) and DM–baryon streaming (Stacy et al., 2011a; Greif et al., 2011b).

While the neutral impact of the CR background on the thermodynamic state of primordial gas at high densities results in a robust characteristic mass that does not vary with u_{CR} , there is a possibility that the enhanced cooling resulting from CR ionisation may decrease the velocity dispersion of the infalling gas (Clark et al., 2011a).

This would decrease fragmentation in the centre of the minihalo, possibly increasing the mass of the stars formed. While we see no evidence to support this, any such systematic effect could be easily masked by the variations in collapse history between simulations. Likewise, the fact that each simulation collapses to high densities at a different epoch in a different gravitational potential well limits our ability to draw detailed conclusions regarding the impact of the CR background on fragmentation in the protostellar accretion disc.

Finally, while the characteristic mass—and thus, ionising output—of Pop III stars appears to be unaffected by the presence of a CR background, CRs still heat the low-density gas in the IGM, reducing its clumping factor. This may have implications for reionisation and the 21-cm signal (Furlanetto et al., 2006; Sazonov & Sunyaev, 2015).

Chapter Five: A pandas-based Framework for Analyzing GADGET Simulation Data

5.1 Introduction

In the past decade, astrophysical simulations have increased dramatically in both scale and sophistication, and the typical size of the datasets produced has grown accordingly. However, the software tools for analyzing such datasets have not kept pace, such that one of the primary barriers to exploratory investigation is simply manipulating the data. This problem is particularly acute for users of the popular smoothed particle hydrodynamics (SPH) code GADGET (Springel et al., 2001b; Springel, 2005). Both GADGET and GIZMO (Hopkins, 2015), which uses the same data storage format, are widely used to investigate a range of astrophysical problems; unfortunately this also leads to fractionation of the data storage format as each research group modifies the output to suit its needs. This state of affairs has historically forced significant duplication of effort, with individual research groups separately developing their own unique analysis scripts to perform similar operations.

Fortunately, the issue of data management and analysis is not endemic to astronomy, and the resulting overlap with the needs of the broader scientific community and the industrial community at large provides a large pool of scientific software developers to tackle these common problems. In recent years, this broader community has settled on python as its programming language of choice due to its efficacy as a ‘glue’ language and the rapid speed of development it allows. This has led to the de-

velopment of a robust scientific software ecosystem with packages for numerical data analysis like `numpy` (van der Walt et al., 2011), `scipy` (Jones et al., 2001), `pandas` (McKinney, 2010), and `scikit-image`; `matplotlib` (Hunter, 2007) and `seaborn` for plotting; `scikit-learn` for machine learning, and statistics and modeling packages like `scikits-statsmodels`, `pymc`, and `emcee` (Foreman-Mackey et al., 2013).

Python is quickly becoming the language of choice for astronomers as well, with the Astropy project (Robitaille et al., 2013) and its affiliated packages providing a coordinated set of tools implementing the core astronomy-specific functionality needed by researchers. Additionally, the development of flexible python packages like `yt` (Turk et al., 2011) and `pynbody` (Pontzen et al., 2013), capable of analyzing and visualizing astrophysical simulation data from several different simulation codes, have greatly improved the ability of computational researchers to perform useful, insight-generating analysis of their datasets.

Recently, the scientific python community has begun to converge on the `DataFrame` provided by the high-performance `pandas` data analysis library as a common data structure. As a result, once data is loaded into a `DataFrame`, it becomes much easier to take advantage of the powerful analysis tools provided by the broader scientific computing ecosystem. With this in mind, we present a `pandas`-based framework for analyzing GADGET simulation data, `GADFLY`: the GADGET DataFrame LibrarY.

In this paper we present the first public release (v0.1) of `gadfly`, which is available at <http://github.com/hummel/gadfly>. The framework design and organizational structure are outlined in Section 5.2, followed by a description of the included SPH particle rendering in Section 5.3. Our plans for future development are outlined in Section 5.4, and a summary is provided in Section 5.5.

```

Importing gadfly and initializing the simulation:
>>> import gadfly as gdf
>>> sim = gdf.Simulation('path_to_simulation_directory')

Loading a snapshot:
>>> snap = sim.load_snapshot(100)
>>> snap.file_id
<HDF5 file "snapshot_100.hdf5" (mode r)>
>>> snap.file_id.keys()
[u'Header', u'PartType0', u'PartType1']

Inspecting the Header:
>>> snap.header.Redshift
26.663827788885538
>>> snap.header.BoxSize
100.0

Loading a particle dataset:
>>> snap.define_ptype('dm', 1, gdf.nbody.PartTypeNbody)
>>> snap.dm.load_masses()
>>> snap.dm.info()
<class 'gadfly.nbody.PartTypeNbody'>
Int64Index: 13347573 entries, 25272898 to 25272897
Data columns (total 1 columns):
masses      float64
dtypes: float64(1)
memory usage: 203.7 MB

>>> snap.dm.cleanup()
>>> snap.dm.load_quantity('coordinates', 'particleIDs')
>>> snap.dm.info()
<class 'gadfly.nbody.PartTypeNbody'>
Int64Index: 13347573 entries, 25272898 to 25272897
Data columns (total 4 columns):
x          float64
y          float64
z          float64
particleIDs  uint32
dtypes: float64(3), uint32(1)
memory usage: 458.3 MB

```

Figure 5.1: Initializing a simulation, defining a PartType dataset, and loading data.

5.2 A Framework built on pandas

There are several motivations for building an analysis framework around the `pandas DataFrame`. The guiding principle underlying the design of this framework is to enable exploratory investigation. This requires both intelligent memory management for handling out-of-core datasets, and a robust indexing system to ensure that particle properties do not become misaligned in memory. Using the `pandas DataFrame` as the primary data container rather than separate `numpy` arrays makes it much easier to keep different particle properties indexed correctly while still affording the flexibility to load and remove data from memory at will. In addition, `pandas` itself is a thoroughly documented, open-source, BSD-licensed library providing high-performance, easy-to-use data structures and analysis tools, and has a strong community of developers working to improve it. More broadly, as `pandas` is becoming the de-facto standard for data analysis in python, doing so simplifies interoperability with the rest of the available tools.

`Gadfly` is designed for use with simulation data stored in the HDF5 format¹. While we otherwise aim to keep `gadfly` as general as possible, some assumptions about the storage format are necessary. Each particle type is expected to be contained in a different HDF5 group, labeled `PartType0`, `PartType1`, etc; a `Header` group is also expected, containing metadata for the simulation snapshot as HDF5 attributes. All particles are expected to have the following fields defined: particle IDs, masses, coordinates, and velocities. SPH particles are additionally expected to have a smoothing length, density, and internal energy. Additional fields not included in the original GADGET specification, such as chemical abundances, are also supported.

¹<http://www.hdfgroup.org/HDF5>

Here, we provide an overview of the design and capabilities of the `gadfly` framework, including the `Simulation`, `Snapshot`, and `PartType DataFrame` objects at the core of `gadfly` (Section 5.2.1), the usage of which is demonstrated in Figure 5.1. Our approach to file access and intelligent memory management (Section 5.2.2), our handling of unit conversions (Section 5.2.3) and coordinate transformations (Section 5.2.4), and the included utilities for parallel batch processing (Section 5.2.5) are also described.

5.2.1 Organizational Structure

5.2.1.1 PartType Dataframes

Data for each particle type (e.g., dark matter, gas, etc.) is stored in a separate `PartType` dataframe and indexed by particle ID number. Individual fields can be loaded into the dataframes and deleted at will, with coherent slicing across multiple data fields, courtesy of `pandas`. The base `PartType` objects, `PartTypeNbody` and `PartTypeSPH`, are standard `pandas` dataframes with additional functionality for loading standard GADGET particle fields from HDF5, converting units, and performing coordinate transformations. As such, `PartType` dataframes retain all the capabilities of the `pandas.DataFrame` from which they inherit, and any operation that creates a new dataframe instance returns a standard `pandas` dataframe.

Nonstandard particle fields (e.g., chemical abundances) can be easily loaded into `gadfly` as well; fields loaded in this manner simply lack automated unit conversion. Alternatively, a custom dataframe class inheriting from `PartTypeNbody` or `PartTypeSPH` as appropriate can be defined to provide methods for loading both non-standard particle fields and additional derived properties (e.g., temperature). An

```
Loading a non-standard particle field:  
>>> snap.define_ptype('gas', 0, gdf.sph.PartTypeSPH)  
>>> snap.gas.load_quantity('Adiabatic index')  
>>> snap.gas.info()  
<class 'gadfly.sph.PartTypeSPH'>  
Int64Index: 13347573 entries, 23325038 to 23308525  
Data columns (total 1 columns):  
 Adiabatic index    float64  
 dtypes: float64(1)  
 memory usage: 203.7 MB
```

```
Loading a dataset using a custom class:  
>>> from custom_ptype import PartTypeCustom  
>>> snap.define_ptype('gas', 0, PartTypeCustom)  
>>> snap.gas.calculate_temperature()  
>>> snap.gas.info()  
<class 'custom_ptype.PartTypeCustom'>  
Int64Index: 13347573 entries, 23325038 to 23308525  
Data columns (total 3 columns):  
 adiabatic_index    float64  
 internal_energy    float64  
 temperature        float64  
 dtypes: float64(3)  
 memory usage: 407.3 MB
```

Figure 5.2: Loading non-standard particle fields and defining custom PartType classes. Within `gadfly` this is straightforward.

example of such a custom class—`PartTypeCustom.py`—is provided in the examples distributed with `gadfly`, and the usage of such a custom class is demonstrated in Figure 5.2.

5.2.1.2 Snapshot

Each `Snapshot` object represents a single HDF5 snapshot file on disk. File access—provided by `h5py` (Collette, 2008)—is handled via the `Snapshot` object, and the actual particle data, loaded as needed into the `PartType` dataframes described in Section 5.2.1.1, is gathered here with each particle type contained in a separate `PartType` dataframe. The information contained in the GADGET header is also maintained here in a `Header` object, along with access to the additional metadata and unit information stored in the relevant `Simulation` object.

5.2.1.3 Simulation

Metadata relevant to the simulation as a whole, such as filepaths and unit information, are stored in a `Simulation` object. Initializing a `Simulation` object is the first step in any analysis using `gadfly` as this is where default values for all subsequent analysis are set, including locating all relevant snapshot files, choosing a coordinate system, and setting the field names of the default particle properties expected by `gadfly`. Snapshots are loaded via `Simulation.load_snapshot()`, and the parallel batch processing functionality described in Section 5.2.5 is implemented at this level as well.

5.2.2 Memory Management and File Access

One of the primary goals of the `gadfly` project is to enable the analysis of large datasets on machines with limited memory. Enabling this requires intelligent memory management, loading only the particle data of interest from the disk. Fortunately the HDF5 protocol is well-suited to such non-contiguous file access, allowing not only individual data fields to be accessed independently, but also for loading only select entries from the field in question.

`Gadfly` employs two complementary approaches to minimizing the memory footprint. The first method requires definition of an optional refinement criterion, such as particles above a given density threshold. The resulting ‘refined’ index can then be used to select only the corresponding values from subsequent particle fields as they are loaded. While this method efficiently minimizes I/O operations, it is fairly rigid, and attempting to load additional fields into a dataframe from which particles have been manually dropped will fail, as the particle indices will no longer match. As such, this approach is poorly suited to exploratory analysis where the proper refinement criterion may not be known *a priori* and is best suited for use in scripts where the analysis to be performed is well defined.

To mitigate the indexing issues that can arise in situations where data is loaded incrementally, `gadfly` performs an intermediate step, first loading new fields into a `pandas.Series` data structure, using the particle ID numbers as an index. This allows `pandas` to properly align the particle fields, dropping any particles not in the existing `PartType` dataframe from the newly loaded field as it is appended. This approach, which can be used in tandem with the refinement index, affords `gadfly` the flexibility needed to allow incremental manual refinement of the data stored in

Table 5.1: Default code units expected by `gadfly`.

Unit	Conversion to <code>cgs</code>
Mass	1.989×10^{43} g
Length	3.085678×10^{21} cm
Velocity	1.0×10^5 cm s $^{-1}$

memory. Additional cuts can be made as subsequent fields are loaded, resulting in the selection of a precisely targeted primary dataset from which derived properties (e.g., temperature) may be calculated, which serves to reduce computational overhead as well.

5.2.3 Units

`Gadfly` implements a minimal unit-handling system for converting between the native code units in which GADGET stores data and the physical units of interest to astronomers. However, GADGET’s code units may be modified to suit the problem at hand, and therefore must be specified at initialization if they differ from the defaults listed in Table 5.1. Conversion from code units to the physical units system of choice is handled at loading. The default units for length, time, mass, etc. can be specified at initialization, along with whether to use physical or comoving coordinates (for cosmological simulations) and whether to factor the Hubble constant out of the reported units (i.e., units of Mpc vs. Mpc/ h). While defaults are set at startup, they can be modified at any time, either by calling `units.set_length()`, which alters the default length unit for all subsequently loaded fields, or by calling a particle field’s load function with the optional `units` keyword argument. Changing the units of an existing field can be done by simply reloading it; the field will remain properly indexed as described in Section 5.2.2. Examples of both approaches to unit conversions are shown in Figure 5.3.

```

Specifying code unit conversions:
>>> import gadfly as gdf
>>> sim = gdf.Simulation('path_to_simulation_directory',
                           UnitMass_in_g = 1.989e43,
                           UnitLength_in_cm = 3.085678e21,
                           UnitVelocity_in_cm_per_s = 1e5)

Specify default units:
>>> sim = gdf.Simulation('path_to_simulation_directory',
                           length='kpc',
                           mass = 'solar',
                           velocity = 'kms',
                           time = 'gyr')

Change default units on the fly:
>>> sim.units.length_unit
'kpc'
>>> sim.units.set_length('AU')
>>> sim.units.length_unit
'AU'

Specify units at load time:
>>> sim.units.mass_unit
'g'
>>> snap.gas.load_masses(unit='solar')
>>> sim.units.mass_unit
'solar'

```

Figure 5.3: Unit handling in `gadfly`.

5.2.4 Coordinate Transformations

A full suite of coordinate transformation utilities is included in `gadfly`, with methods for converting between Cartesian, spherical, and cylindrical coordinates, performing linear coordinate translations, and rotations about arbitrary axes. These methods are both directly accessible as independent library functions, and via the `PartType` dataframe object using the `.orient_box()` functionality.

5.2.5 Parallel Batch Processing

Investigating the results of a simulation often requires running an identical analysis on many snapshots in order to study how the system changes with time. These operations are typically completely independent, and thus amenable to parallelization—so long as the machine being used has sufficient memory. To aid in the parallelization of such analyses, `gadfly` includes utilities for performing parallel batch processing jobs by making use of python’s `multiprocessing` module.

One issue with doing operations such as this in parallel is that they are often IO-bound. To mitigate the issues that arise when multiple processes attempt to read large amounts of data from disk simultaneously, `gadfly`’s parallelization utilities are designed to load the data needed for a given analysis serially in a separate thread from the main execution. As the necessary data from each snapshot file is loaded, execution is passed to a pool of worker processes which can then perform the remainder of the analysis in parallel. An example of such a parallel batch processing script is included in the examples distributed with `gadfly`.

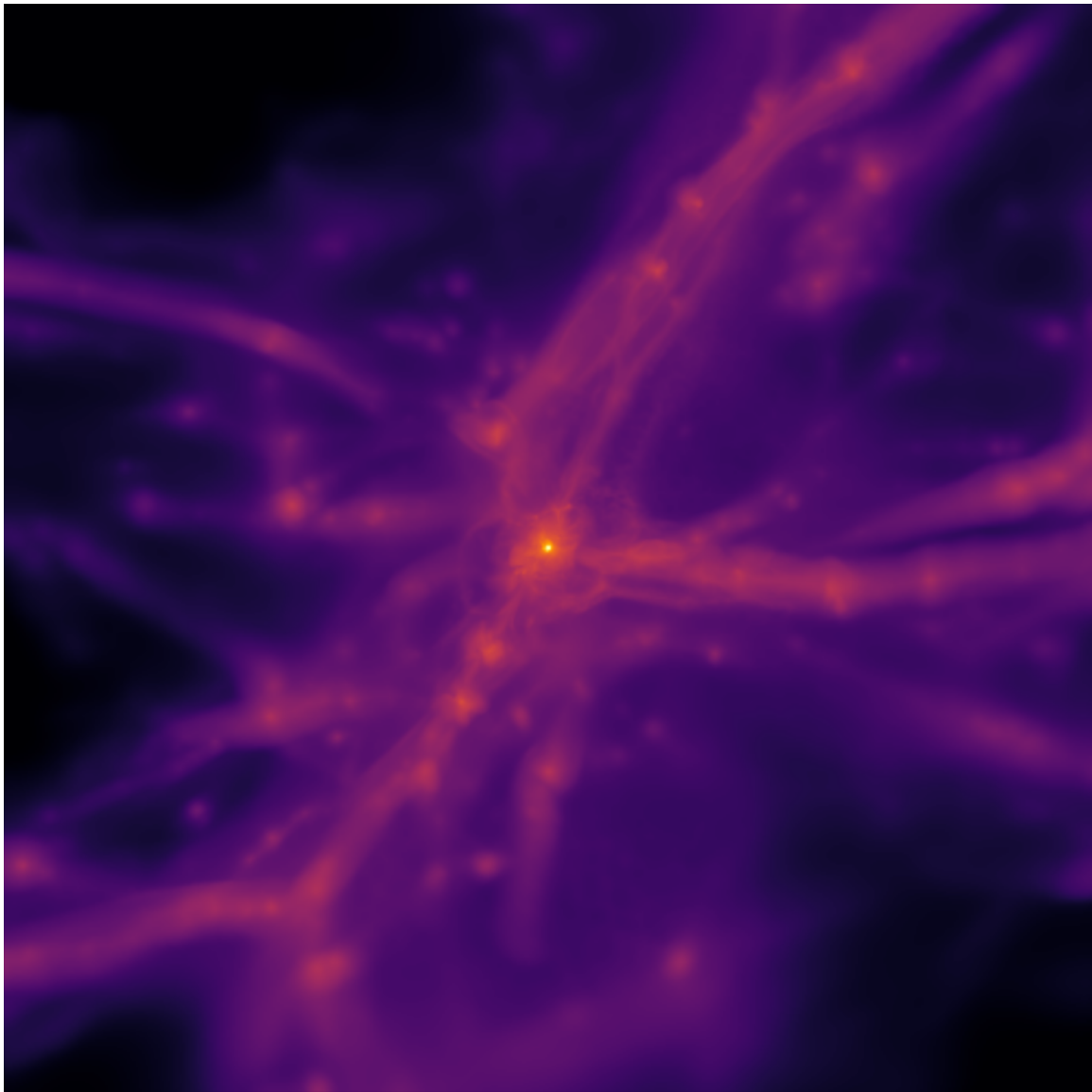


Figure 5.4: Example of a visualization produced by `gadfly`. This particular image shows the density distribution in a minihalo forming at $z = 25$ on 1 kpc scales, and is from a simulation run for Hummel et al. (2015).

5.3 Visualization

Visualization plays a major role in any analysis of simulation data, and the ability to directly visualize the spatial structure and evolution of a system is often crucial to generating insight. While the guiding principle of the `gadfly` project is to avoid reinventing the wheel, instead relying on the tools developed by the broader scientific python community wherever possible, SPH particle rendering is one critical area where that broader ecosystem proves insufficient. To mitigate this shortcoming, `gadfly` includes a minimal library of visualization tools.

The particles in an SPH simulation are best thought of as fluid elements sampling the continuum properties of the gas they represent (Lucy, 1977; Gingold & Monaghan, 1977; Monaghan, 1992; Springel, 2010). They accomplish this by serving as Lagrangian tracers over which the continuum properties are interpolated using a smoothing kernel W . While it is possible to use alternative kernels, most modern SPH implementations (including GADGET) utilize a cubic spline kernel (Springel, 2014):

$$W(r, h_{\text{sml}}) = \begin{cases} 1 - 6 \left(\frac{r}{h_{\text{sml}}} \right)^2 + 6 \left(\frac{r}{h_{\text{sml}}} \right)^3, & 0 \leq \frac{r}{h_{\text{sml}}} \leq \frac{1}{2} \\ 2 \left(1 - \frac{r}{h_{\text{sml}}} \right)^3, & \frac{1}{2} < \frac{r}{h_{\text{sml}}} \leq 1 \\ 0, & \frac{r}{h} > 1, \end{cases} \quad (5.1)$$

where r is the radius and h_{sml} is the characteristic width of the kernel, otherwise known as the smoothing length. The physical density at any point, $\rho(\mathbf{r})$, is then represented by the sum over all particles

$$\rho(\mathbf{r}) \simeq \sum_j m_j W(\mathbf{r} - \mathbf{r}_j, h_{\text{sml}}), \quad (5.2)$$

where m_j is the mass of particle j , located at \mathbf{r}_j . As such, creating visualizations that faithfully reproduce the actual density distribution requires performing this sum over

all particles of interest; this can be quite computationally intensive depending on the number of particles involved and the desired resolution. The SPH particle rendering algorithm included in `gadfly` performs this summation over two dimensions, producing a density-weighted projection. An example of such a visualization produced by `gadfly` is shown in Figure 5.4.

`Gadfly` includes three separate implementations of this algorithm, each of which is best suited to different conditions:

1. The primary implementation is derived from Navratil et al. (2007) and is written in C, parallelized using OpenMP, and wrapped in python using `scipy.weave`. This method must be locally compiled, and will fail if the python interpreter cannot locate a C compiler, or if the requisite libraries are not installed. However, it is the most powerful implementation, best suited to rendering many particles, and to machines with many processors available.
2. A second implementation makes use of `numba` (Lam et al., 2015) to perform just-in-time (JIT) compilation of pure python code using the LLVM compiler infrastructure (Lattner & Adve, 2004). The resulting serial routine is highly optimized, providing performance within a factor of two of the parallel method on a 16-core machine. As such, this method is preferable on smaller machines with fewer processors, and for visualizations including fewer particles where the additional overhead associated with the parallel implementation is significant.
3. The final implementation is a pure python routine included only for situations where the other methods have unmet dependencies. This implementation is over 500 times slower than the others, and as such is suitable only to visualizing

small numbers of particles, or as a last resort.

These methods are all available as independent library functions, and can be used both with particle data in a `PartType` dataframe or independently from the rest of the `gadfly` framework, with data stored in `numpy` arrays. Future versions of `gadfly` will greatly simplify the visualization of data stored in a `PartType` dataframe through the use of a `.visualize()` method (see Section 5.4).

5.4 Future Development

The `gadfly` package is under active development, and in addition to incremental improvements of the existing functionality, a few significant upgrades are planned for future releases. First and foremost, the current `gadfly` units system is fairly inflexible, with limited support for additional units. For the next release we plan on replacing the existing units system, instead employing the far more versatile `astropy.units` framework (Robitaille et al., 2013) as the backend for handling unit conversions. Future releases will also more seamlessly integrate `gadfly`'s visualization tools with the rest of the framework. At the moment the user is required to pass each required field to the visualization methods individually. We intend to integrate this functionality directly into the `PartType` dataframe, allowing the user to simply call `PartType.visualize()` and be presented with a default density projection of the SPH particles currently in the dataframe, similar to the `.plot()` functionality of a standard `pandas.DataFrame`.

In the longer term, the `dask`² project presents an intriguing option for handling

²<http://dask.pydata.org>

very large out-of-core datasets through the use of blocked algorithms and task scheduling. `Dask` manages this by mapping high-level `numpy`, `pandas`, and list operations on large datasets to many operations on smaller chunked datasets that can fit in memory. Future releases of `gadfly` may migrate the data structure on which the `PartType` dataframe is built from the `pandas.DataFrame` to `dask.dataframe` to take advantage of this functionality.

5.5 Summary

In this paper we have presented the first public release of `gadfly`. We have described the framework’s structure, which is designed around three core abstractions: the `PartType` dataframe (Section 5.2.1.1), the `Snapshot` object (Section 5.2.1.2), and the `Simulation` object (Section 5.2.1.3). Additional functionality includes intelligent memory management and file access (Section 5.2.2), basic unit handling (Section 5.2.3), coordinate transformations (Section 5.2.4), utilities for parallel batch processing (Section 5.2.5), and SPH particle visualization (Section 5.3).

`Gadfly` is fully open-source, is released under the MIT License, and can be downloaded and installed from its repository at <http://github.com/hummel/gadfly>. Users can submit bug reports via GitHub, and if they know how to fix them, are welcome to submit pull requests.

Chapter Six: Outlook

Appendix A: Appendix

Included here are the observable properties of the He100 and R175 models from Kasen et al. (2011), including the observable flux and time visible (Figure A.2) and the observable number for each feedback scenario (Figure A.1). These plots are to be compared to Figure 2.5 and Figure 2.6 in Section 2.3. Both cases may be detected with NIRCam beyond $z = 15$ for deep exposures of 10^6 s.

Also included is an extended version of Figure 2.8 showing the detectable number in observing campaigns totalling 10^6 , 10^7 and 10^8 s for all four PISN models (Figure A.3). Only R250-type PISNe will be detectable above reshift 15, and R175- and B200-type PISNe will only be detectable in observing campaigns totalling greater than 10^7 s.

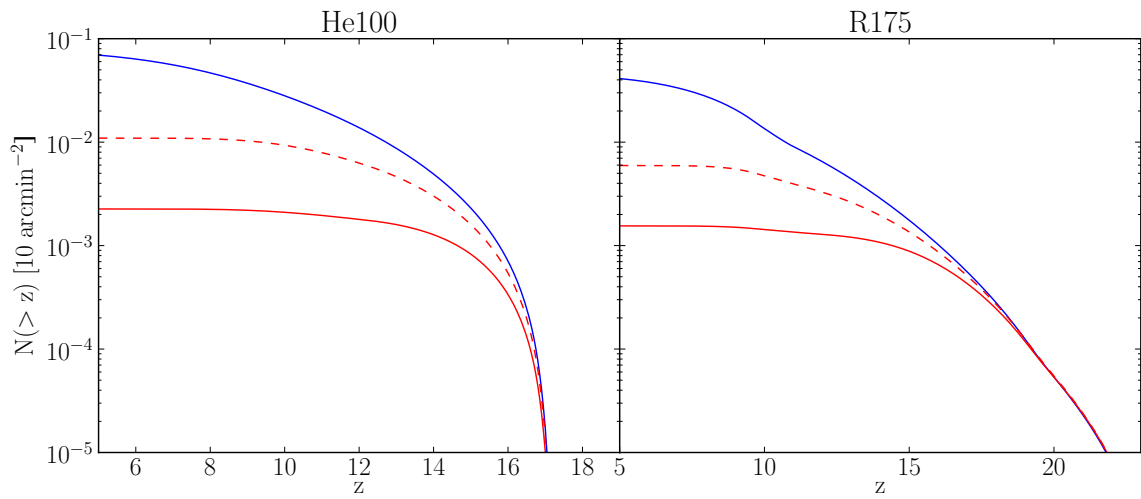


Figure A.1: Upper and lower limits for the number of PISNe per JWST FoV above redshift z with different feedback prescriptions. The observable numbers for a 10^6 s exposure assuming the He100 model are shown on the left; the R175 model is employed on the right. Solid blue lines show an upper limit to the observable number in the case of no feedback, solid red lines an estimate for the observable number in our conservative feedback scenario, and dashed red lines the number in the enhanced star formation case. Note that the x-axis is scaled independently in each panel.

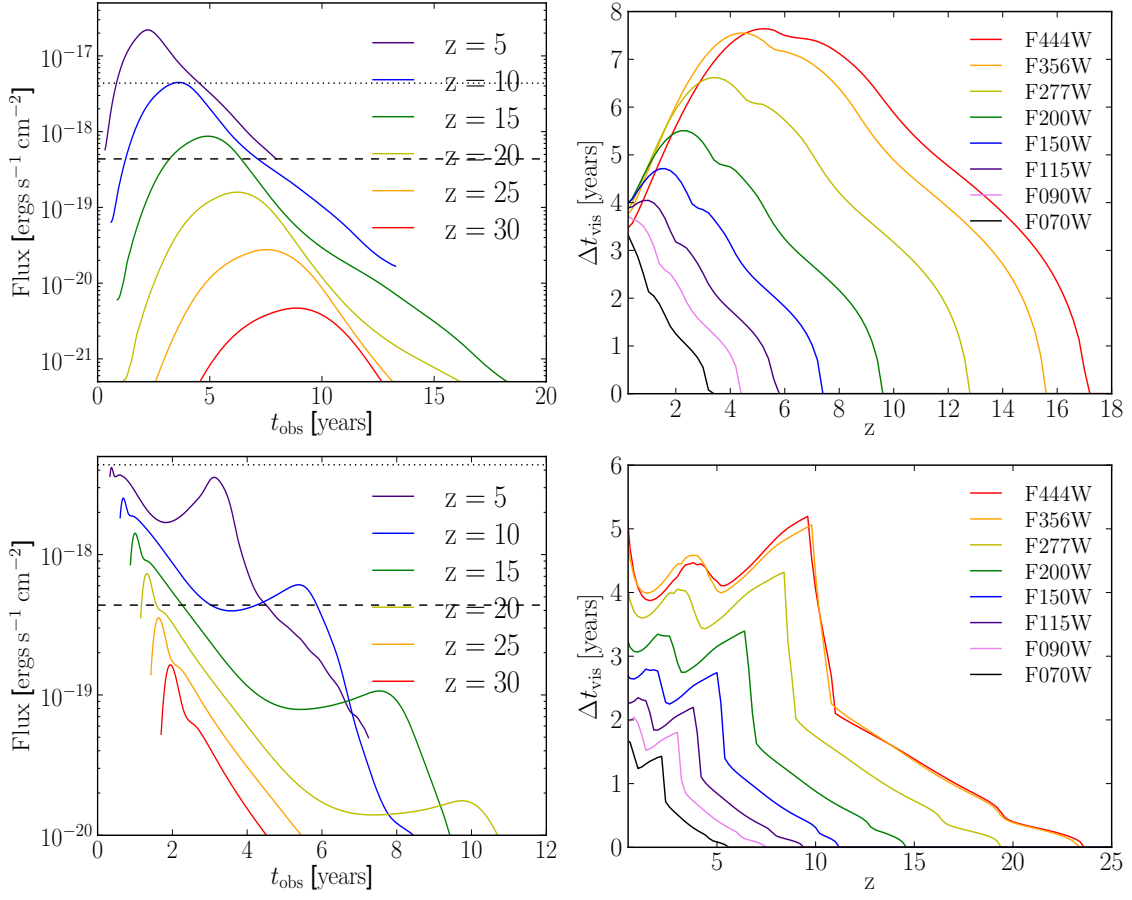


Figure A.2: Left: Lightcurves for the Kasen et al. (2011) He100 (top) and R175 (bottom) models as they would be observed by JWST's F444W NIRCam filter at $z = 5, 10, 15, 20, 25$ and 30 . The flux limits for a 10^6 s (dashed line) and 10^4 s (dotted line) exposure are shown for reference. Right: The visibility time Δt_{vis} in years for He100 (top) and R175 (bottom) as a function of redshift for each of the NIRcam wide filters. Note that the axes are scaled independently.

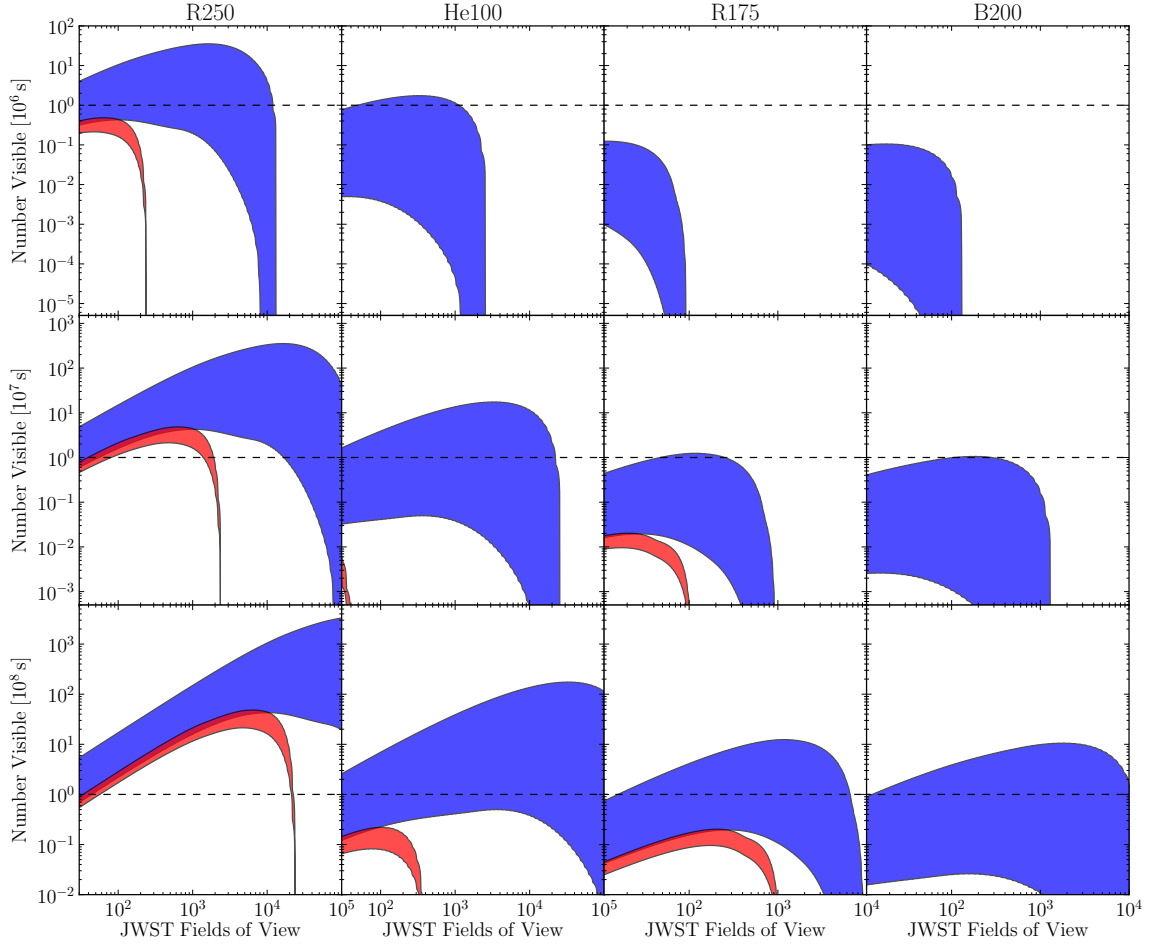


Figure A.3: The total number of PISNe observable with a campaign of 10^6 , 10^7 and 10^8 s (from top to bottom) as a function of total survey area for a given PISN model. In each case, the total campaign time is apportioned equally over the survey area to determine the exposure time for individual pointings. The blue region represents all PISNe, the red only PISNe from $z > 15$. Upper boundaries correspond to the no-feedback upper limit to the PISN rate and lower boundaries to the conservative feedback case. The dashed line marks one PISN visible. Note that not all axes are scaled the same.

Bibliography

- Abel, T., Anninos, P., Zhang, Y., & Norman, M. L. 1997, New Astronomy, 2, 181 71
- Abel, T., Bryan, G. L., & Norman, M. L. 2002, Science, 295, 93 4, 8, 39, 72
- Ade, P. A. R., Aghanim, N., Arnaud, M., et al. 2015, A&A, submitted(arXiv:1502.01589) 2, 74
- Alvarez, M. A., Bromm, V., & Shapiro, P. R. 2006, ApJ, 639, 621 13, 38, 72
- Alvarez, M. A., Wise, J. H., & Abel, T. 2009, ApJ, 701, L133 13
- Ando, S., & Kusenko, A. 2010, ApJ, 722, L39 77
- Asplund, M., Lambert, D. L., Nissen, P. E., Primas, F., & Smith, V. V. 2006, ApJ, 644, 229 73
- Bakker, C. J., & Segrè, E. 1951, Physical Review, 81, 489 85
- Barkana, R., & Loeb, A. 2001, Phys. Rep., 349, 125 3, 8, 15, 17, 38, 51
- Barkat, Z., Rakavy, G., & Sack, N. 1967, Phys. Rev. Lett., 18, 379 9
- Bate, M. R., & Burkert, A. 1997, MNRAS, 288, 1060 48, 81
- Belczynski, K., Bulik, T., & Fryer, C. L. 2012, ApJ, submitted (arXiv:1208.2422) 43
- Bell, A. R. 1978, MNRAS, 182, 147 75
- Biermann, P. L., & Sigl, G. 2001, in Physics and Astrophysics of Ultra-High-Energy Cosmic Rays, Vol. 576 (Berlin: Springer), 1 75

Blandford, R., & Eichler, D. 1987, Phys. Rep., 154, 1 76

Booth, C. M., Agertz, O., Kravtsov, A. V., & Gnedin, N. Y. 2013, ApJ, 777, L16 71

Bradley, L. D., Trenti, M., Oesch, P. A., et al. 2012, ApJ, submitted (arXiv:1204.3641)

37

Bromm, V. 2013, Rep. Prog. Phys., 76, 112901 3, 4, 42, 58, 72, 78, 97

Bromm, V., Coppi, P. S., & Larson, R. B. 1999, ApJ, 527, L5 4, 8, 39, 72

—. 2002, ApJ, 564, 23 4, 8, 39, 54, 59, 71, 72, 88, 89

Bromm, V., Kudritzki, R. P., & Loeb, A. 2001, ApJ, 552, 464 10, 13, 20

Bromm, V., & Larson, R. B. 2004, ARA&A, 42, 79 4, 8, 39, 72

Bromm, V., & Loeb, A. 2003, Nature, 425, 812 20

Bromm, V., Yoshida, N., & Hernquist, L. 2003, ApJ, 596, L135 11, 13, 38, 72

Bromm, V., Yoshida, N., Hernquist, L., & McKee, C. F. 2009, Nature, 459, 49 3, 8, 38

Campisi, M. A., Maio, U., Salvaterra, R., & Ciardi, B. 2011, MNRAS, 416, 2760 41, 78

Caprioli, D., & Spitkovsky, A. 2014, ApJ, 783, 91 76

Cen, R. 2003, ApJ, 591, 12 40, 68

Chatzopoulos, E., & Wheeler, J. C. 2012, ApJ, 748, 42 9, 26

Chen, K.-J., Heger, A., & Almgren, A. S. 2011, Comp. Phys. Communications, 182, 254 32

- Chiappini, C., Frischknecht, U., Meynet, G., et al. 2011, *Nature*, 472, 454 10
- Ciardi, B., Ferrara, A., & Abel, T. 2000, *ApJ*, 533, 594 16
- Clark, P. C., & Glover, S. C. O. 2014, *MNRAS*, 444, 2396 51
- Clark, P. C., Glover, S. C. O., Klessen, R. S., & Bromm, V. 2011a, *ApJ*, 727, 110 4, 39, 61, 70, 72, 100
- Clark, P. C., Glover, S. C. O., Smith, R. J., et al. 2011b, *Science*, 331, 1040 4, 8, 14, 26, 39, 40, 61, 72
- Collette, A. 2008, HDF5 for Python, <http://www.h5py.org/> 108
- Couchman, H. M. P., & Rees, M. J. 1986, *MNRAS*, 221, 53 4, 8, 39
- Cravens, T. E., & Dalgarno, A. 1978, *ApJ*, 219, 750 71
- Dahlén, T., & Fransson, C. 1999, *A&A*, 350, 349 11
- Dalgarno, A., Yan, M., & Liu, W. 1999, *ApJS*, 125, 237 71
- Dermer, C. D., Cavadini, M., Razzaque, S., et al. 2011, *ApJ*, 733, L21 77
- Dicke, R. H., Peebles, P. J. E., Roll, P. G., & Wilkinson, D. T. 1965, *ApJ*, 142, 414 1
- Dijkstra, M., Haiman, Z., Mesinger, A., & Wyithe, J. S. B. 2008, *MNRAS*, 391, 1961 40, 73
- Dopcke, G., Glover, S. C. O., Clark, P. C., & Klessen, R. S. 2013, *ApJ*, 766, 103 39
- Duquennoy, A., & Mayor, M. 1991, *A&A*, 248, 485 42
- Durrer, R., & Neronov, A. 2013, *The A&A Review*, 21, 62 76

- Einstein, A. 1916, Annalen der Physik, 354, 769 1
- Enßlin, T. A., Pfrommer, C., Springel, V., & Jubelgas, M. 2007, A&A, 473, 41 71
- Foreman-Mackey, D., Hogg, D. W., Lang, D., & Goodman, J. 2013, PASP, 125, 306 103
- Fraley, G. S. 1968, Ap&SS, 2, 96 9
- Frost, M. I., Surace, J. A., Moustakas, L. A., & Krick, J. 2009, ApJ, 698, L68 29
- Fryer, C. L., Woosley, S. E., & Heger, A. 2001, ApJ, 550, 372 9
- Fumagalli, M., O'Meara, J. M., & Prochaska, J. X. 2011, Science, 334, 1245 22
- Furlanetto, S. R., & Loeb, A. 2003, ApJ, 588, 18 11
- . 2005, ApJ, 634, 1 22
- Furlanetto, S. R., Peng Oh, S., & Briggs, F. H. 2006, Phys. Rep., 433, 181 70, 101
- Furlanetto, S. R., & Stoever, S. J. 2010, MNRAS, 404, 1869 53
- Gal-Yam, A., Mazzali, P., Ofek, E. O., et al. 2009, Nature, 462, 624 10
- Galli, D., & Palla, F. 1998, A&A, 335, 403 71
- Gammie, C. F. 2001, ApJ, 553, 174 39
- Gardner, J. P., Mather, J. C., Clampin, M., et al. 2006, Space Sci. Rev., 123, 485 11, 29
- Gingold, R. A., & Monaghan, J. J. 1977, MNRAS, 181, 375 114
- Ginzburg, V. L., & Syrovatskii, S. I. 1969, The origin of cosmic rays (New York: Gordon and Breach) 75

- Glassgold, A. E., Galli, D., & Padovani, M. 2012, ApJ, 756, 157 71
- Glassgold, A. E., & Langer, W. D. 1973, ApJ, 186, 859 71
- Glover, S. C. O., & Brand, P. W. J. L. 2001, MNRAS, 321, 385 16
- . 2003, MNRAS, 340, 210 40, 68
- Goldsmith, P. F., & Langer, W. D. 1978, ApJ, 222, 881 71
- Greif, T. H., & Bromm, V. 2006, MNRAS, 373, 128 19, 41, 42, 78
- Greif, T. H., Bromm, V., Clark, P. C., et al. 2012, MNRAS, 424, 399 4, 8, 26, 39, 40, 58, 61, 65, 72, 89
- Greif, T. H., Glover, S. C. O., Bromm, V., & Klessen, R. S. 2010, ApJ, 716, 510 11, 13, 38, 72
- Greif, T. H., Johnson, J. L., Bromm, V., & Klessen, R. S. 2007, ApJ, 670, 1 13, 22, 38, 72
- Greif, T. H., Johnson, J. L., Klessen, R. S., & Bromm, V. 2008, MNRAS, 387, 1021 13
- . 2009, MNRAS, 399, 639 48, 83
- Greif, T. H., Springel, V., White, S. D. M., et al. 2011a, ApJ, 737, 75 4, 8, 14, 26, 39, 49, 61, 72, 83
- Greif, T. H., White, S. D. M., Klessen, R. S., & Springel, V. 2011b, ApJ, 736, 147 60, 92, 100
- Greisen, K. 1966, Phys. Rev. Lett., 16, 748 74

- Grenier, I. A., Black, J. H., & Strong, A. W. 2015, *ARA&A*, 53, 199–71
- Haiman, Z., Abel, T., & Rees, M. J. 2000, *ApJ*, 534, 11–16, 40, 68
- Haiman, Z., Rees, M. J., & Loeb, A. 1997, *ApJ*, 476, 458–16
- Haiman, Z., Thoul, A. A., & Loeb, A. 1996, *ApJ*, 464, 523–4, 8, 39
- Hanasz, M., Lesch, H., Naab, T., et al. 2013, *ApJ*, 777, L38–71
- Hartwig, T., Clark, P. C., Glover, S. C. O., Klessen, R. S., & Sasaki, M. 2015, *ApJ*, 799, 114–69
- Heger, A., Fryer, C. L., Woosley, S. E., Langer, N., & Hartmann, D. H. 2003, *ApJ*, 591, 288–4, 9, 13, 14, 38, 72
- Heger, A., & Woosley, S. E. 2002, *ApJ*, 567, 532–9, 11
- . 2010, *ApJ*, 724, 341–4, 38, 72
- Hirano, S., Hosokawa, T., Yoshida, N., Omukai, K., & Yorke, H. W. 2015, *MNRAS*, 448, 568–39
- Hirano, S., Hosokawa, T., Yoshida, N., et al. 2014, *ApJ*, 781, 60–4, 39, 72, 89
- Hopkins, P. F. 2015, *MNRAS*, 450, 53–7, 102
- Hosokawa, T., Hirano, S., Kuiper, R., et al. 2015, eprint arXiv:1510.01407–4, 72, 89
- Hosokawa, T., Omukai, K., Yoshida, N., & Yorke, H. W. 2011, *Science*, 334, 1250–8, 51, 85
- Hubble, E. 1929, *Proceedings of the National Academy of Sciences*, 15, 168–1
- Hubble, E. P. 1925, *ApJ*, 62, 409–1

- Hummel, J. A., Stacy, A., Jeon, M., Oliveri, A., & Bromm, V. 2015, MNRAS, 453, 4136 xiii, xv, 73, 78, 79, 81, 84, 86, 88, 92, 99, 100, 113
- Hunter, J. D. 2007, Computing in Science & Engineering, 9, 90–103
- Inayoshi, K., & Omukai, K. 2011, MNRAS, 416, 2748–43, 85
- Indriolo, N., Fields, B. D., & McCall, B. J. 2009, ApJ, 694, 257–71
- Jasche, J., Ciardi, B., & Enßlin, T. A. 2007, MNRAS, 380, 417–74, 85
- Jeon, M., Pawlik, A. H., Bromm, V., & Milosavljević, M. 2014, MNRAS, 440, 3778–40, 43, 51
- Jeon, M., Pawlik, A. H., Greif, T. H., et al. 2012, ApJ, 754, 34–40, 43, 51, 68
- Joggerst, C. C., & Whalen, D. J. 2011, ApJ, 728, 129–9, 32
- Johnson, J. L., Greif, T. H., & Bromm, V. 2007, ApJ, 665, 85–13, 38, 72
- Jones, E., Oliphant, T., Peterson, P., & Al., E. 2001, SciPy: Open source scientific tools for Python, <http://www.scipy.org> 103
- Jubelgas, M., Springel, V., Enßlin, T., & Pfrommer, C. 2008, A&A, 481, 33–71
- Karlsson, T., Bromm, V., & Bland-Hawthorn, J. 2013, Rev. Mod. Phys., 85, 809–3, 9, 38, 72
- Karlsson, T., Johnson, J. L., & Bromm, V. 2008, ApJ, 679, 6–9
- Kasen, D., Woosley, S. E., & Heger, A. 2011, ApJ, 734, 102 ix, xv, 9, 12, 25, 26, 28, 30, 32, 33, 119, 121
- Kitayama, T., Susa, H., Umemura, M., & Ikeuchi, S. 2001, MNRAS, 326, 1353–16

- Kitayama, T., & Yoshida, N. 2005, ApJ, 630, 675 11
- Kitayama, T., Yoshida, N., Susa, H., & Umemura, M. 2004, ApJ, 613, 631 13, 38, 72
- Komatsu, E., Dunkley, J., Nolta, M. R., et al. 2009, ApJS, 180, 330 13
- Kudritzki, R. P. 2002, ApJ, 577, 389 9
- Kuhlen, M., & Madau, P. 2005, MNRAS, 363, 1069 40, 68
- Lam, S. K., Pitrou, A., & Seibert, S. 2015, in Proceedings of the Second Workshop on the LLVM Compiler Infrastructure in HPC - LLVM '15 (New York, New York, USA: ACM Press) 115
- Lattner, C., & Adve, V. 2004, in LLVM: A Compilation Framework for Lifelong Program Analysis and Transformation, San Jose, CA, USA, 75–88 115
- Loeb, A. 2010, How Did the First Stars and Galaxies Form? (Princeton, NJ: Princeton University Press) 3, 8, 38
- Longair, M. S. 1994, High energy astrophysics. Vol.2: Stars, the galaxy and the interstellar medium (Cambridge: Cambridge University Press) 75
- Lucy, L. B. 1977, AJ, 82, 1013 114
- Machacek, M. E., Bryan, G. L., & Abel, T. 2001, ApJ, 548, 509 16, 17
- Mackey, J., Bromm, V., & Hernquist, L. 2003, ApJ, 586, 1 viii, 11, 24, 25
- Madau, P., Della Valle, M., & Panagia, N. 1998, MNRAS, 297, L17 11
- Madau, P., Ferrara, A., & Rees, M. J. 2001, ApJ, 555, 92 38, 72
- Maeder, A., & Meynet, G. 2012, Rev. Mod. Phys., 84, 25 4, 38, 72

- Maio, U., Ciardi, B., Dolag, K., Tornatore, L., & Khochfar, S. 2010, MNRAS, 407, 1003 22
- Maio, U., Khochfar, S., Johnson, J. L., & Ciardi, B. 2011, MNRAS, 414, 1145 38, 72
- Mannheim, K., & Schlickeiser, R. 1994, A&A 286 71
- Martel, H., Evans II, N. J., & Shapiro, P. R. 2006, ApJS, 163, 122 54, 88
- McKee, C. F., & Tan, J. C. 2008, ApJ, 681, 771 72
- McKinney, W. 2010, in Proceedings of the 9th Python in Science Conference, ed. S. van der Walt & J. Millman, 51–56 103
- Meiksin, A. 2009, Rev. Mod. Phys., 81, 1405 3, 9
- Mesinger, A., Bryan, G. L., & Haiman, Z. 2006a, ApJ, 648, 835 17
- Mesinger, A., Johnson, B. D., & Haiman, Z. 2006b, ApJ, 637, 80 12
- Miralda-Escudé, J. 2003, Science, 300, 1904 3, 8, 38
- Miralda-Escudé, J., & Rees, M. J. 1997, ApJ, 478, 57 viii, 11, 24, 25
- Mirocha, J. 2014, MNRAS, 443, 1211 40, 70
- Mitra, S., Kulkarni, G., Bagla, J. S., & Yadav, J. K. 2011, Bull. Astr. Soc. of India, 39, 563 15
- Mitsuda, K., Inoue, H., Koyama, K., et al. 1984, Astronomical Society of Japan, 36, 741 43
- Monaghan, J. J. 1992, ARA&A, 30, 543 114
- Mori, M., Ferrara, A., & Madau, P. 2002, ApJ, 571, 40 11, 38, 72

- Navratil, P., Johnson, J., & Bromm, V. 2007, IEEE Transactions on Visualization and Computer Graphics, 13, 1712 115
- Neronov, A., & Vovk, I. 2010, Science, 328, 73 77
- Oh, S. P. 2001, ApJ, 553, 499 40
- Omukai, K., & Nishi, R. 1999, ApJ, 518, 64 16
- Omukai, K., & Yoshii, Y. 2003, ApJ, 599, 746 17
- O'Shea, B. W., & Norman, M. L. 2007, ApJ, 654, 66 4, 8, 39, 72
- Osterbrock, D. E., & Ferland, G. J. 2006, Astrophysics of gaseous nebulae and active galactic nuclei (Sausalito, CA: University Science Books) 51
- Padovani, M., Galli, D., & Glassgold, A. E. 2009, A&A, 501, 619 71
- Padovani, M., Hennebelle, P., & Galli, D. 2013, A&A, 560, A114 71
- Padovani, M., Hennebelle, P., Marcowith, A., & Ferrière, K. 2015, A&A, 582, L13 71
- Palla, F., Salpeter, E. E., & Stahler, S. W. 1983, ApJ, 271, 632 48, 83
- Pan, T., Kasen, D., & Loeb, A. 2012, MNRAS, 422, 2701 12
- Pawlak, A. H., Milosavljevic, M., & Bromm, V. 2011, ApJ, 731, 54 5, 10, 17
- Penzias, A. A., & Wilson, R. W. 1965, ApJ, 142, 419 1
- Perlmutter, S., Aldering, G., Goldhaber, G., et al. 1999, ApJ, 517, 565 2
- Pfrommer, C., Springel, V., Ensslin, T. A., & Jubelgas, M. 2006, MNRAS, 367, 113

- Pontzen, A., Roškar, R., Stinson, G., & Woods, R. 2013, Astrophysics Source Code Library, ascl:1305.002 103
- Press, W. H., & Schechter, P. 1974, ApJ, 187, 425 15, 77
- Rees, M. J., & Ostriker, J. P. 1977, MNRAS, 179, 541 92
- Ricotti, M., Gnedin, N. Y., & Shull, J. M. 2001, ApJ, 560, 580 17
- . 2002a, ApJ, 575, 33 17
- . 2002b, ApJ, 575, 49 17
- Riess, A. G., Filippenko, A. V., Challis, P., et al. 1998, AJ, 116, 1009 2
- Ripamonti, E., Iocco, F., Bressan, A., et al. 2008, in Proceedings of Science 40
- Ripamonti, E., Iocco, F., Ferrara, A., et al. 2010, MNRAS, 406, 2605 40
- Ripamonti, E., Mapelli, M., & Ferrara, A. 2007, MNRAS, 375, 1399 74
- Robertson, B. E., Ellis, R. S., Dunlop, J. S., McLure, R. J., & Stark, D. P. 2010, Nature, 468, 49 38, 72
- Robitaille, T. P., Tollerud, E. J., Greenfield, P., et al. 2013, A&A, 558, A33 103, 116
- Rollinde, E., Vangioni, E., & Olive, K. A. 2005, ApJ, 627, 666 73
- . 2006, ApJ, 651, 658 xii, 73, 79, 80
- Rubin, V. C., Thonnard, N., & Ford, W. K., J. 1980, ApJ, 238, 471 1
- Safranek-Shrader, C., Agarwal, M., Federrath, C., et al. 2012, MNRAS, 426, 1159 69
- Salem, M., & Bryan, G. L. 2014, MNRAS, 437, 3312 71

- Salem, M., Bryan, G. L., & Hummels, C. 2014, ApJ, 797, L18 71
- Sasaki, S. 1994, PASJ, 46, 427 15
- Sazonov, S., & Sunyaev, R. 2015, MNRAS, 454, 3464 71, 76, 101
- Scannapieco, E., Madau, P., Woosley, S. E., Heger, A., & Ferrara, A. 2005, ApJ, 633, 1031 11, 22
- Schaerer, D. 2002, A&A, 382, 28 4, 13, 38, 72
- . 2003, A&A, 397, 527 19
- Schlickeiser, R. 2002, *Cosmic Ray Astrophysics* (Berlin: Springer) 75, 84, 85
- Schneider, R., Ferrara, A., Natarajan, P., & Omukai, K. 2002, ApJ, 571, 30 20
- Sedov, L. I. 1959, *Similarity and Dimensional Methods in Mechanics* (New York: Academic Press) 22
- Shchekinov, Y. A., & Vasiliev, E. O. 2004, A&A, 419, 19 74
- Shu, F. H. 1977, ApJ, 214, 488 66
- Shull, J. M., & van Steenberg, M. E. 1985, ApJ, 298, 268 47, 53, 85
- Smith, N., Li, W., Foley, R. J., et al. 2007, ApJ, 666, 1116 10
- Smith, R. J., Glover, S. C. O., Clark, P. C., Greif, T. H., & Klessen, R. S. 2011, MNRAS, 414, 3633 39
- Smith, R. J., Iocco, F., Glover, S. C. O., et al. 2012, ApJ, 761, 154 40
- Sokasian, A., Yoshida, N., Abel, T., Hernquist, L., & Springel, V. 2004, MNRAS, 350, 47 38, 72

Spitzer, L. 1978, Physical Processes in the Interstellar Medium (New York: Wiley-Interscience) 71

Spitzer, L., & Scott, E. H. 1969, ApJ, 158, 161 71, 85

Spitzer, L., & Tomasko, M. G. 1968, ApJ, 152, 971 71, 83

Springel, V. 2005, MNRAS, 364, 1105 6, 17, 47, 79, 102

—. 2010, ARA&A, 48, 391 114

Springel, V. 2014, in Lecture notes given at the 43rd Saas Fee Advanced School, March 11-16, 2013, Villars-sur-Ollon, Switzerland 114

Springel, V., White, S. D. M., Tormen, G., & Kauffmann, G. 2001a, MNRAS, 328, 726 17

Springel, V., Yoshida, N., & White, S. D. 2001b, New Astronomy, 6, 79 102

Stacy, A., & Bromm, V. 2007, MNRAS, 382, 229 xii, xiv, 74, 76, 80, 84, 85, 97, 98, 100

—. 2013, MNRAS, 433, 1094 4, 39, 42, 59, 72, 81, 89

Stacy, A., Bromm, V., & Loeb, A. 2011a, ApJ, 730, L1 60, 92, 100

—. 2011b, MNRAS, 413, 543 10, 26

Stacy, A., Greif, T. H., & Bromm, V. 2010, MNRAS, 403, 45 4, 8, 13, 26, 39, 48, 54, 58, 61, 72, 81, 88

—. 2012a, MNRAS, 422, 290 8, 26, 39

Stacy, A., Pawlik, A. H., Bromm, V., & Loeb, A. 2012b, MNRAS, 421, 894 40

- . 2014, MNRAS, 441, 822 40
- Stanev, T. 2004, High energy cosmic rays (Berlin: Springer) 75
- Strong, A. W., Moskalenko, I. V., & Ptuskin, V. S. 2007, Annual Review of Nuclear and Particle Science, 57, 285 71
- Susa, H., Hasegawa, K., & Tominaga, N. 2014, ApJ, 792, 32 39
- Tegmark, M., Silk, J., Rees, M. J., et al. 1997, ApJ, 474, 1 4, 8, 39
- Tielens, A. G. G. M. 2005, The Physics and Chemistry of the Interstellar Medium (Cambridge: Cambridge University Press), doi:10.1017/CBO9780511819056 71
- Tominaga, N., Umeda, H., & Nomoto, K. 2007, ApJ, 660, 516 10
- Toomre, A. 1964, ApJ, 139, 1217 64
- Tornatore, L., Ferrara, A., & Schneider, R. 2007, MNRAS, 382, 945 22, 38, 72
- Trenti, M., Stiavelli, M., & Michael Shull, J. 2009, ApJ, 700, 1672 12
- Trenti, M., Bradley, L. D., Stiavelli, M., et al. 2011, ApJ, 727, L39 37
- Tumlinson, J., Venkatesan, A., & Shull, J. M. 2004, ApJ, 612, 602 9
- Turk, M. J., Clark, P. C., Glover, S. C. O., et al. 2011, ApJ, 726, 55 48, 83, 103
- Umeda, H., & Nomoto, K. 2003, Nature, 422, 871 10, 38, 72
- Valdés, M., & Ferrara, A. 2008, MNRAS, 387, L8 53
- van der Walt, S., Colbert, S. C., & Varoquaux, G. 2011, Computing in Science & Engineering, 13, 22 103

- Vasiliev, E. O., & Shchekinov, Y. A. 2006, Astronomy Reports, 50, 778 74
- Venkatesan, A., Giroux, M. L., & Shull, J. M. 2001, ApJ, 563, 1 40, 68
- Wang, H.-H., Klessen, R. S., Dullemond, C. P., Van Den Bosch, F. C., & Fuchs, B. 2010, MNRAS, 407, 705 65
- Weinmann, S. M., & Lilly, S. J. 2005, ApJ, 624, 526 viii, 11, 23, 24, 34
- Weiss, J., & Bernstein, W. 1956, Physical Review, 103, 1253 85
- Whalen, D. J., Abel, T., & Norman, M. L. 2004, ApJ, 610, 14 13, 38, 72
- Whalen, D. J., van Veelen, B., O'Shea, B. W., & Norman, M. L. 2008, ApJ, 682, 49 11, 13
- Wise, J. H., & Abel, T. 2005, ApJ, 629, 615 viii, 11, 24, 25
- . 2007, ApJ, 665, 899 13
- . 2008, ApJ, 685, 40 11, 13, 22, 38, 72
- Wolcott-Green, J., Haiman, Z., & Bryan, G. L. 2011, MNRAS, 418, 838 19
- Woosley, S. E., Blinnikov, S., & Heger, A. 2007, Nature, 450, 390 10
- Yoon, S.-C., Dierks, A., & Langer, N. 2012, A&A, 542, A113 9, 26
- Yoshida, N., Abel, T., Hernquist, L., & Sugiyama, N. 2003, ApJ, 592, 645 16, 17, 39, 72
- Yoshida, N., Bromm, V., & Hernquist, L. 2004, ApJ, 605, 579 13
- Yoshida, N., Oh, S. P., Kitayama, T., & Hernquist, L. 2007, ApJ, 663, 687 13

Yoshida, N., Omukai, K., Hernquist, L., & Abel, T. 2006, ApJ, 652, 6 4, 8, 39, 49,
72, 83

Zatsepin, G. T., & Kuz'min, V. A. 1966, Journal of Experimental and Theoretical
Physics Letters, 4 74